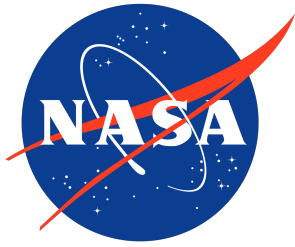NASA/TM–20230010662

Computational Analysis of the X-57 Maxwell Airplane, the Landing Configuration with High-Lift Blowing and Aileron Deflections (Preliminary Fuselage)

Karen A. Deere and Jeffrey K. Viken
NASA Langley Research Center, Hampton, Virginia

Michael R. Wiese and Norma L. Farr
Craig Technologies, Hampton, Virginia

January 2024

NASA STI Program Report Series

Since its founding, NASA has been dedicated to the advancement of aeronautics and space science. The NASA scientific and technical information (STI) program plays a key part in helping NASA maintain this important role.

The NASA STI Program operates under the auspices of the Agency Chief Information Officer. It collects, organizes, provides for archiving, and disseminates NASA's STI. The NASA STI Program provides access to the NTRS Registered and its public interface, the NASA Technical Report Server, thus providing one of the largest collections of aeronautical and space science STI in the world. Results are published in both non-NASA channels and by NASA in the NASA STI Report Series, which includes the following report types:

- TECHNICAL PUBLICATION. Reports of completed research or a major significant phase of research that present the results of NASA programs and include extensive data or theoretical analysis. Includes compilations of significant scientific and technical data and information deemed to be of continuing reference value. NASA counterpart of peer-reviewed formal professional papers, but having less stringent limitations on manuscript length and extent of graphic presentations.

- TECHNICAL MEMORANDUM. Scientific and technical findings that are preliminary or of specialized interest, e.g., quick release reports, working papers, and bibliographies that contain minimal annotation. Does not contain extensive analysis.

- CONTRACTOR REPORT. Scientific and technical findings by NASA-sponsored contractors and grantees.
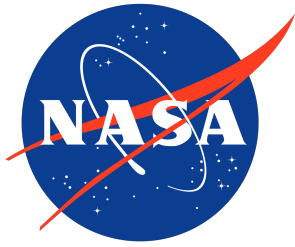
- CONFERENCE PUBLICATION. Collected papers from scientific and technical conferences, symposia, seminars, or other meetings sponsored or co-sponsored by NASA.

- SPECIAL PUBLICATION. Scientific, technical, or historical information from NASA programs, projects, and missions, often concerned with subjects having substantial public interest.

- TECHNICAL TRANSLATION. English-language translations of foreign scientific and technical material pertinent to NASA's mission.

Specialized services also include organizing and publishing research results, distributing specialized research announcements and feeds, providing information desk and personal search support, and enabling data exchange services.

For more information about the NASA STI Program, see the following:

- Access the NASA STI program home page at http://www.sti.nasa.gov

- Help desk contact information: https://www.sti.nasa.gov/sti-contact-form/ and select the "General" help request type.

Computational Analysis of the X-57 Maxwell Airplane, the Landing Configuration with High-Lift Blowing and Aileron Deflections (Preliminary Fuselage)

Karen A. Deere and Jeffrey K. Viken
NASA Langley Research Center, Hampton, Virginia

Michael R. Wiese and Norma L. Farr
Craig Technologies, Hampton, Virginia

January 2024

Acknowledgments

Available from:

NASA STI Program / Mail Stop 050
NASA Langley Research Center
Hampton, VA 23681-2199

Abstract

The X-57 Maxwell is an all-electric airplane with a distributed electric propulsion system used for a high-lift system at takeoff and landing conditions. The Kestrel and USM3D flow solvers were used at the NASA Langley Research Center to investigate the performance of the X-57 Maxwell in the development of an aerodynamic database. The configuration investigated in this paper had a $30°$ flap deflection, and in addition the pilot's right aileron was deflected and undeflected in different cases. The solutions were computed at an airspeed of 58 KEAS, for an altitude of 6000 feet, and a flight unit Reynolds number of 0.588e+06 per foot. To evaluate the high-lift distributed electric propulsion system without aileron deflections, the solutions were computed for an angle-of-attack sweep from $-2°$ to $20°$, with the high-lift propellers blowing and the cruise propellers excluded from the simulation. To investigate the aileron effectiveness, the solutions were computed at angles of attack of $-2°$ and $14°$, for aileron deflections from $-25°$ to $18°$ with the high-lift propellers blowing and the cruise propellers windmilling at idle-power. The high-lift propellers and the idle-power cruise propellers were modeled with an actuator disk. Results show negligible differences in lift, drag, and pitching moment whether the idle-powered cruise propellers were included or excluded from the simulation. In general, the Kestrel and USM3D codes compared well for lift, drag, and pitching moment for the landing configuration with no aileron control. The Kestrel code, using the Spalart-Allmaras turbulence model with rotation correction terms, predicted an increasing lift coefficient up to maximum lift coefficient of 4.65 at a $15°$ angle of attack. The USM3D code, using the Spalart-Allmaras turbulence model turbulence model with the Quadratic Constitutive Relation predicted an increasing lift coefficient up to maximum lift coefficient of 4.5 at a $12°$ angle of attack, with the lift remaining constant through a $14°$ angle of attack. A possible difference in lift coefficient between the codes for high angles of attack may result from the different available options used with the standard Spalart-Allmaras turbulence model. The Kestrel code predicted more drag across the angle-of-attack range than the USM3D code. The codes compared well for pitching moment coefficient across the angle-of-attack range. The Kestrel and USM3D codes compared well for aileron effectiveness at a $2°$ angle of attack. The Kestrel code predicts better aileron effectiveness than USM3D at a $14°$ angle of attack. There is more flow separation in the region outboard of the last high-lift nacelle for the USM3D solutions at a $14°$ angle of attack, which diminishes the ability of the aileron to be effective.

Contents

3

List of Figures

4

6

List of Tables

Nomenclature

α	=	angle of attack, degrees
a_∞	=	freestream speed of sound, feet/second
b_{ref}	=	reference span, inches
β	=	angle of sideslip, degrees
$cfl1$	=	numerical field in USM3D input file representing the minimum CFL number
$cfl2$	=	numerical field in USM3D input file representing the maximum CFL number
c_{ref}	=	reference chord, mean aerodynamic chord, 25.56 inches
C_D	=	drag coefficient = drag force / $(q_\infty\ S_{ref})$
C_L	=	lift coefficient = lift force / $(q_\infty\ S_{ref})$
$C_{L,max}$	=	maximum lift coefficient = maximum lift force / $(q_\infty\ S_{ref})$
C_l	=	rolling moment coefficient = rolling moment / $(q_\infty\ S_{ref}\ c_{ref})$
C_m	=	pitching moment coefficient = pitching moment / $(q_\infty\ S_{ref}\ c_{ref})$
C_n	=	yawing moment coefficient = yawing moment / $(q_\infty\ S_{ref}\ b_{ref})$
C_p	=	pressure coefficient = $(p - P_\infty)$ / (q_∞)
C_T	=	thrust coefficient = T / $(\rho_\infty*(\text{RPM}/60)^{2}*D^{4})$
$C_{T,usm}$	=	normalized thrust coefficient for USM3D = $4/\pi^{3}*C_T$
C_Q	=	torque coefficient = Q / $(\rho_\infty*(\text{RPM}/60)^{2}*D^{5})$
$C_{Q,usm}$	=	normalized torque coefficient for USM3D = $8/\pi^{3}*C_Q$
C_Y	=	side force coefficient = side force / $(q_\infty\ S_{ref})$
δ_1	=	height of the first node off the surface, inches
δ_a	=	aileron deflection, positive trailing edge down, degrees
δ_f	=	flap deflection, positive trailing edge down, degrees
$delta_t$	=	time step used for nondimensionalization in USM3D, Equation 3, inches/step
D	=	propeller diameter, inches
$D_{t,char}$	=	distance a signal travels in one time step, Equation 2, inches/step
e	=	efficiency factor
γ	=	gamma, specific heat ratio
J	=	propeller advance ratio = V_∞ / $((\text{RPM}/60)*D)$
J_{usm}	=	normalized propeller advance ratio for USM3D = J/π
$log(r/r0)$	=	log scale L2-norm of the mean flow residue, normalized by the initial value
$log(tnu/tnu0)$	=	log scale L2-norm of the turbulent residue, normalized by the initial value
L/D	=	lift to drag ratio
L_{char}	=	characteristic reference length, inches
M	=	freestream Mach number
N	=	number of time steps
ϕ	=	roll angle, degrees
P	=	pressure, generic expression, psf
P_{out}	=	power, kW
P_∞	=	freestream static pressure, psf
q_∞	=	freestream dynamic pressure = $\rho_\infty\ V^{2}$ / 2, psf
Q	=	torque, lbf-ft
ρ_∞	=	freestream density, slugs/feet^{3}
r	=	radial distance, inches
R	=	propeller radius, inches

R_{prop}	=	maximum radius of the propeller, inches
Re	=	unit Reynolds number, per foot
Re_c	=	Reynolds number based on reference chord
$ReUe$	=	freestream Reynolds number per unit length, specified in millions
$R1$	=	grid growth rate 1
$R2$	=	grid growth rate 2
S_{ref}	=	(wing) reference area, 66.67 feet^2
s	=	primary length scale at the source center
S	=	stretched length scale at the source center
T	=	thrust, lbf
T_∞	=	freestream temperature, °F
T_{max}	=	location of maximum thrust along the propeller radius
u	=	dimensional velocity, feet/second
U	=	nondimensional velocity used in USM3D $= u \, / \, a_\infty$
V_∞	=	freestream velocity, inches/sec
W	=	weight, lbs
W/S_ref	=	wing loading, W $/ \, S_{ref}$
x, y, z	=	Cartesian coordinates, inches
xmc	=	moment center in X-direction (streamwise direction), inches
ymc	=	moment center in Y-direction (spanwise direction), inches
y^+_{cell}	=	nondimensional height of the first cell in the boundary layer
y^+_{node}	=	nondimensional height of the first node in the boundary layer
zmc	=	moment center in Z-direction (normal direction), inches

Acronyms and Abbreviations

AFRC	Armstrong Flight Research Center
AR	aspect ratio $= b_{ref} \, / \, S_{ref}$
ARC	Ames Research Center
CAD	computer aided design
CFD	computational fluid dynamics
CFL	Courant–Friedrichs–Lewy [number]
DEP	distributed electric propulsion
GA	General Aviation
GEOLAB	GEOmetry LABoratory
KCAS	Knots Calibrated Airspeed
KEAS	Knots Equivalent Airspeed
KTAS	Knots True Airspeed
LE	leading edge
LES	Large Eddy Simulation
LGC	landing gear cover
NASA	National Aeronautics and Space Administration
LaRC	Langley Research Center
LAVA	Launch Ascent and Vehicle Aerodynamics
NPS	nacelles, pylons, strakes
POR	percent over range convergence equation
RANS	Reynolds-averaged Navier-Stokes (equations)

RC	rotation correction (terms)
RPM	revolutions per minute
SA	Spalart-Allmaras [turbulence model]
TN	wingtip nacelle
QCR	Quadratic Constitutive Relation
TetrUSS	NASA Tetrahedral Unstructured Software System
VG	vortex generator

1   Introduction

The X-57 Maxwell is an all-electric airplane that has a distributed electric propulsion (DEP) system to increase lift at takeoff and landing conditions [1–3]. The X-57 airplane was designed to cruise efficiently at 150 knots true airspeed (KTAS), which is a Mach number (M) of $M = 0.233$ at an altitude of 8,000 feet. A concept image of the X-57 Maxwell aircraft is shown in Figure 1. The DEP system includes twelve high-lift, electrically-powered propellers positioned along the wing leading edge to increase the velocity over the wing, and thus, reduce the upper-surface pressure, for a boost of lift. The high-lift propellers fold conformally onto the high-lift nacelles at cruise conditions to minimize drag when the DEP high-lift system is not needed. The electrically-powered cruise propellers are located on the wingtip nacelles. Some previous computational fluid dynamics (CFD) results on earlier variations of the airplane have been published [4–10].

The initial objective of the X-57 Maxwell project was to demonstrate that emission-free electric motors could be integrated with the aircraft configuration to increase overall aircraft efficiency. The goal was to demonstrate that the small cruise efficient wing, integrated with the DEP system, could achieve the flight objectives with at least 3x lower energy use compared to the baseline Tecnam P2006T aircraft [1]. The lower energy use comes from a combination of improved aerodynamic efficiency from reducing the wing area, an improvement in motor efficiency, and an improvement in propulsion efficiency from the wingtip propellers operating opposite to the wingtip vortex to reduce induced drag. To meet the cruise performance goal of $M = 0.233$ and at an altitude of 8000 feet, the X-57 has a cruise lift coefficient ($C_{L,cruise}$) of 0.7516 and would need to have a cruise drag coefficient of 0.05423 or less.

In the X-57 Maxwell project, the development and analysis of the airplane was divided into four phase modifications (Mod), with each Mod focusing on a different aircraft configuration. The Mod I aircraft configuration is the original Tecnam P2006T aircraft and is shown in Figure 2. The P2006T aircraft has a wing loading of 17 psf, a wing span of 37.4 feet, a root chord of 4.57 feet (54.84 inches), and a tip chord of 2.9 feet (34.8 inches). The Mod II aircraft configuration is an electric version of the P2006T, with electric motors and X-57 cruise propellers replacing the original combustion engines and propellers on the P2006T aircraft. A front view of the Mod II configuration with the electric motors running is shown in Figure 3. The Mod II aircraft configuration was planned to test engine safety and service during

taxi tests, and then flight tested before the electric motors, the batteries, and the instrumentation were to be installed in the Mod III configuration. For the Mod III aircraft configuration, the P2006T wing is replaced with the X-57 wing, and the Mod II electric cruise motors and propellers will be moved out to the wingtip nacelles, see Figure 4. Finally, the Mod IV aircraft configuration has the 12 high-lift motors and propellers integrated into the X-57 wing for the final, all-electric X-57 Maxwell aircraft, see Figure 5. Again, the high-lift propellers will only be operational at takeoff and landing conditions to produce the extra lift needed at low airspeeds. The X-57 Maxwell airplane has a higher wing loading of 45 psf, a shorter wing span of 31.6 feet (379.47 inches), and a shorter mean aerodynamic chord of 2.13 feet (25.56 inches), than the original Tecnam P2006T airplane.

The X-57 Maxwell airplane has only 42% of the wing area of the original Tecnam P2006T wing, but with an increased gross weight. The gross weight needed to be increased because the increased weight of the batteries, compared to the weight of the fuel for the original Tecnam engines, was much greater than the weight savings of the electric motors. The primary driver of reducing the wing area was to reduce drag, and increase the efficiency of the X-57. The smaller wing area reduces the total wetted area and the skin friction drag. The wing aspect ratio was increased from 8.8 to 15.0 for the X-57 to minimize the induced drag penalty of the increased gross weight. The minimum wing area was determined based upon the limits of the powered high-lift augmentation, wing structural stiffness, and wing internal volume. The X-57 wing loading is 2.5 times the original Tecnam P2006T airplane. The X-57 will experience smaller g-loadings in gusts with such a large increase in wing loading compared to the original Tecnam P2006T airplane. For airplanes with the propeller plane behind the center of gravity (CG), the tip mounted propellers can be directionally stabilizing [11]. However, the X-57 tip-mounted propellers are ahead of the CG, and therefore may reduce the directional stability in gusts. Thus, the directional stability of the X-57 airplane would need to be evaluated in flight tests.

The purpose of this paper was to document aerodynamic data of the Mod IV configuration with a landing flap deflection (δ_f) of $\delta_f = 30°$, with and without the pilot's right aileron deflected. Results were computed with the CFD flow solvers, USM3D and Kestrel. The high-lift propellers and the idle-power cruise propellers were modeled with an actuator disk. The aerodynamic data of interest are lift coefficient (C_L), drag coefficient(C_D), rolling moment coefficient (C_l), pitching moment coefficient (C_m), and yawing moment coefficient (C_n). The flow conditions were an airspeed of 58 knots equivalent airspeed (KEAS), an altitude of 6000 feet, and a flight unit Reynolds number (Re) of $Re = 0.588E+06$/ft. To evaluate the DEP high-lift system, the solutions were computed for an angle-of-attack sweep from $\alpha = -2°$ to $\alpha = 20°$ with no aileron deflection, and the high-lift propellers blowing. The cruise propellers at idle-power were excluded from this simulation. Results will show there was negligible difference between modeling idle-powered cruise propellers or excluding them from the simulation. To investigate the aileron roll effectiveness, the solutions were computed at two angles of attack, $\alpha = -2°$ and at $\alpha = 14°$, for aileron deflections (δ_a) from $\delta_a = -25°$ (trailing edge up) to $\delta_a = 18°$ (trailing edge down) with the high-lift propellers blowing and the idle-powered, cruise propellers

windmilling.

This is the second paper in a series of NASA technical memorandum papers from the NASA Langley Research Center (LaRC) documenting the computational results for the X-57 Maxwell airplane. The first paper documented the unblown and unpowered performance [12]. This paper documents the Mod IV configuration with a landing flap deflection (δ_f) of $\delta_f = 30°$ with high-lift blowing (HLB), and with aileron deflections. The third paper will record results for the X-57 at cruise power without high-lift blowing. The fourth paper will present the effects of high-lift power and flap deflection for the Mod IV configuration. The first set of four papers documents the results for the X-57 with the preliminary fuselage that was available the first three years of the project. The second set of papers will include the X-57 flight fuselage and fairing; showing the effects of the flight fuselage as compared to the preliminary fuselage, the motor-out effects with and without aileron deflections, and the effects of the updated takeoff flap setting of $\delta_f = 20°$, on the aerodynamic coefficients.

Since there are no reliable experimental performance data for the X-57 airplane, the CFD results from three NASA centers were used to develop an aerodynamic database and establish uncertainty bounds for the force and moment coefficients for the X-57 Maxwell. The X-57 CFD team at LaRC used the USM3D code [13, 14] developed at Langley, and the Kestrel code [15, 16] developed by the Department of Defense (DoD) Computational Research and Engineering Acquisition Tools and Environment (CREATE-AV) group. The X-57 CFD team at the NASA Armstrong Flight Research Center (AFRC) used the commercially developed STAR-CCM+ code [17]. The X-57 CFD team at the NASA Ames Research Center (ARC) used the ARC developed Launch Ascent and Vehicle Aerodynamics (LAVA) code [18]. The fuselage geometry at the wing root for the configuration discussed in this paper is slightly different than the fuselage used with LAVA and STAR-CCM+. The configurations herein used the OpenVSP analytic fuselage geometry (preliminary fuselage), while a wind-tunnel model fuselage geometry was scaled up to full size for the LAVA and STAR-CCM+ solutions. The configurations with the preliminary fuselage and with the wind-tunnel model fuselage compare well except at the junction of the fuselage and wing-root where the smaller X-57 wing replaced the larger P2006T wing and intersection geometries were developed differently. Additionally, the results from LAVA and STAR-CCM+ were computed with a local time stepping or steady-state Reynolds-averaged Navier-Stokes (RANS) approach, while the current solutions were computed with global time stepping or time-accurate RANS approach. A time-accurate RANS approach was believed to be more appropriate for high-lift configurations near stall and for configurations with flow separation, as was expected for the X-57 Maxwell airplane. However, a hybrid model of RANS combined with a Large Eddy Simulation (LES) approach may be required to more accurately predict the maximum lift coefficient ($C_{L,max}$) and stall.

Figure 1. Concept Image of the X-57 Maxwell Airplane [Source: NASA / Advanced Concepts Lab].

Figure 2. Mod I, the Tecnam P2006T Airplane [Source: NASA].

Figure 3. Mod II, the Tecnam P2006T Airplane with Electric Cruise Motors [Source: NASA AFRC TV / Steve Parcel].

Figure 4. Concept Image of Mod III, the X-57 Maxwell Airplane with Cruise Propellers Operating and High-Lift Propellers Stowed [Source: NASA / Advanced Concepts Lab].

Figure 5. Concept Image of Mod IV, the X-57 Maxwell Airplane with Cruise Propellers and High-Lift Propellers Operating [Source: NASA / Advanced Concepts Lab].

2 Methods Description

This section describes the details for generating the CFD data in this report. The majority of the data shown in this study were computed at NASA LaRC using Kestrel and USM3D. Additionally, the X-57 CFD team results [19–21] were included with permission from STAR-CCM+ and from LAVA in Sections 3.5 and 3.6. The codes used the finite-volume, Reynolds-averaged Navier-Stokes (RANS) method with the Spalart-Allmaras (SA) turbulence model [22]. Additionally, variants to the SA turbulence model were implemented as available for each code.

2.1 Computational Flow Solvers

The USM3D code version 6.0 was run with a global time stepping or time-accurate RANS approach on a fully unstructured, tetrahedral mesh. The SA turbulence model with the Quadratic Constitutive Relation (SA QCR) was used, but the rotation correction option was not available. The QCR2000 version was used, but the term QCR will be used throughout the rest of the paper. The implicit Gauss-Seidel scheme and the Roe flux difference-splitting scheme were used.

The Kestrel code version 8.02 was run with the time-accurate RANS approach on a fully unstructured, mixed-element mesh. The QCR option was not available in Kestrel V8.0, and therefore, the SA turbulence model with the rotation correction (SA RC) was used. The matrix scheme was Gauss-Seidel and the inviscid flux scheme was HLLE++.

The Tecplot software was used for post processing results from both Kestrel and USM3D. Additionally, the NASA LaRC-developed code USMC6 [23] was used for analyzing the USM3D solutions.

The STAR-CCM+ code [17] was run with the local time stepping or steady-state RANS approach on a polyhedral mesh combined with a prism boundary layer mesh. The SA RC option was available at the time of this work and the details of the STAR-CCM+ approach are shown in references [19, 20].

The LAVA code [18] was also run with the steady-state RANS approach, but on a body-fitted curvilinear mesh and off-body Cartesian farfield mesh. The QCR option was available at the time of this work and the details of the LAVA approach are discussed in references [19, 20].

2.2 Freestream Conditions

The freestream flow conditions were specified with the Mach number, Reynolds number and temperature. The input for USM3D is Reynolds number per unit length specified in millions ($ReUe$). One primary flight condition was researched in this work, namely an airspeed of 58 KEAS ($M = 0.098$), which yields a freestream velocity of $V_\infty = 107.2$ feet/sec. The flight altitude was 6000 feet at a temperature of 37.6°F, which gives a density of 0.001988 slug/ft^3. Data were computed for angles of attack from $\alpha = -2°$ to $\alpha = 20°$. The flight Reynolds number of 1.25 million was based on mean aerodynamic chord of 2.13 feet (25.56 inches), and the input for USM3D was $ReUe = 0.04905$.

The current paper focuses on high-lift blowing results at the above conditions. However, in Section 3.1 and Section 3.2, comparisons of the high-lift blowing results are made to the unblown results at slightly different freestream conditions. The unblown wing results were previously computed. For these comparisons, the flow speed is incompressible for all cases, and the Reynolds number variation is between 1.25 and 2.81 million. The unblown landing flap at 30° was computed at an airspeed of 88 KEAS ($M = 0.138$), a flight altitude of 2500 feet, a temperature of 50.1°F, a density of 0.002208 slug/ft^3 and a flight Reynolds number of 1.97 million based on mean aerodynamic chord. The unblown cruise wing was computed at an airspeed of 133 KEAS ($M = 0.233$), a flight altitude of 8000 feet, a temperature of 30.5°F, a density of 0.001868 slug/ft^3 and a flight Reynolds number of 2.81 million based on mean aerodynamic chord.

2.3   Power Conditions

Both the Kestrel and USM3D codes can model propellers with an actuator disk model, which simplifies the gridding process by eliminating the need to mesh every blade. This was beneficial for the X-57 configuration, which has 60 propeller blades for the DEP high-lift system and 6 propeller blades for the cruise motors.

The Kestrel actuator disk model requires five inputs for each propeller; angular velocity specified in rotations per minute (RPM), radial location of the maximum thrust, rotor method (disk or annulus), propeller thrust, and thrust vector. The actuator disk can be implemented as a uniform jump or with triangular thrust and torque distributions. The uniform jump is specified by setting the radial location of maximum thrust to 0. The triangular thrust and torque distributions start at 0 at the center and increase linearly to the maximum values at the specified radius, and then decrease linearly to the tip. Since the grids were made with positive x in the flow direction, the thrust vector for the high-lift propellers was specified as (-1, 0, 0). If the right-hand rule rotation vector of the propeller is in the direction of the thrust vector, then RPM is specified as a positive number. If the right-hand rule rotation vector of the propeller is in the opposite direction of the thrust vector, then RPM is specified as a negative number.

The USM3D actuator disk model requires nine inputs for each propeller; the propeller outer radius, the location of the propeller center (x, y, z coordinates), the normalized advance ratio (J_{usm}), the normalized thrust coefficient ($C_{T,usm}$), the normalized torque coefficient ($C_{Q,usm}$), the rotational direction, and the loading type. The loading type can be implemented with a uniform jump or with user-defined thrust and torque distributions that are a function of radius, $T(R)$ and $Q(R)$. The Goldstein thrust and torque distributions can be implemented with the user-defined distributions. The normalized advance ratio is $J_{usm} = J/\pi$, the normalized thrust coefficient is $C_{T,usm} = (4/\pi^3)*C_T$, and the normalized torque coefficient is $C_{Q,usm} = (8/\pi^3)*C_Q$.

Figure 6 shows Kestrel data for the effect of the propeller thrust distribution on lift coefficient for the Mod II configuration. Four solutions are compared in Figure 6; a uniform loading thrust distribution and three triangular thrust distributions with the maximum thrust located at 25%, 75%, and 100% of the propeller radius. The

effect of the radial location of maximum thrust on lift coefficient was a difference of 0.03 in lift coefficient. The maximum thrust location at $r/R_{prop} = 0.25$ resulted in the highest lift coefficient, albeit only by 0.03. The lowest lift coefficient for these approaches occurred at the maximum thrust locations at $r/R_{prop} = 0.75$ and $r/R_{prop} = 1$, while the lift coefficient for the uniform loading condition was about 0.01 higher. Although the thrust distribution had a small effect on lift coefficient for the Mod II configuration, it should be noted that the airplane has one motor and propeller on each wing. There may be a larger impact on lift coefficient for the X-57 airplane, since it has six propellers on each wing and cruise propellers located at the wingtips. Therefore, it is important to model the propeller thrust distributions as close to reality as possible. Also important, although for drag prediction, is modeling the correct rotation direction of the propellers. The propellers on the Mod II configuration rotate in the direction of the wingtip vortex, while the X-57 cruise propellers rotate in the opposite direction to reduce induced drag.
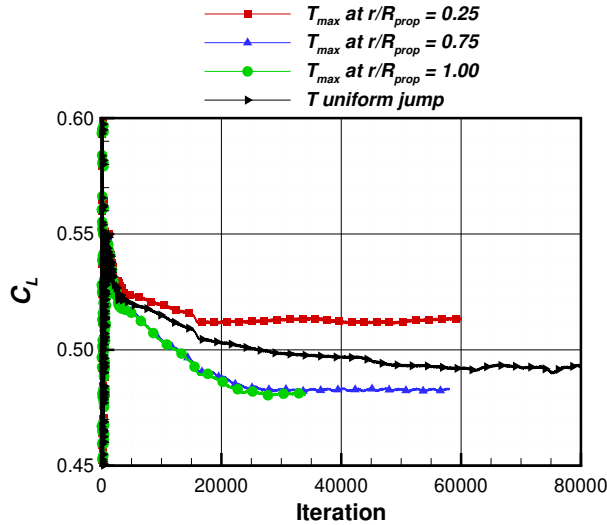
Figure 6. Effect of Cruise Propeller Thrust Distribution for the Mod II Configuration at $M = 0.1964$, $\alpha = 3.5°$, $Re_c = 4.76\text{E}{+}06$, $T = 84$ lbf, and $Q = 89.5$ lbf-ft. Solutions computed with Kestrel, SA turbulence model.

2.3.1 DEP High-Lift Blowing Propeller Conditions

The thrust and torque distributions that are expected from the high-lift propellers of the DEP system were generated with the XROTOR code [24]. The exact XROTOR distributions were not used for this paper, but were used as targets for inputs to the CFD codes. Figure 7 shows the thrust distribution for the DEP high-lift propellers; at 5035 RPM, a thrust of $T = 50.65$ lbf, a torque of $Q = 16.23$ lbf-ft and power of $P_{out} = 11.6$ kW. The diameter of the high-lift propellers is $D = 22.68$ inches.

The DEP high-lift propeller inputs used for the Kestrel code were an angular velocity of 5035 RPM, a maximum thrust (T_{max}) location at $r/R_{prop} = 0.9$, an

annulus rotor method, a propeller thrust of $T = 50.65$ lbf, and a thrust vector of (-1, 0, 0). The triangular thrust and torque distribution was used for modeling the high-lift propellers because it was the best approach available with Kestrel to model the XROTOR distribution shown in Figure 7.

The DEP high-lift propeller inputs used for the USM3D code were a normalized advance ratio $J_{usm} = 0.2149$, a normalized thrust coefficient $C_{T,usm} = 0.03660$, a normalized torque coefficient $C_{Q,usm} = 0.01241$, and a uniform loading type of 0. Although the ideal loading type for modeling the DEP high-lift propellers with the XROTOR thrust and torque distributions was the user-defined loading type available in USM3D, the authors did not have time to validate this approach until after this data delivery date.
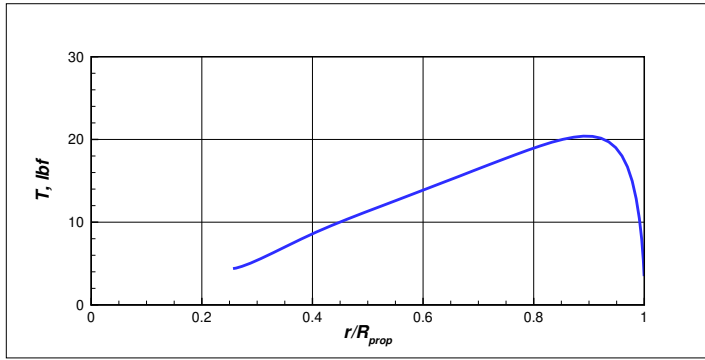
Figure 7. XROTOR Thrust Distribution for the DEP High-Lift Propellers, 5035 RPM, $T = 50.65$ lbf, $Q = 16.23$ lbf-ft, and $P_{out} = 11.6$ kW.

2.3.2 Mod III Cruise Power Propeller Conditions

The cruise propellers were intended to be in an idling, windmilling state. The XROTOR thrust distribution for the cruise propellers in idle conditions is shown in Figure 8. The thrust distribution was computed with XROTOR for 1540 RPM, a blade pitch of 14° (flat pitch), a thrust of $T = -8.02$ lbf, a torque of $Q = 0.65$ lbf-ft and power of $P_{out} = 0.14$ kW. The diameter of the cruise propellers is $D = 60$ inches. The cruise power propeller inputs for the Kestrel code were an angular velocity of 1540 RPM, a triangular thrust distribution with the maximum thrust location at r/R_{prop}=0.92, an annulus rotor method, and a thrust of $T = -8.02$ lbf. This is specified in the input file as $T = 8.02$ lbf with a thrust vector of (1, 0, 0). The inputs for the USM3D code were a radius of $R = 30$ inches, a normalized advance ratio of $J_{usm} = 0.26564$, a normalized thrust coefficient of $C_{T,usm} = -0.00126$, a normalized torque coefficient of $C_{Q,usm} = 0.00004$, and a uniform jump loading type.

2.4 Initial and Boundary Conditions

A no-slip boundary condition was used on all airplane solid surfaces. For these subsonic flow conditions, a characteristic inflow and outflow boundary condition
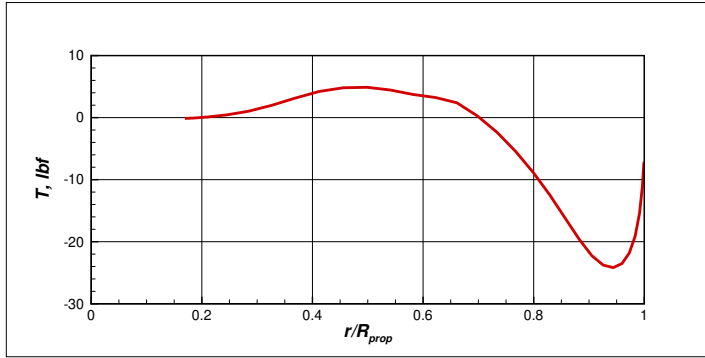
Figure 8. XROTOR Thrust Distribution for the Cruise Propellers, 1540 RPM, T = -8.02 lbf, Q = 0.65 lbf-ft, and P_{out} = 0.14 kW.

was used at the inflow face, the lateral faces, and at the downstream outflow face of the computational domain. The inflow boundary condition was implemented by setting the Mach number, Reynolds number and temperature. The characteristic boundary condition used fixed and extrapolated Riemann invariants of the incoming and outgoing waves along characteristic directions defined normal to the boundary. Local velocity components and speed of sound were computed from the invariants, density was computed from the entropy relationship and pressure was computed from the ideal gas law using the square of the speed of sound. An annulus actuator disk boundary condition was used for modeling the DEP high-lift propellers.

2.5   Input File and Solution Procedure

The Kestrel User Interface (KUI) was used to set up the Kestrel input file, and many of the code default settings were accepted. The user inputs angle of attack, angle of sideslip, Reynolds number based on chord, temperature and Mach number for each case. The user can also specify geometric values of reference area, span, chord and moment reference location for automatic calculation of aerodynamic coefficients.

A typical USM3D input file is shown in Figure 9. For the USM3D code, the user must specify the Mach number, angle of attack (alpha), the sideslip angle (beta), and the freestream Reynolds number per unit length specified in millions ($ReUe$). For each geometric configuration, the user must specify reference area (sref), reference length (cref), reference span (bref), moment center in x-direction (xmc), moment center in y-direction (ymc), and moment center in z-direction (zmc). The USM3D solutions were started with 5,000 iterations using local time stepping, steady-state RANS approach (itimeacc = 0), then the solutions were switched to a global time stepping, time-accurate RANS approach (itimeacc = -2). At the start of a new solution (irest = 0), the USM3D code used a spatial accuracy flag of iorder = 0 or automatic ordering. This selection started the code with first-order spatial accuracy until the residual dropped one order of magnitude, and then the code automatically switched to second-order spatial accuracy. For the time-accurate RANS method, the spatial accuracy was set to second order (iorder = 2). A typical solution was

started with 5,000 iterations (ncyc = 5,000), and Courant–Friedrichs–Lewy (CFL) number was adjusted from –1.0 (dt/cfl1) to 50 (cfl2) over 2000 iterations (iramp). On a restart, the solution was continued with irest = 1, and the CFL number remained constant (dt/cfl1 = cfl2 = 50) if continuing with local time stepping or set to (dt/cfl1 = -1 and cfl2 = 1) for global time stepping. On a restart and change to global time stepping, the ncyc parameter was used for the number of subiterations at each time step (ntstep). The turbulence model was specified with the ivisc parameter. The fully turbulent calculations in this paper were computed using the SA turbulence model (ivisc = 2) with the Quadratic Constitutive Relation (QCR) option (iqcrflg=1).

Mach	alpha	beta	ReUe,mil	Tinf,dR	itwall	Tw/Tinf		ipwall
0.098	2.0	0	0.049045	497.27	0	-1.0		0
sref	cref	bref	xmc	ymc	zmc			
9600.00	25.560833	379.47332	154.797	0.0	64.527			
ioverset	impl	dt/cfl1	iramp	cfl2	cflmin	GS_tol		crelax
0	1	-1.0	2000	50.0	1.0	-20.0		0.7
itimeacc	deltat	ntstep	res_step	imvgrd	isolavg	nbgnavg		
0	10.20	450	-3.00	0	1	500		
irest	mstage	iresmth	dqmax	p_break	p_min	limiter		lim_coeff
0	3	1	0.5	0.05	0.001	0		0.01
nupdate	nwrest	nwflo	nwflobgn	ipltqn	idiagnos	nodeypl		lim_frz
1	2000	0	0	2	1	0		0
iorder	lapl-avg	high-bc	ifds	ivisc	itrp		EV_lim	iqcrflg
0	1	0	1	2	0		0	1
ncyc	nengines	nsinkbc	nrotor	compF&M	p_bc1002	cldes		
5000	0	0	0	-1	0.714290	0.0		
lkeord	icons	nstagek	t_dtfact	t_intsity	mut/mul	ratiokp	dkemax	
1	1	10	1.0	1.0e-3	0.009	0.00	0.25	
inl	ilhg	iwallf	icompCorr	itempCorr	itk	isk	idt_proc	
0	-14	0	0	0	2	0	0	
f1kemax	itranflg							
1.0	0							

(a) Steady-State RANS

Mach	alpha	beta	ReUe,mil	Tinf,dR	itwall	Tw/Tinf		ipwall
0.098	2.0	0	0.049045	497.27	0	-1.0		0
sref	cref	bref	xmc	ymc	zmc			
9600.00	25.560833	379.47332	154.797	0.0	64.527			
ioverset	impl	dt/cfl1	iramp	cfl2	cflmin	GS_tol		crelax
0	1	-1.0	0	1.0	1.0	-20.0		0.7
itimeacc	deltat	ntstep	res_step	imvgrd	isolavg	nbgnavg		
-2	10.20	600	-3.00	0	1	500		
irest	mstage	iresmth	dqmax	p_break	p_min	limiter		lim_coeff
1	3	1	0.5	0.05	0.001	0		0.01
nupdate	nwrest	nwflo	nwflobgn	ipltqn	idiagnos	nodeypl		lim_frz
1	250	0	0	2	1	0		0
iorder	lapl-avg	high-bc	ifds	ivisc	itrp		EV_lim	iqcrflg
2	1	0	1	2	0		0	1
ncyc	nengines	nsinkbc	nrotor	compF&M	p_bc1002	cldes		
15	0	0	0	-1	0.714290	0.0		
lkeord	icons	nstagek	t_dtfact	t_intsity	mut/mul	ratiokp	dkemax	
1	1	10	1.0	1.0e-3	0.009	0.00	0.25	
inl	ilhg	iwallf	icompCorr	itempCorr	itk	isk	idt_proc	
0	-14	0	0	0	2	0	0	
f1kemax	itranflg							
1.0	0							

(b) Time-Accurate RANS

Figure 9. Typical Input File for USM3D with SA Turbulence Model with QCR Selected. Freestream Conditions for 58 KEAS and 6000 feet.

24

2.6   Computer Platform

Resources supporting this work were provided by the NASA High-End Computing (HEC) Program through the NASA Advanced Supercomputing (NAS) Division at the Ames Research Center. The Pleiades supercomputer at NAS was used for all these cases. A semispan mesh was used for investigating the DEP high-lift system through angle-of-attack sweeps. A fullspan mesh was used for investigating the aileron roll effectiveness at select angles of attack.

The Kestrel solutions used 32 nodes from Ivy, each having 20 cores per node, for a total of 640 processors per solution on the semispan mesh. For the fullspan mesh, Kestrel solutions used 52 nodes from Haswell, each having 24 cores per node, for a total of 1248 processors per solution. The USM3D solutions used 24 Ivy nodes for a total of 480 processors per solution on the semispan mesh, and 40 Ivy nodes for a total of 800 processors per solution for the fullspan mesh.

2.7 Coordinate System

The reference coordinate system used for the USM3D and Kestrel codes is shown in Figure 10, with the reference axes positioned at the main coordinate system origin for the project $((x, y, z) = (0, 0, 0))$. The positive y-axis is aligned with the pilot's right wing. The positive x-axis is in the direction of the freestream flow and the y-axis and z-axis are specified normal to the x-axis. The angle of attack (α) is defined in the x-z plane and the sideslip angle (β) is defined in the x-y plane. The moment reference center $((x, y, z) = (154.797, 0, 64.527))$ is shown in Figure 11.

(a) Top View, x-y plane   (b) Side View, x-z plane
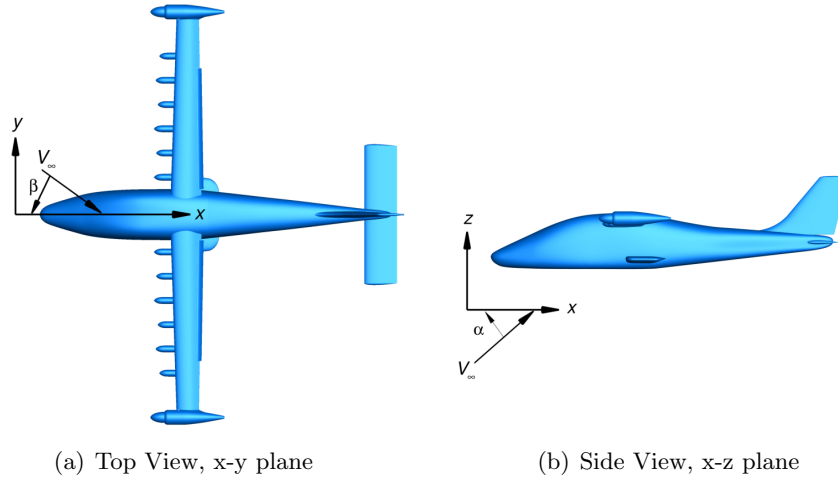
Figure 10. The Geometry (CAD) Reference Coordinate System.

(a) Top View, x-y plane   (b) Side View, x-z plane
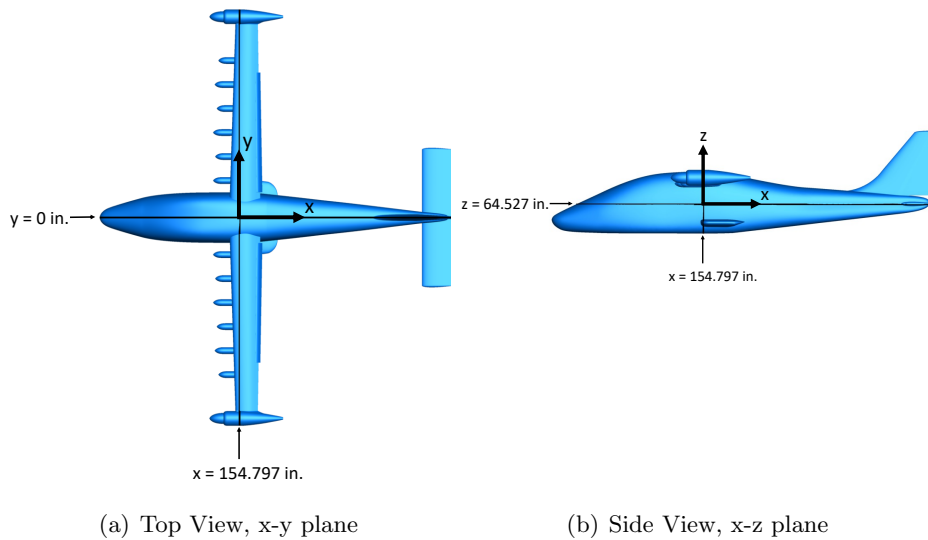
Figure 11. The Moment Reference Center Location.

2.8 Geometry Definition

The Vehicle Sketch Pad (OpenVSP) software [25, 26] was used to generate the geometry of the unpowered X-57 Maxwell Mod III configuration, which had no high-lift blowing propellers nor cruise propellers. The X-57 Maxwell has a root chord (25.56 inches) that is nearly half the original Tecnam P2006T root chord (54.84 inches). Figure 12(a) shows a top down view of the airplane wireframe with the Tecnam wing shaded blue and the X-57 wing shaded green (with a pink and blue arrow highlighting the boundary). Figure 12(b) shows an isometric view of the wing root region, with the larger Tecnam wing shaded blue and the smaller X-57 wing shaded green. Therefore, the intersection of the X-57 wing into the fuselage is completely different than the original Tecnam P2006T. The fit routine in the OpenVSP software was used to modify the original computer aided design (CAD) of the isolated fuselage, to define the new fuselage outer mold line using analytical curves in both the x-y and y-z planes. This fuselage will be referred to as the 'preliminary fuselage'. The preliminary fuselage was used for CFD computations at NASA Langley for the first three years before the actual X-57 flight fuselage geometry was available. During the structural design for the X-57 Maxwell, it was discovered that the preliminary fuselage would not contain the hardware that was designed to attach the X-57 Mod III wing to the original Tecnam P2006T fuselage structure. A final 'X-57 fuselage' was designed to completely contain the structure required to support the wing. In follow-on papers, the final X-57 flight fuselage geometry will be modeled in NASA Langley computational results. However, this paper reports results for the X-57 Mod III geometry with the preliminary fuselage.

The NASA LaRC GEOmetry LABoratory (GEOLAB) supported this effort by preparing the CAD geometry from OpenVSP for grid generation. The OpenVSP geometry was imported into the commercial CAD package, Siemens NX. All the components were intersected; the flap bracket fairings were cleaned and trimmed for the flap setting to create a solid bracket volume. The final geometry was sewn together to create a single, water-tight configuration.

The shaded surface geometry for the X-57 Maxwell Mod IV configuration used in this study is shown in Figure 13. The geometry with the preliminary fuselage included high-lift propellers and cruise propellers, the flap deflected at $\delta_f = 30°$, a neutral stabilator, a vortex generator (VG) on the wingtip nacelle, a t-strip on the rudder, a gurney flap on the horizontal stabilizer, and a wingtip fillet at the intersection of the wing and tip nacelle. To investigate the high-lift capability at an airspeed of 58 KEAS, the ailerons were neutral for an angle-of-attack sweep. To investigate roll effectiveness with the high-lift propellers operating, the right aileron was deflected at these angles: $-25°$, $-15°$, $-10°$, $-5°$, $10°$, and $18°$. The left aileron remained neutral for all simulations. Figure 14 shows the right aileron deflections in black, with a trailing edge downward for positive deflections and a trailing edge upward for negative deflections.
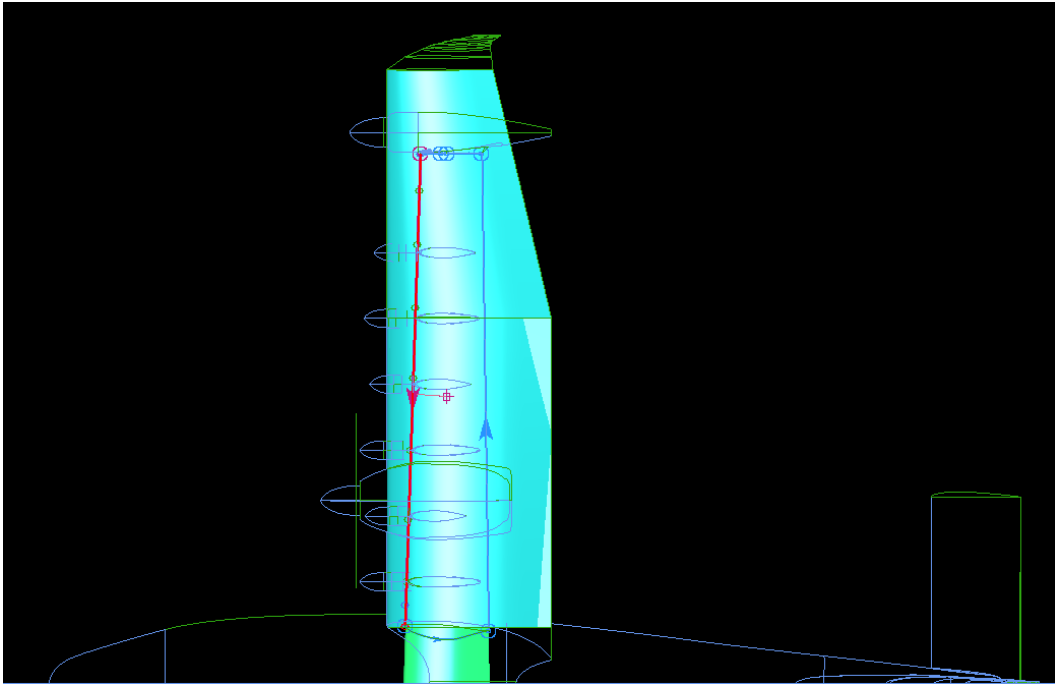
(a) Top Down View of the Smaller X-57 Wing Inside of the Tecnam Wing
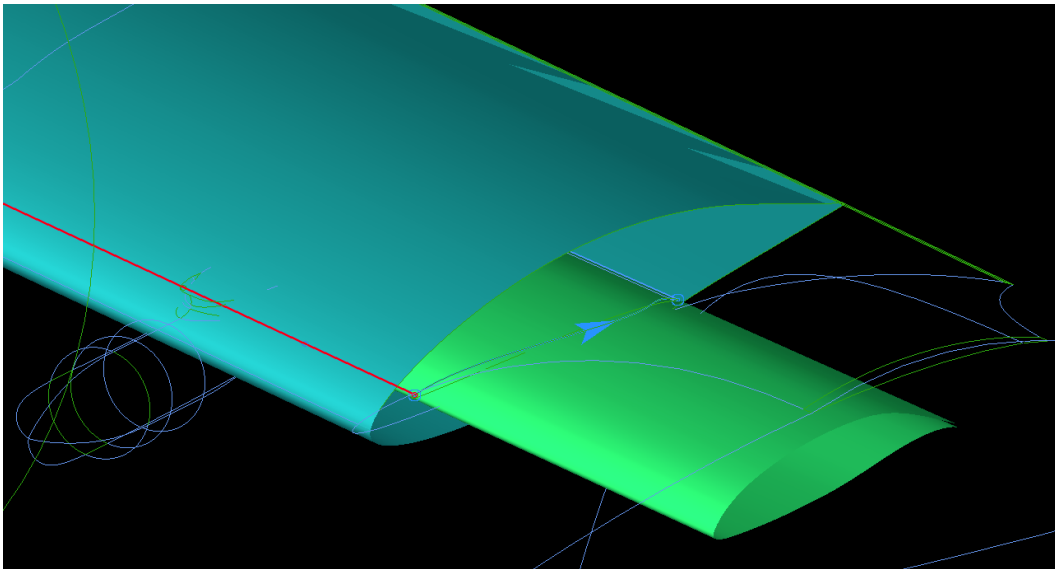
(b) Isometric View of Wing Root Region with the Smaller X-57 Wing Inside of the Tecnam Wing

Figure 12. Comparison of Tecnam Wing (blue) with the X-57 Wing (green).
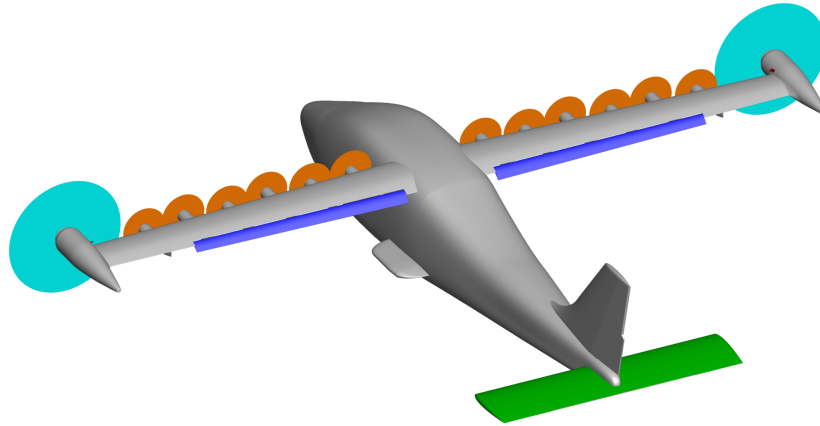
(a) Fullspan Geometry with a 30° Flap Deflection (blue), a Neutral Stabilator (green), No Aileron Deflection, DEP High-Lift Propellers (orange), and Cruise Propellers (cyan)
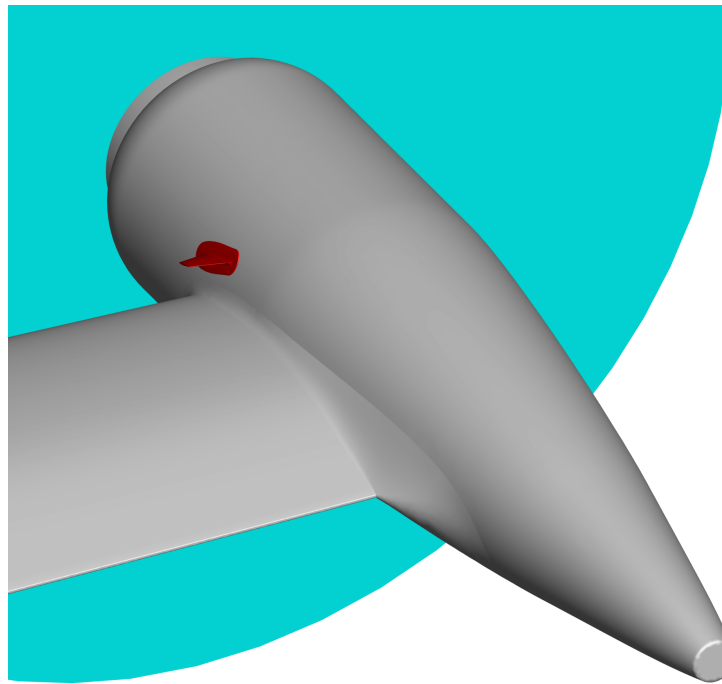
(b) Cruise Propeller (cyan) and Vortex Generator (red) on the Starboard Tip Nacelle

Figure 13. The Powered, X-57 Maxwell Mod IV Landing Configuration.

(a) $\delta_a = +18°$

(b) $\delta_a = +10°$

(c) δ_a = -5°

(d) δ_a = -10°

(e) δ_a = -15°

(f) δ_a = -25°
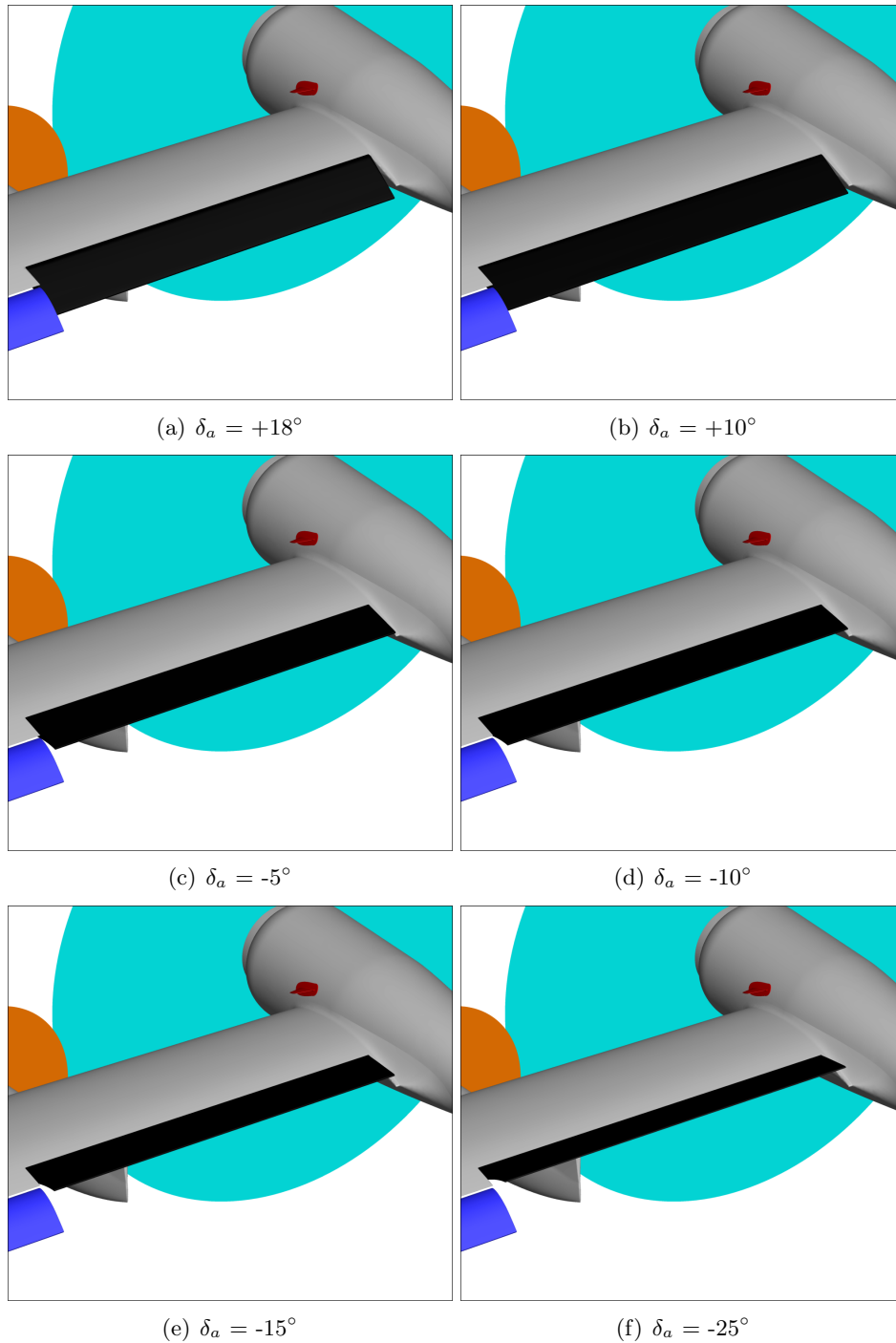
Figure 14. The Right Outboard Wing, Showing the Right Aileron Deflection in Black.

2.9 Grid Generation

The NASA LaRC GEOLAB also supported the grid generation effort in providing many of the meshes used in this investigation. The geometry definition was prepared in GridTool [27] by creating surface patches on the configuration and by placing sources throughout the domain to capture configuration characteristics. The sources are shown in yellow in Figure 15. The projectname.rst output file from GridTool was used to generate the computational domains with the Heldenmesh unstructured grid generation software, developed by Helden Aerospace Inc. [28].
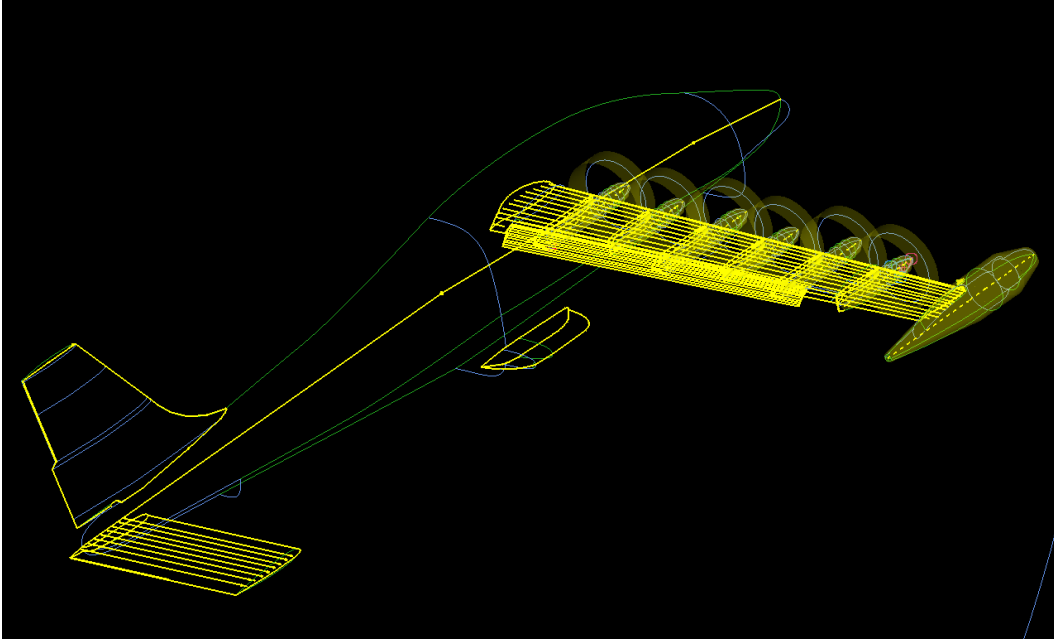
Figure 15. Placement of Sources for Defining Grid Resolution.

The GridTool software has an internal boundary-layer calculator that was used to generate the parameters needed to create the viscous portion of the mesh. The inputs to the calculator included the Reynolds number based on reference chord (Re_c), the reference chord (c_{ref}), a growth rate ($R2$), the nondimensional first node height (y_{node}^+), and the number of layers in the boundary layer. The outputs from the calculator included another growth rate ($R1$) and the dimensional first node height (δ_1).

The Heldenmesh software used an advancing layers method similar to reference [29] to create a boundary layer mesh of three cells per node (for a tetrahedral mesh) as the mesh propagated from the surface. An advancing front method, similar to reference [30], was used to generate the inviscid volume mesh from the boundary layer to the farfield. The volume growth rate was computed with Equation 1.

$$\delta_j = \delta_1[1 + R1(1 + R2)^{(j-1)}]^{(j-1)} \tag{1}$$

The Heldenmesh software produced an unstructured, tetrahedral mesh needed for USM3D. The three USM3D grid files were inputs to the CREATE-AV utility

called CARPENTER, which was used to generate the mixed-element mesh for Kestrel. The boundary layer cells of the all-tetrahedral mesh were merged into prisms for the Kestrel flow solver.

The high-lift workshop gridding guidelines [31] were used as a guide to generate the meshes in this study. The guidelines emphasized the number of cells along the wing and flap trailing edges should have at least 9 cells across the edge and a first cell height of $y_{cell}^+ = 0.44$ for a fine mesh. The computational domain was set at (-10,000 $\leq$ x $\leq$ 10,000), (0 $\leq$ y $\leq$ 10,000), and (-10,000 $\leq$ z $\leq$ 10,000), which was approximately 29 body lengths from the geometry.

For a better representation of the leading-edge curvature, it was important to use stretching along the wing leading edge to reduce the faceting that can occur from isotropic triangles on a curved surface [32]. The boundary layer spacing was specified for a $y_{cell}^+ < 1$ with 30 nodes for 90 cells across the boundary layer. The intent was to use the same mesh to run solutions for 58 KEAS through 133 KEAS and keep $y_{cell}^+ < 1$. The first cell height was $\delta_1 = 1.7e\text{-}4$ inches, which was computed for achieving $y_{cell}^+ = 0.6$ at 88 KEAS and an altitude of 2500 ft.

A semispan mesh was used to investigate the high-lift capability of the X-57 airplane, because the ailerons were neutral and the configuration was symmetric. A fullspan mesh was used to investigate roll effectiveness of the X-57 airplane since the geometry was asymmetric with the right aileron deflected and the left aileron remained neutral.

Since the surface mesh was very fine and it was difficult to show the mesh details on the full configuration in one picture, some representative mesh details are shown in Figures 16 and 17 for the landing configuration with $\delta_f = 30°$, and the landing configuration with $\delta_f = 30°$ and a $\delta_a = -25°$, respectively.

(a) Nose

(b) Empennage

(c) Inboard Wing, Nacelles 7-10

(d) Outboard Wing, Nacelles 11-12

(e) Wing Upper Surface at Root

(f) Top of Vertical Tail, Tstrip
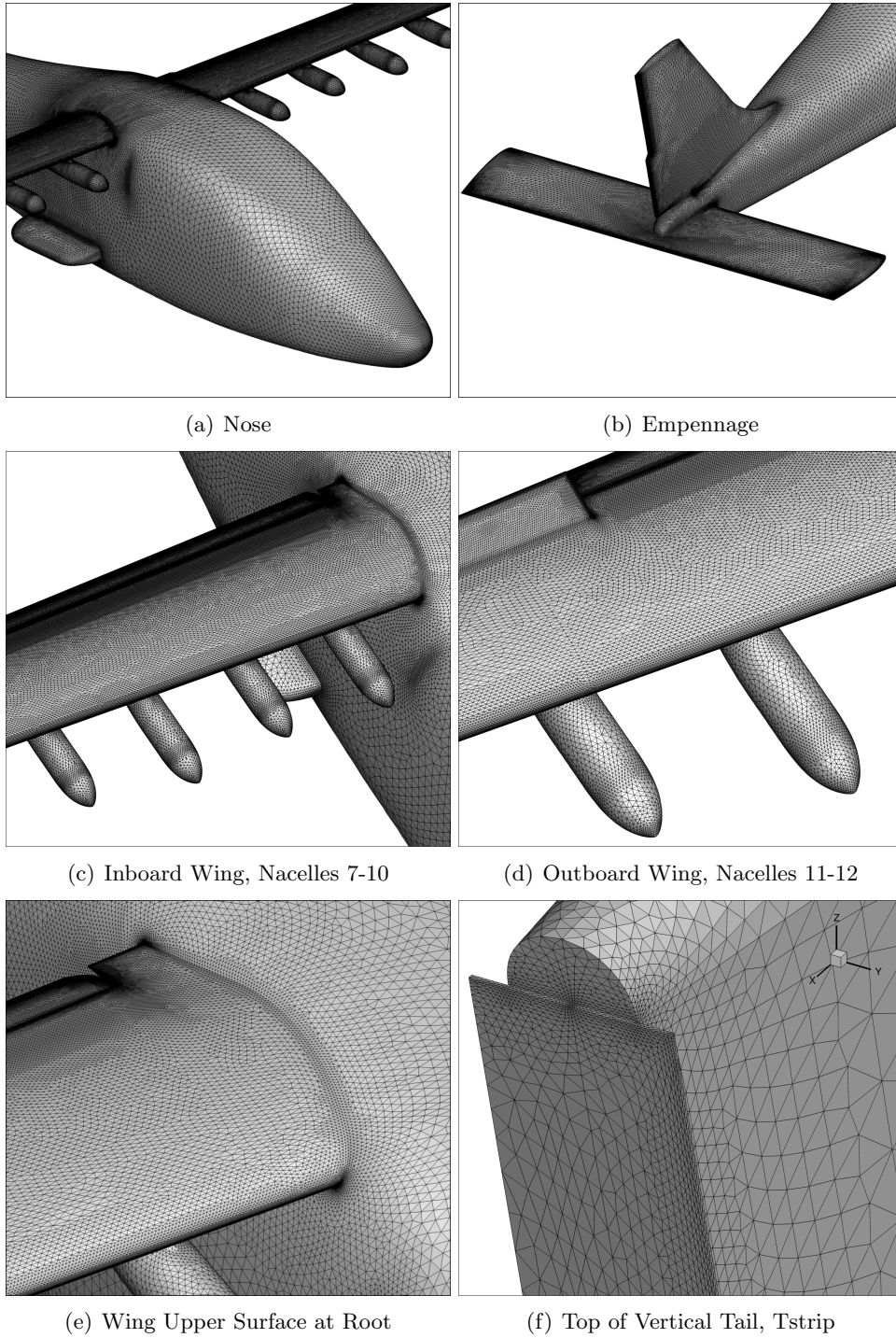
Figure 16. Surface Mesh for the Landing Configuration with $\delta_f = 30°$.
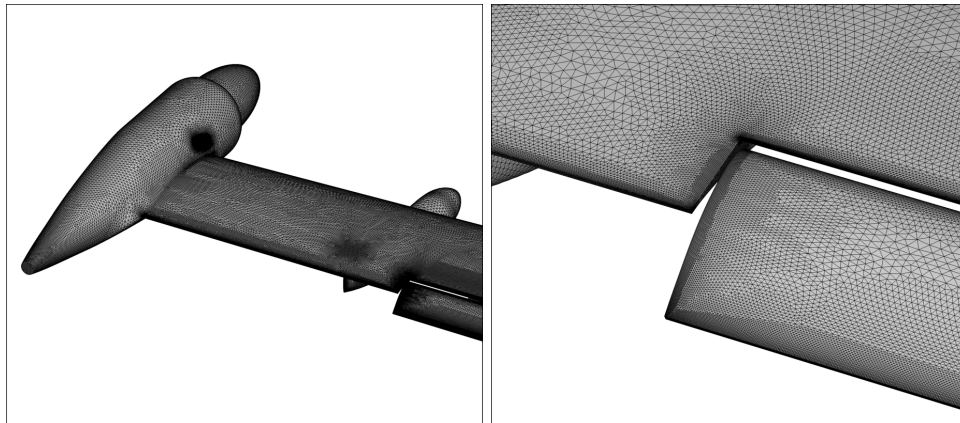
(a) Neutral Aileron, Left Wing

(b) Neutral Aileron, Left Wing, Zoom
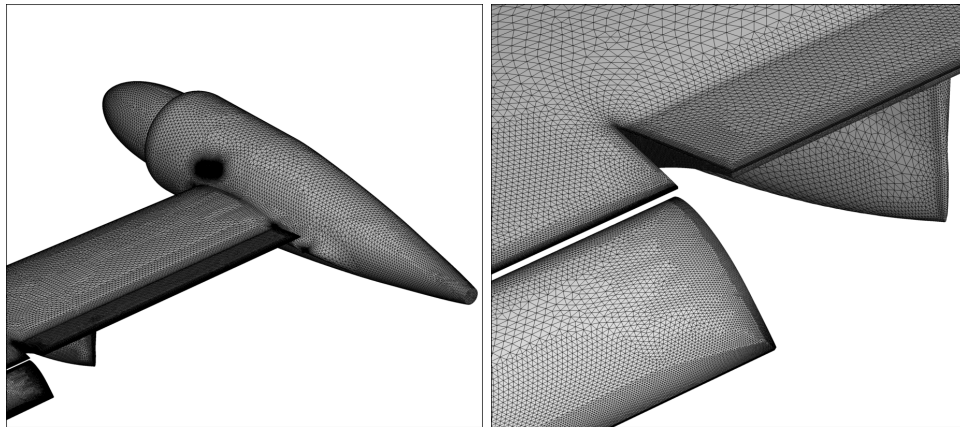
(c) Deflected Aileron, Right Wing

(d) Deflected Aileron, Right Wing, Inboard
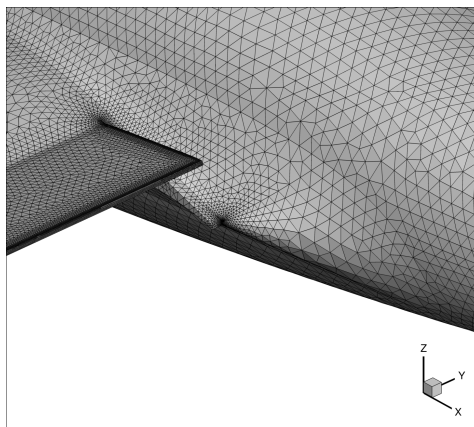
(e) Deflected Aileron, Right Wing, Outboard

Figure 17. Surface Mesh for the Landing Configuration with $\delta_f = 30°$, a Right Aileron $\delta_a = -25°$, and a Neutral Left Aileron.

2.9.1 Propeller Meshing

Propellers can be modeled in Kestrel and USM3D with an actuator disk boundary condition. Both codes required a circular patch, created within the mesh, onto which the actuator boundary condition was applied. Each propeller required an inflow and an outflow patch in the same location, as well as point-matching and face-matching between the meshes on the inflow and outflow patches. For each propeller, an inflow propeller patch was created in GridTool with the coordinates of the center of the propeller, with the diameter (D) of the propeller, and was given the patch name rotor. When the Heldenmesh software generated the grid, it duplicated each of the inflow patches called rotor, which created a point-matched and face-matched outflow patch. The authors used an approach of two cylinder-shaped volume sources at each propeller plane to cluster cells near the propeller to resolve the flow through the propeller and the wake. Figure 18 shows some of the volume sources used to mesh the nacelles (shown in yellow) and the propellers (highlighted in pink). One volume source extended two inches upstream of the rotor patches as shown as a pink ring in Figure 18(a). The second volume source extended seven inches downstream of the rotor patches as shown in Figure 18(b).

(a) Upstream Volume Source (b) Downstream Volume Source
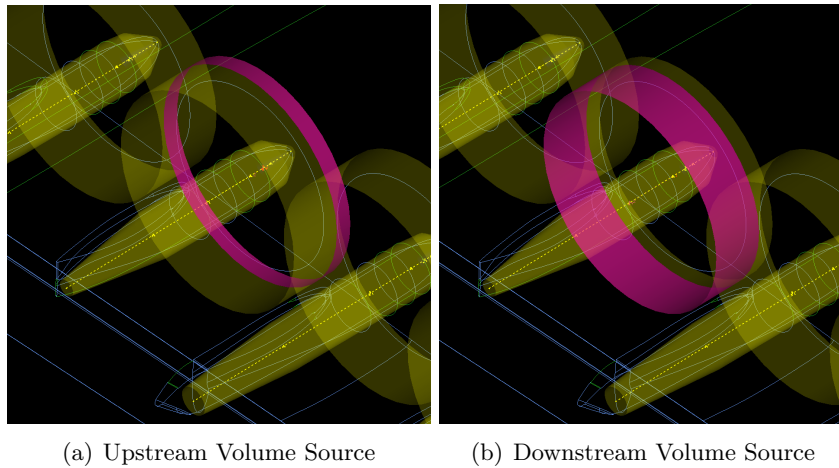
Figure 18. Example of Two Volume Sources Used for Propeller Meshing.

2.9.2 Propeller Meshing Grid Study

It was important to determine if extending the grid clustering in the propeller wake to downstream of the stabilator impacted lift, drag, and pitching moment coefficients. In previous work for the Mod II configuration, two grids were made to investigate the grid density in the wake of the propellers. Figure 19 shows the mesh on a plane at $y = 55$ inches for the two grids with the airplane facing to the right. The first grid (Figure 19(a)) had 185 million cells and had propeller meshing local to the propeller plane. The second grid (Figure 19(b)) had local propeller meshing and extended meshing to the trailing edge of the stabilizer. The second grid had 7 million extra cells through the propeller wake for a total of 192 million cells.

The Mod II data at $M = 0.1964$ from four cases at two angles of attack and thrust settings are shown in Tables 1 and 2 and will be used to discuss the effect of the two propeller meshing approaches on the aircraft and the stabilator aerodynamic coefficients. The tables show the effect of propeller mesh, localized cell clustering near the propeller plane (Local Meshing), compared to full-wake cell clustering to the trailing edge of the stabilator (Extended Meshing) on the forces and moment coefficients. There was less than 1% difference in aircraft lift, drag, and pitching moment coefficients between the local meshing and the extended meshing approaches for the 4 cases investigated. Therefore, the meshes in this paper were created with the local meshing approach for the propellers, and did not extend dense meshing across the stabilator. This approach may not work well for coarse volume meshes.
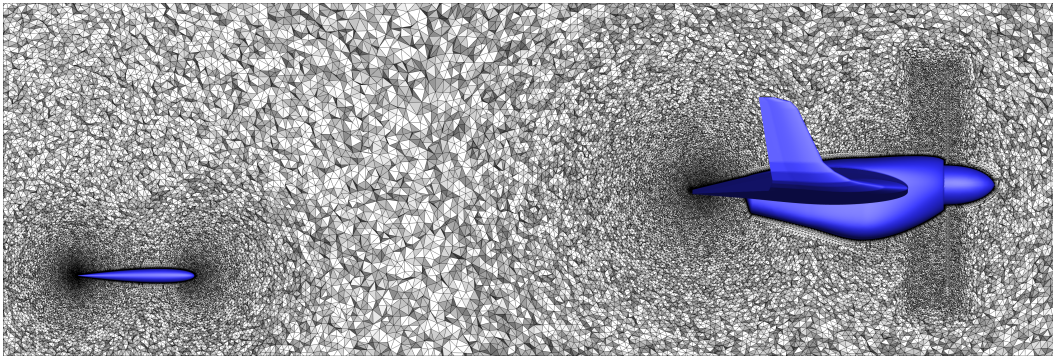
(a) Local Propeller Meshing
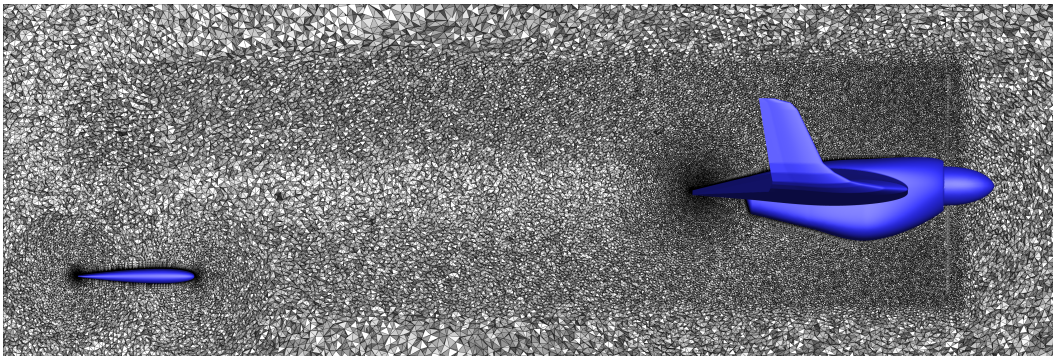
(b) Local Propeller Meshing and Extended Meshing to Trailing Edge of Stabilator

Figure 19. Mesh on a Plane at $y = 55$ inches for Two Meshing Approaches. Wing, Nacelle and Stabilator are shown in Blue.

Table 1. Effect of Propeller Grid Clustering on the Aircraft Forces and Moments, Mod II Configuration at $M = 0.1964$, USM3D SA.

Case	α deg.	T lbf.	Local Meshing C_L	C_D	C_m	Extended Meshing C_L	C_D	C_m	% Difference C_L	C_D	C_m
1	3.5	84.0	0.528	0.0328	-0.126	0.529	0.0329	-0.126	0.18	0.12	-0.14
2	3.5	161.8	0.535	0.0342	-0.128	0.535	0.0342	-0.128	0.14	0.11	-0.27
9	7.5	89.0	0.917	0.0574	-0.192	0.920	0.0578	-0.193	0.32	0.68	0.61
10	7.5	228.3	0.942	0.0629	-0.188	0.944	0.0631	-0.189	0.14	0.27	0.13

Table 2. Effect of Propeller Grid Clustering on the Stabilator Forces and Moments, Mod II Configuration at $M = 0.1964$, USM3D SA.

Case	α deg.	T lbf.	Local Meshing C_L	C_D	C_m	Extended Meshing C_L	C_D	C_m	% Difference C_L	C_D	C_m
1	3.5	84.0	0.025	0.0024	-0.087	0.025	0.0024	-0.087	-0.44	0.00	-0.45
2	3.5	161.8	0.026	0.0024	-0.090	0.026	0.0024	-0.089	-0.55	0.00	-0.57
9	7.5	89.0	0.051	0.0050	-0.172	0.050	0.0050	-0.173	0.24	0.00	0.25
10	7.5	228.3	0.049	0.0050	-0.169	0.049	0.0050	-0.169	-0.02	0.00	-0.01

2.10 Time Step

The Kestrel and USM3D codes were run with a global time stepping, time-accurate RANS approach. For USM3D nondimensionalization, the relationship for time step ($delta_t$) and the number of steps (N) to traverse a characteristic length (L_{char}) is shown in Equation 2. The distance a signal travels in one time step ($D_{t,char}$) is computed with Equation 3. The Kestrel manual recommends determining time step with Equation 4, with values of N in the range of 10–20 for steady state problems, and in the range of 50–100 for unsteady problems. For this work, a characteristic length of $L_{char} = 25.56$ inches was used with a value of $N = 25.56$ to get $D_{t,char} = 1$ inch/step. The authors felt this was an acceptable initial estimate since a local time stepping, steady-state RANS approach was used with the LAVA and STAR-CCM+ codes. A smaller time step was used to verify that the solution did not change.

$$delta_{t,USM3D} = \frac{L_{char}}{N * M} \tag{2}$$

$$D_{t,char} = \frac{L_{char}}{N} \tag{3}$$

$$delta_{t,KESTREL} = \frac{L_{char}}{V_\infty * N} \tag{4}$$

The USM3D time steps for 58 KEAS ($M = 0.098$) are shown in Table 3, along with the lift, drag, and pitching moment coefficient at $\alpha = 14°$. The differences in lift ($\Delta C_L = 0.0025$) and pitching moment ($\Delta C_m = 0.007$) coefficients between the two time steps were very small. Although the difference in drag was 22 counts, it was a very small percent of the total drag (0.3%). Therefore, the larger time step was deemed acceptable and used for the USM3D solutions to reduce the CPU time needed for a final solution.

Table 3. USM3D Time Step Information for 58 KEAS and Lift, Drag, and Pitching Moment Coefficients at $\alpha = 14°$.

$D_{t,char}$	$delta_{t,USM3D}$	N	C_L	C_D	C_m
1.00	10.2	25.56	4.2832	0.78237	-1.588
0.50	5.1	51.12	4.2857	0.78014	-1.595

The Kestrel time steps for 58 KEAS ($M = 0.098$, $V_\infty = 1286.2$ inches/sec) are shown in Table 4. A check on time step for Kestrel is discussed in the next section for Subiteration Selection. Similar to USM3D results, there was little difference in coefficients between the two time steps. Therefore, the larger time step was used to reduce resources since the smaller time step typically takes more CPU time.

2.11 Subiteration Selection

The Kestrel manual recommended using 1 subiteration for steady problems and 3 subiterations for unsteady problems. Additionally, there were up to 32 linear sweeps

Table 4. Kestrel Time Step Information for 58 KEAS.

$D_{t,char}$	$delta_{t,KESTREL}$	N
1.00	0.0008	25.56
0.50	0.0004	51.12

completed at each subiteration depending on when the solution met a convergence criteria of 1.0e-6. In order to determine the number of subiterations to use for this configuration, the results from 1 and 3 subiterations were compared at a high angle of attack where the difference in subiteration may be impactful.

Table 5 shows the effect of the number of subiterations on force and moment coefficients and solution time. The differences in lift and pitching moment coefficients between the two approaches were small; $\Delta C_L = 0.0049$ and $\Delta C_m = 0.0165$. Although the drag difference between the two subiteration approaches was 12 counts, it was a very small percent of the total drag (0.15%). Both of the solutions used 640 processors, but the difference in computational time was 14 hours. Therefore, the entire angle-of-attack sweep was computed with 1 subiteration for time savings, without a significant impact on force and moment coefficients expected.

Table 5. Effect of Number of Subiterations on Force and Moment Coefficients and Time at 58 KEAS ($M = 0.098$) and $\alpha = 14°$.

Subiteration	Time Step	C_L	C_D	C_m	Hours
1	0.0008	4.5787	0.82606	-1.3699	32
3	0.0004	4.5836	0.82486	-1.3534	46

2.12   Convergence

The convergence of each solution was judged with a drop in residuals and the standard deviation of time-averaged lift, drag, and pitching moment coefficients. In general, it was easier to judge convergence when a solution was steady because there was usually a large drop in residuals and the coefficients typically become constant with a very small standard deviation from the average. For steady problems, two main criteria were used to determine solution convergence; a drop in residual of two orders of magnitude and the convergence of force and moment coefficients to less than 0.5% change over a specified range of iterations. However, many of the solutions were unsteady and required engineering judgment in determining solution convergence. For the unsteady cases, the solutions were run until a statistical steady state was achieved and the average force and moment coefficients were computed over a reasonable time period.

2.12.1 Kestrel Convergence

Typical history plots used for evaluating convergence of Kestrel solutions are shown in Figure 20. The linear and nonlinear solution residuals are shown in Figures 20(a) and 20(b), respectively. It is difficult to see the initial drop in residuals for these plots unless the scale is changed to view the first 800 time steps, as is done in Figure 20(c) to show the 2 to 3 order of magnitude drop in residuals. The lift, drag, and pitching moment coefficients are shown in Figure 20(d) and the time-averaged values are shown in Figure 20(e). For this case, the time averaging was set to start at 10,000 time steps in the input file. Occasionally, the starting iteration for time averaging is not appropriate, and for such cases the authors have used Microsoft Excel software to compute the time-averaged values of the aerodynamic coefficients over an appropriate range of data. The Kestrel code does have a control file that can change the starting time step for time averaging, while the code is running if the user happens to check the solution history and determines it needs modification. Finally, flow contours for the solution were also evaluated to judge whether the solution appears to be converged of good quality, with no odd features appearing in the solution. Figure 20(f) shows typical C_p contours on the aircraft surface, and M contours at the propeller patches, with expected values of very low C_p on the blown wing. There was a ring of high M values for the DEP high-lift blowing propellers where the maximum thrust was set to $r/R_{prop} = 0.9$, and near freestream M contours for the idling cruise propeller.
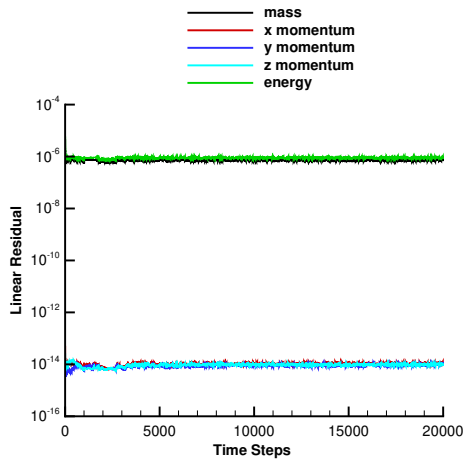
(a) Linear Residuals
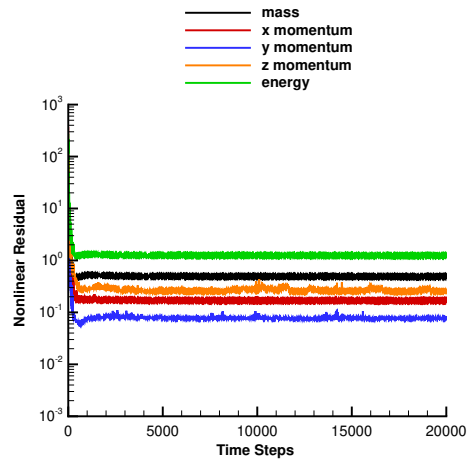
(b) Nonlinear Residuals
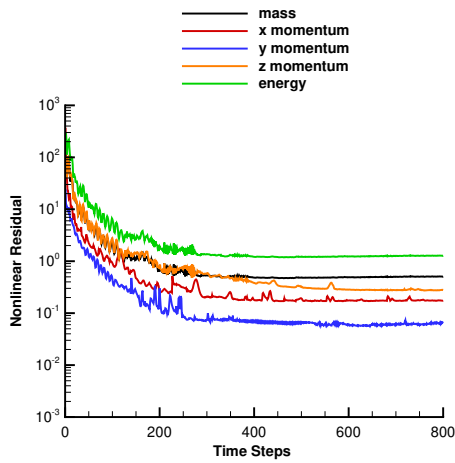
(c) Nonlinear Residuals to 800 Steps
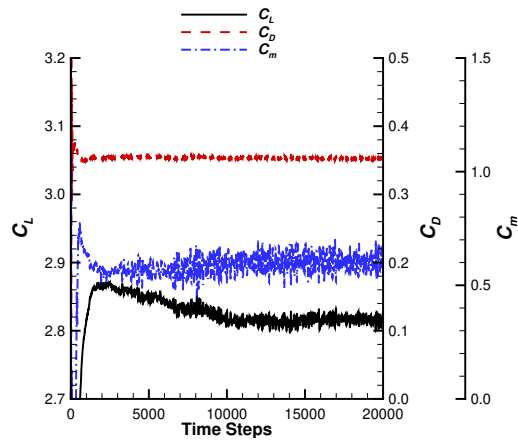
(d) Force and Moment Coefficients
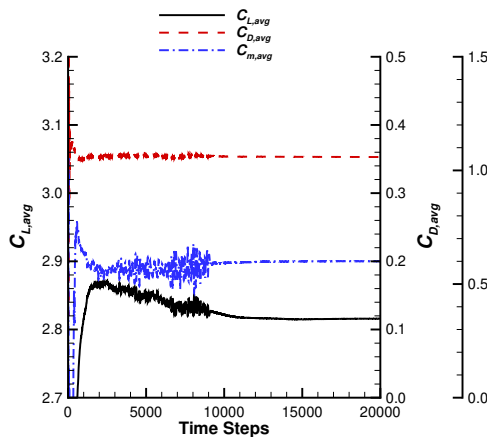
(e) Average Force and Moment Coefficients
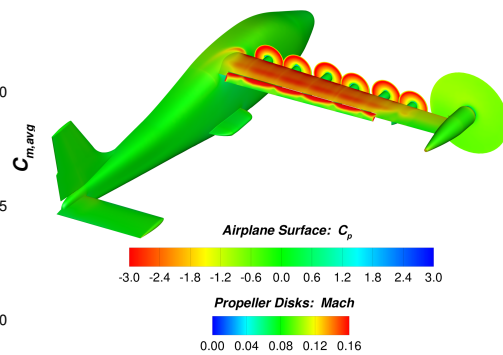
(f) Surface C_p and Propeller M Contours

Figure 20. Typical History Plots Used for Evaluating Convergence of the Kestrel (SA RC) Solutions. Landing Configuration at 58 KCAS, $\alpha = 2°$, with Idle Cruise Power (T = -8.02 lbf), and DEP High-Lift Blowing (T = 50.65 lbf).

2.12.2 USM3D Convergence

For USM3D solutions, the coefficients were averaged over a range of 2,000 iterations for steady solutions and at least 5,000 iterations for unsteady solutions. The standard deviation and the percent over range (POR) were also calculated for each coefficient over the specified range. The POR was calculated with Equation 5, where the $C_{(N,max-(range))}$ and the $C_{N,max}$ are the values of the coefficient at the first and last iterations of the range, respectively.

$$POR = \left(\frac{C_{N,max} - C_{(N,max-(range))}}{C_{average}} \right) * 100 \qquad (5)$$

$$C_{average} = \frac{1}{range} \sum_{j=N_{max}-range}^{N_{max}} (C_j) \qquad (6)$$

Steady solutions were deemed converged when the POR values were less than 0.5. In the situation where the coefficient was approaching zero, the POR values may be larger than 0.5% because of the near zero average value of the coefficient in the denominator of Equation 6. These higher POR calculations when the average was near zero can be deceiving, and therefore, engineering judgment was used with the standard deviation to determine if properly converged with POR $> 0.5\%$.

An example of force and moment convergence data for a steady case is shown in Table 6. In this example for the landing configuration with high-lift blowing at 58 KEAS and $\alpha = 0°$, the solution was well converged with POR $< 0.03\%$ for C_L, C_D, and C_m

Table 6. Typical Convergence Data for a Steady Solution. Landing Configuration at 58 KEAS, $\alpha = 0°$, No Cruise Power, High-Lift Blowing ($T = 50.65$ lbf), USM3D SA QCR.

Calculation	C_L	C_D	C_m
Average	2.5905	0.2706	1.0176
Standard Deviation	20e-06	3e-06	70e-06
POR	0.0019	0.0018	0.0226

A grouping of plots used to evaluate convergence is shown in Figure 21. This solution was started with first-order flux calculations for the first 10,000 iterations, and then continued with a second-order scheme. Figure 21(a) shows excellent residual convergence. The mean-flow residuals ($r/r0$) drop three orders of magnitude during the first-order flux scheme, and drops another two orders of magnitude during the second-order scheme. The turbulence residuals ($tn/tn0$) drop one order of magnitude during the first-order flux scheme, and another four orders of magnitude drop during the second-order scheme. The force and moment coefficients shown in Figure 21(b) indicate excellent convergence as expected from the data calculations in Table 6. The subiteration residual convergence data in Figure 21(c) show that for each time step at 54,200 iterations, the mean flow and turbulence residuals are

dropping three and six orders of magnitude, respectively. Finally, Figure 21(d) shows the normalized U velocity contours in the x direction, at the first cell above the surface. The normalized U velocity contours are computed by dividing the dimensional U velocity by the dimensional freestream speed of sound. Values of $U < 0$, were removed from the plot such that flow separation was easily viewed when the gray-shaded surface was visible. This figure shows fully attached flow on most of the configuration except for some regions of flow separation on the flap.

(a) Residuals

(b) Force and Moment Coefficients

(c) Subiteration Residuals

(d) Normalized U Velocity
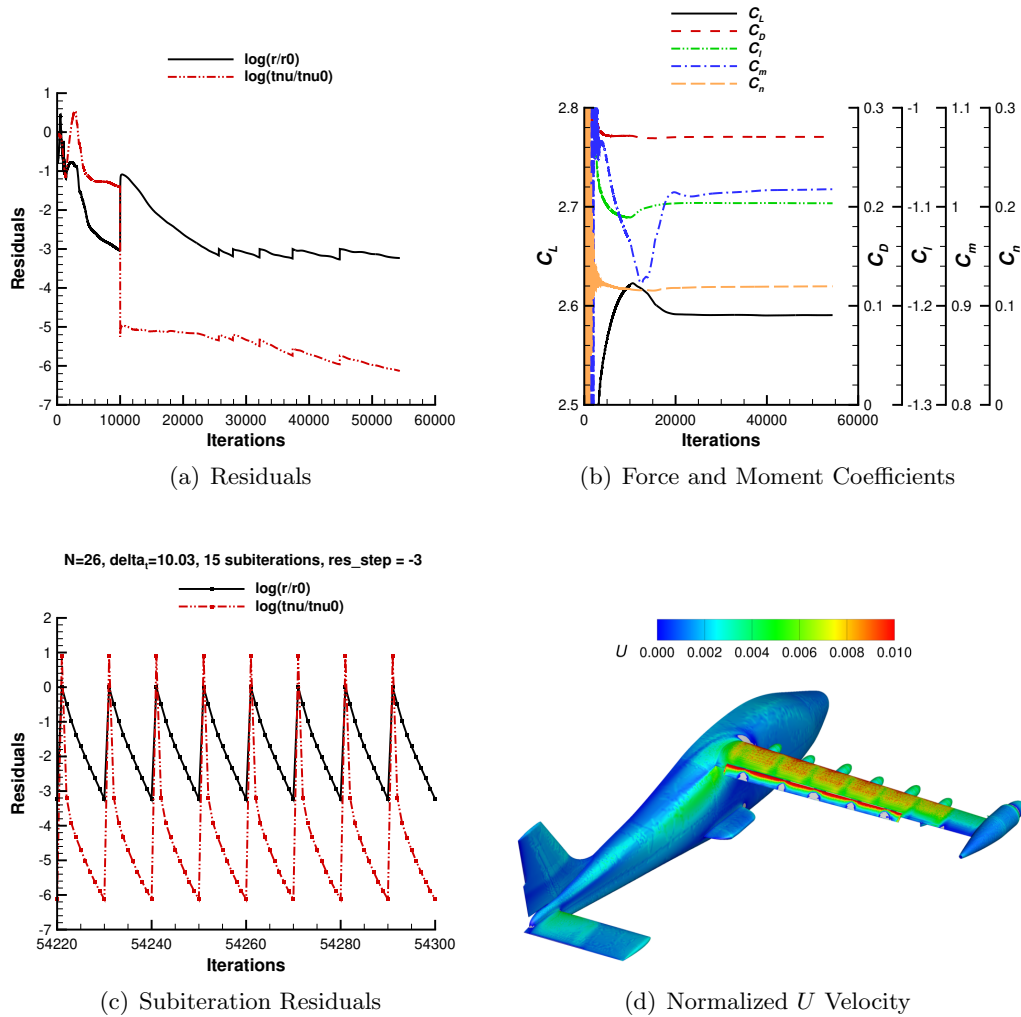
Figure 21. Typical History Plots Used for Evaluating Convergence of USM3D (SA QCR) Solutions. The Landing Configuration with $\delta_f = 30°$, 58 KCAS, $M = 0.098$, $\alpha = 0°$, No Cruise Power, and DEP High-Lift Blowing.

3 Results

The majority of the data shown in this study were computed at NASA LaRC using Kestrel and USM3D. Additionally, the X-57 CFD team results from STAR-CCM+ and from LAVA [19–21] were included with permission in Sections 3.5 and 3.6. All data in this paper were computed for the landing configuration with a flap deflection at $\delta_f = 30°$, at freestream conditions of $M = 0.098$, 58 KEAS, an altitude of 6000 feet, and a flight Reynolds number of 1.25E+06 based on the mean aerodynamic chord of 25.56 inches. The DEP high-lift system conditions for each propeller were 5035 RPM with a thrust of $T = 50.65$ lbf, a torque of $Q = 16.23$ lbf-ft, and a power of $P_{out} = 11.6$ kW.

The results are presented in seven sections. First, some insights on understanding the lift and drag coefficients for the X-57 Maxwell are presented in Section 3.1. The effects of high-lift blowing on lift and drag are discussed in Section 3.2. The effects of including or excluding the idling, windmilling cruise propellers are shown in Section 3.3. The aerodynamic performance with high-lift blowing from the DEP system and a neutral aileron are shown in Section 3.4. The results from four CFD codes are discussed in Section 3.5 for the aerodynamic performance with high-lift blowing and a neutral aileron. The aileron roll effectiveness from a right aileron deflection with the DEP high-lift system operating is presented in Section 3.6. Finally, the effect of aileron deflection on aerodynamic configuration performance with high-lift blowing and the cruise propellers excluded is shown in Section 3.7.

3.1 Understanding the X-57 Maxwell Powered Lift Coefficient and Drag Coefficient Trends

The basic X-57 wing was designed to operate in a lift coefficient range that is different than typical General Aviation (GA) wings. Compared to the Tecnam P2006T base airplane, the X-57 wing area was reduced by 58%, from $S_{ref} = 158.9$ feet^2 to $S_{ref} = 66.67$ feet^2. In addition, the gross weight of the X-57 was increased from 2,700 lbs to 3,000 lbs to accommodate the battery weight. These factors increased the wing loading (W/S) from $W/S = 17.0$ lbs/feet^2 for the Tecnam, to $W/S = 45.0$ lbs/feet^2 for the X-57. Therefore, the cruise C_L was increased from $C_L = 0.28$ to $C_L = 0.75$. Wing camber can be increased on the basic airfoil to adjust the C_L for minimizing cruise drag, but unfortunately there are upper limits to $C_{L,max}$ and the X-57 cruise C_L moves closer to the maximum C_L limit as camber increases, and reduces the available margin between cruise C_L and $C_{L,max}$. This increases the chance for trailing-edge separation at lift coefficients not far above the $C_{L,cruise}$. In addition, reducing the wing area and increasing the aspect ratio reduces the wing chord of the X-57 Maxwell significantly. The X-57 mean aerodynamic chord is 2.13 feet. The Reynolds number is 6.62 million at cruise, but only 1.25 million at low speeds for landing. The low operating Reynolds numbers also increase the chance for trailing-edge separation even at moderate angles of attack.

With these facts about the geometry and the flow conditions of the X-57 wing, let's now examine the lift and drag coefficients from the USM3D CFD solutions. The lift and drag coefficient data versus angle of attack are presented in Figure 22

44

for three different X-57 configurations:

1. Cruise, Without High-Lift Blowing: undeflected flap (basic cruise wing), and no high-lift blowing augmentation

2. Flap 30°, Without High-Lift Blowing: wing landing configuration with a 25% slotted flap deflected 30°, and no high-lift blowing augmentation

3. Flap 30°, With High-Lift Blowing: wing landing configuration with a 25% slotted flap deflected 30°, and DEP high-lift propellers operating at maximum power

Comparison of data between configurations 1 and 2 provides the effect of flap deflection, while the comparison between configurations 2 and 3 provides the benefit of powered lift. Solid lines are used to represent the USM3D CFD C_L and C_D data for the three configurations.

Comparing C_L for the unblown configurations in Figure 22(a), it can be seen that the 30° flap deflection adds a linear increment of approximately $\Delta C_L = 0.84$ up to $\alpha = 10°$ relative to the cruise wing. The $C_{L,max}$ is near $\alpha = 10°$ for the unpowered 30° flap configuration and Figure 23 shows some flow contours for this condition. Figure 23(a) shows Mach contours at several spanwise locations and Figure 23(b) shows surface streamlines overlaid above the pressure coefficient contours. For $\alpha > 10°$, wingroot flow separation spreads outward onto the wing and reduces lift, as seen in Figure 24 for $\alpha = 12°$. Above $\alpha = 14°$, there is another reduction in lift as the flow separation on the unblown wing moves forward toward the leading edge between the two inboard nacelles, as shown in Figure 25 for $\alpha = 15°$. When DEP high-lift blowing is added to the 30° flap landing configuration, there is not only a significant lift increment compared to the unblown 30° flap configuration ($\Delta C_L = 1.1$ at $\alpha = 0°$), but in addition, there is an increase in the lift-curve slope (Figure 22(a)). Note that this increase in lift-curve slope is not constant, and the powered lift-curve slope drops off with increasing angle of attack.

These trends are compared with linear lift theory and the flat plate lift-curve slope of 2π/radian in Figure 22. On the lift curve plot in Figure 22(a), the linear lift theory is added (dotted straight lines) according to Equation 7. The configuration lift at zero degrees angle of attack (C_{Lo}) is computed from the CFD data by interpolating between negative and positive angles of attack for each configuration. For angles of attack up to 10°, the CFD lift curve data follow the linear theory fairly well for both the cruise configuration and the unblown 30° flap configuration. However, for the powered lift case with 30° flap and DEP high-lift blowing, the lift-curve slope is larger than the 2π/radian theory. Therefore, a multiplier of 1.9 was included to the lift-curve slope for the 30° flap DEP high-lift blowing case to match the initial lift-curve slope at low angles of attack. As stated before, as angle of attack is increased, the lift-curve slope rolls off but is not too different than the linear approximation up to about $\alpha = 6°$. As can be seen in the comparison of Figures 26 and 27 for $\alpha = 2°$ and the comparison of Figures 28 and 29 for $\alpha = 8°$, the increase in lift-curve slope occurs because the powered lift increases the turning of the flow compared to the unpowered cases.

The USM3D CFD drag coefficient for the three configurations is shown in Figure 22(b) with solid lines. Note that the wing area is the characteristic dimension for conversion of forces to coefficients. Therefore, the value of the X-57 drag coefficient is much larger than the Tecnam drag coefficient (52% higher), even if the two configurations had the same physical drag value. The high value of the zero-lift drag coefficient (C_{Do}) and the high operating lift coefficients push the actual value of the drag coefficient to a higher range than is typical for GA aircraft. The CFD drag data can be compared to the simple drag theory of the base configuration drag plus induced drag, as presented in Equation 8. The zero-lift drag coefficient was estimated by taking the CFD drag coefficient for the lowest analyzed angle of attack and subtracting off $C_L{}^2/(\pi e AR)$. Up to about $\alpha = 10°$, the drag versus angle of attack for all three configurations compares with the simplified zero-lift drag plus induced drag theory (Equation 8). The CFD drag for the cruise and $30°$ flap no high-lift blowing configurations are slightly higher than the simplified theory up to $\alpha = 10°$, which can be expected for an increase in aft boundary layer thickness and the start of trailing-edge flow separation at these low airfoil Reynolds numbers. After $\alpha = 10°$, this effect is more pronounced and the CFD drag increases significantly over the simplified drag theory curves. For the $30°$ flap DEP high-lift blowing configuration, the CFD drag versus α compares very well to the simplified theory curve over the angle-of-attack range, even up to $\alpha = 20°$. This appears to be a coincidence though, because the CFD lift curve continuously drops off from the linear lift curve for $\alpha > 5°$. However, the CFD drag coefficient compares well to the simplified theory for $\alpha < 7°$. Also note that with these very high zero-lift drag coefficients and the larger lift coefficients, the trend in the C_D versus α appears almost linear, in contrast to parabolic trends for the C_D versus α curve.

$$C_L = C_{L_\alpha} \alpha_{deg} + C_{L_o} \tag{7}$$

$$C_D = C_{D_o} + \frac{C_L{}^2}{\pi e AR} \tag{8}$$
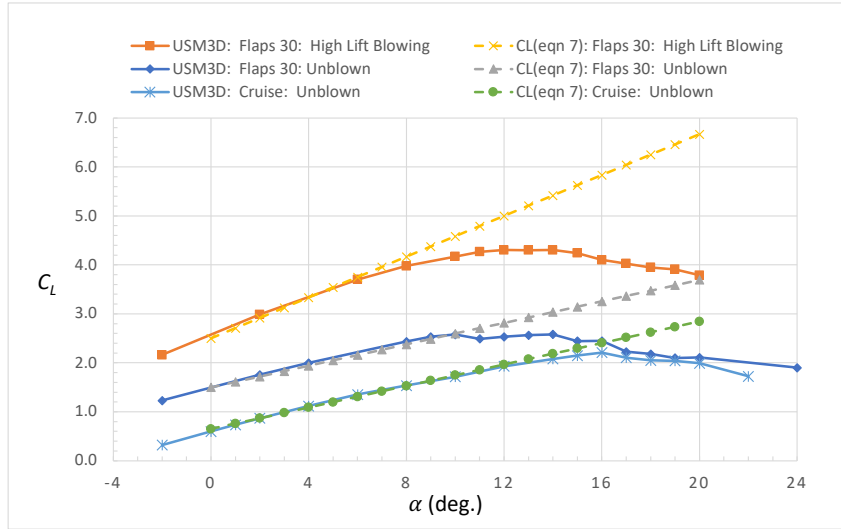
(a) Lift
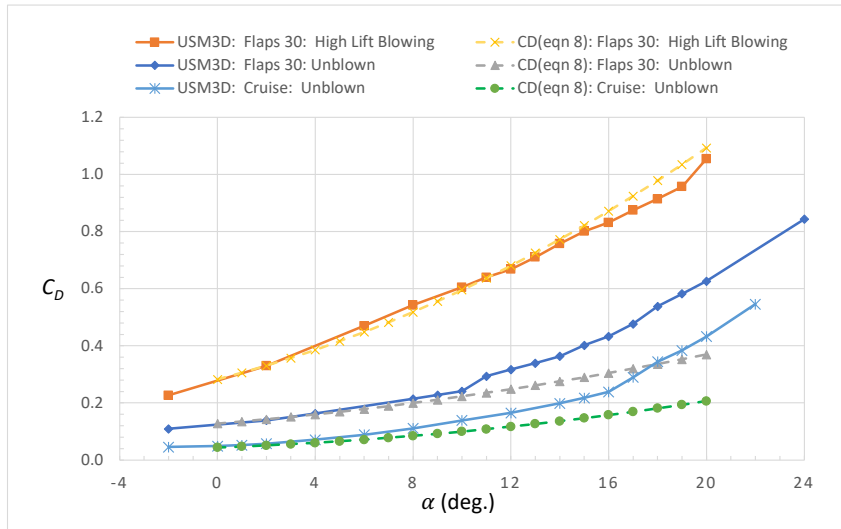
(b) Drag

Figure 22. The Effects of Flap Deflection and High-Lift Blowing on Lift and Drag. Landing Configuration with No Aileron Deflection. Flaps 30° High-Lift Blowing Results with a Freestream at 58 KEAS. Flaps 30° Unblown Results with a Freestream at 88 KEAS. Cruise Unblown Results at 133 KEAS, USM3D SA QCR.

(a) Mach Contours   (b) Streamlines on Pressure Coefficient

Figure 23. Landing Configuration with No Aileron Deflection, 88 KEAS, $\alpha = 10°$, and No High-Lift Blowing, USM3D SA QCR.

(a) Mach Contours   (b) Streamlines on Pressure Coefficient

Figure 24. Landing Configuration with No Aileron Deflection, 88 KEAS, $\alpha = 12°$, and No High-Lift Blowing, USM3D SA QCR.

(a) Mach Contours   (b) Streamlines on Pressure Coefficient

Figure 25. Landing Configuration with No Aileron Deflection, 88 KEAS, $\alpha = 15°$, and No High-Lift Blowing, USM3D SA QCR.

(a) nacelle, wing, and flap view

(b) flap view

Figure 26. Normalized Velocity at y = 57 inches. Landing Configuration with No Aileron Deflection, 88 KEAS, $\alpha = 2°$, and No High-Lift Blowing, USM3D SA QCR.

(a) nacelle, wing, and flap view

(b) flap view

Figure 27. Normalized Velocity at y = 57 inches. Landing Configuration with No Aileron Deflection, 58 KEAS, $\alpha = 2°$, with High-Lift Blowing, USM3D SA QCR.

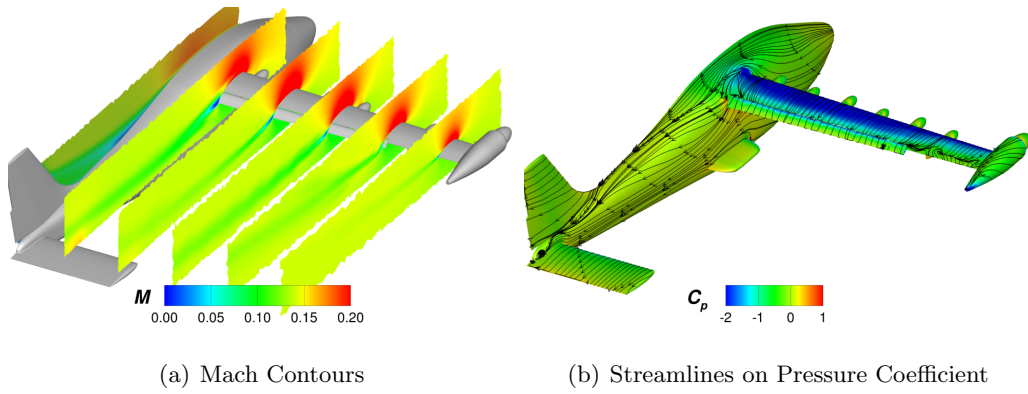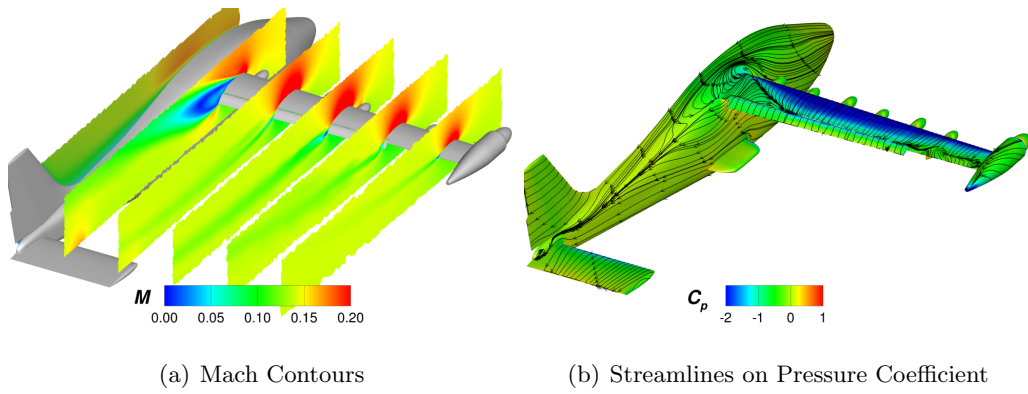(a) nacelle, wing, and flap view

(b) flap view

Figure 28. Normalized Velocity at y = 57 inches. Landing Configuration with No Aileron Deflection, 88 KEAS, $\alpha = 8°$, and No High-Lift Blowing, USM3D SA QCR.

(a) nacelle, wing, and flap view
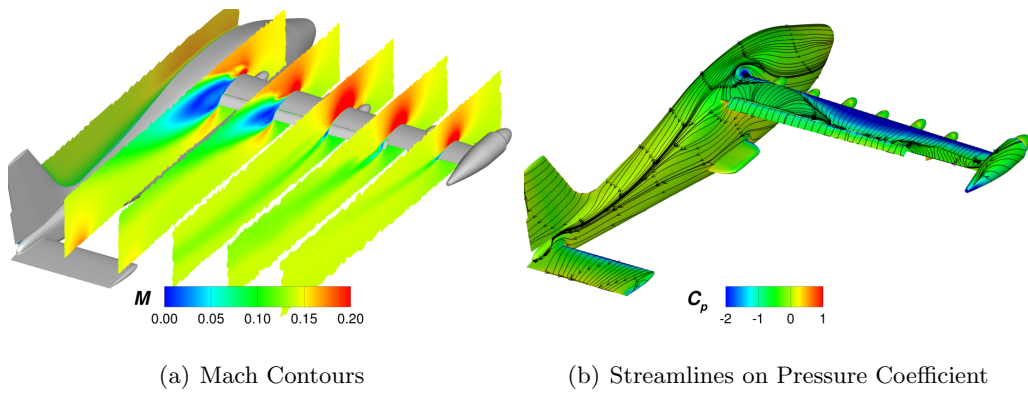

(b) flap view

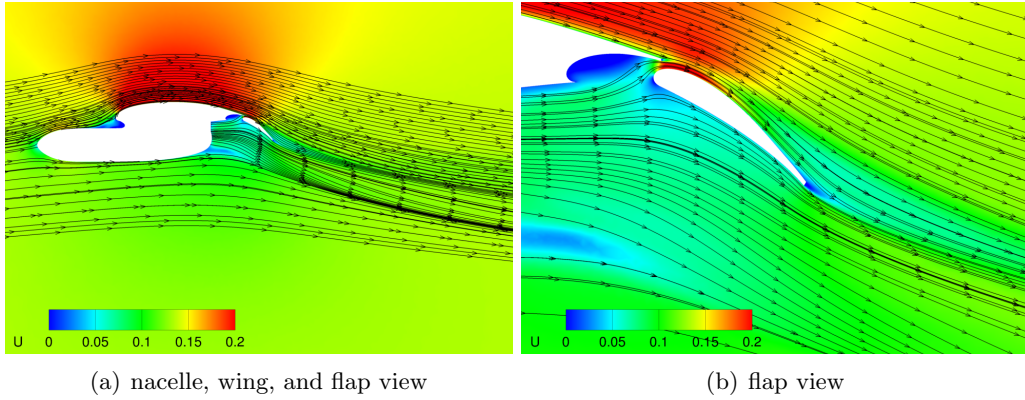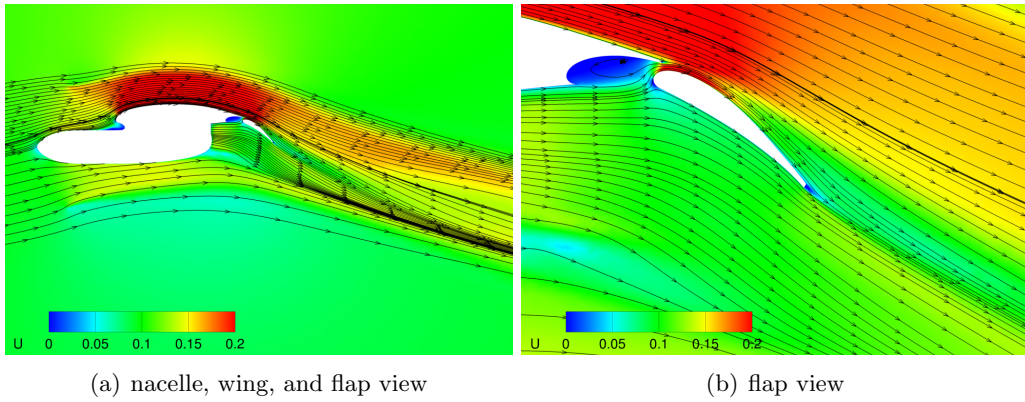Figure 29. Normalized Velocity at y = 57 inches. Landing Configuration with No Aileron Deflection, 58 KEAS, $\alpha = 8°$, with High-Lift Blowing, USM3D SA QCR.
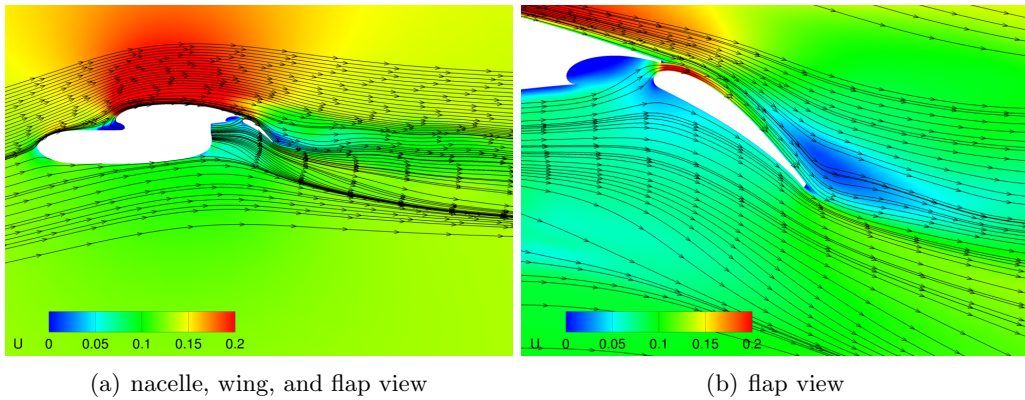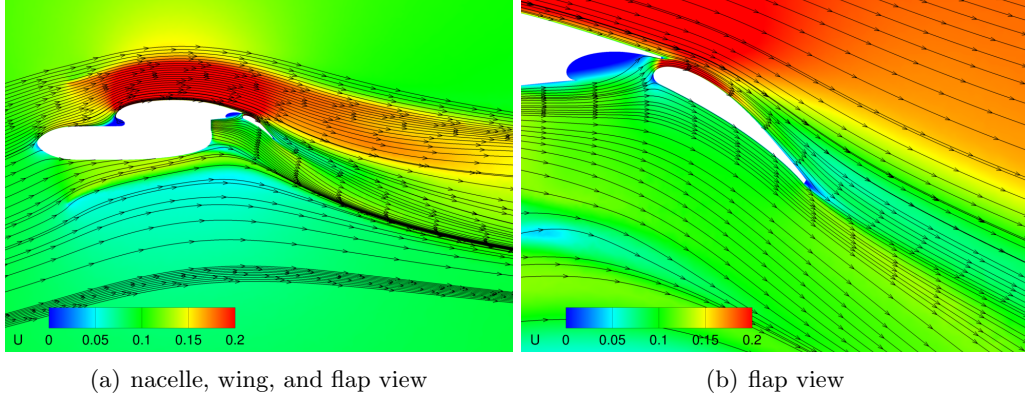
3.2 Effects of High-Lift Blowing on Component Contributions to Lift and Drag

Figure 30 shows the effects of high-lift blowing on the major component contributors to lift and drag. The data with solid symbols in Figure 30(a) and Figure 30(c) represent the high-lift blowing data, while the unfilled symbols represent the data without high-lift blowing (unblown). Figure 30(b) shows ΔC_L, as computed as the difference in lift between the solutions with and without high-lift blowing. Figure 30(d) shows the ΔC_D, as computed as the difference in drag between the solutions with and without high-lift blowing.

Figure 30(a) shows that, as expected, the wing is the main contributor to lift at high-lift blowing and unblown conditions. The stabilator has an increasing contribution to lift with increasing angle of attack, and $C_L = 0$ at $\alpha = 8°$ and $\alpha = 10°$ for the unblown and high-lift blowing conditions, respectively.

For unblown conditions, the flap and fuselage have equal contributions to lift at $\alpha = 4°$, with the flap having higher lift for $\alpha < 4°$ and the fuselage having higher, relatively constant lift for $\alpha > 4°$. Also at unblown conditions, as angle of attack increases beyond $\alpha = 4°$, the fuselage has a slightly increasing contribution to lift, except for a drop in lift at $\alpha = 11°$ when the wingroot flow separation influences the flow on the fuselage near the wingroot. Finally, the unblown flap has a maximum contribution to lift at $\alpha = -2°$ and lift decreases slightly with increasing angle of attack, although the contribution to lift is mostly constant for $\alpha > 12°$.

For the high-lift blowing conditions, the flap and fuselage have equal contributions to lift at $\alpha = 8°$, with the flap having higher lift for $\alpha < 8°$ and the fuselage having a higher and mostly constant lift for $\alpha > 8°$. The effect of high-lift blowing on lift shown in Figure 30(b) indicates the largest increase in lift from high-lift blowing is from the wing. In general, the change in lift increases with increasing angle of attack, providing a minimum boost in lift of $\Delta C_L = 0.66$ at $\alpha = -2°$ and a maximum increase in lift of $\Delta C_L = 1.5$ at $\alpha = 19°$. It is surprising that the effect of high-lift blowing on lift for the flap is relatively constant at $\Delta C_L = 0.3$ for $\alpha < 10°$ and declines with increasing angle of attack to $\Delta C_L = 0.1$ for $\alpha = 20°$. The high-lift

blowing increases lift from the fuselage by $\Delta C_L = 0.1$–0.2, but reduces lift on the stabilator with a relatively constant reduction in lift of $\Delta C_L = 0.05$–0.1 across angle-of-attack range.

Figure 30(d) shows that the largest contributors to drag from high-lift blowing are from the flap for $\alpha < 12°$ and from the wing for $\alpha > 12°$. There is an increasing contribution to drag from the fuselage and stabilator with increasing angle of attack (Figure 30(c)), however, there is little to no change in drag from unblown to blown-wing conditions for the fuselage and stabilator (Figure 30(d)).

(a) Lift

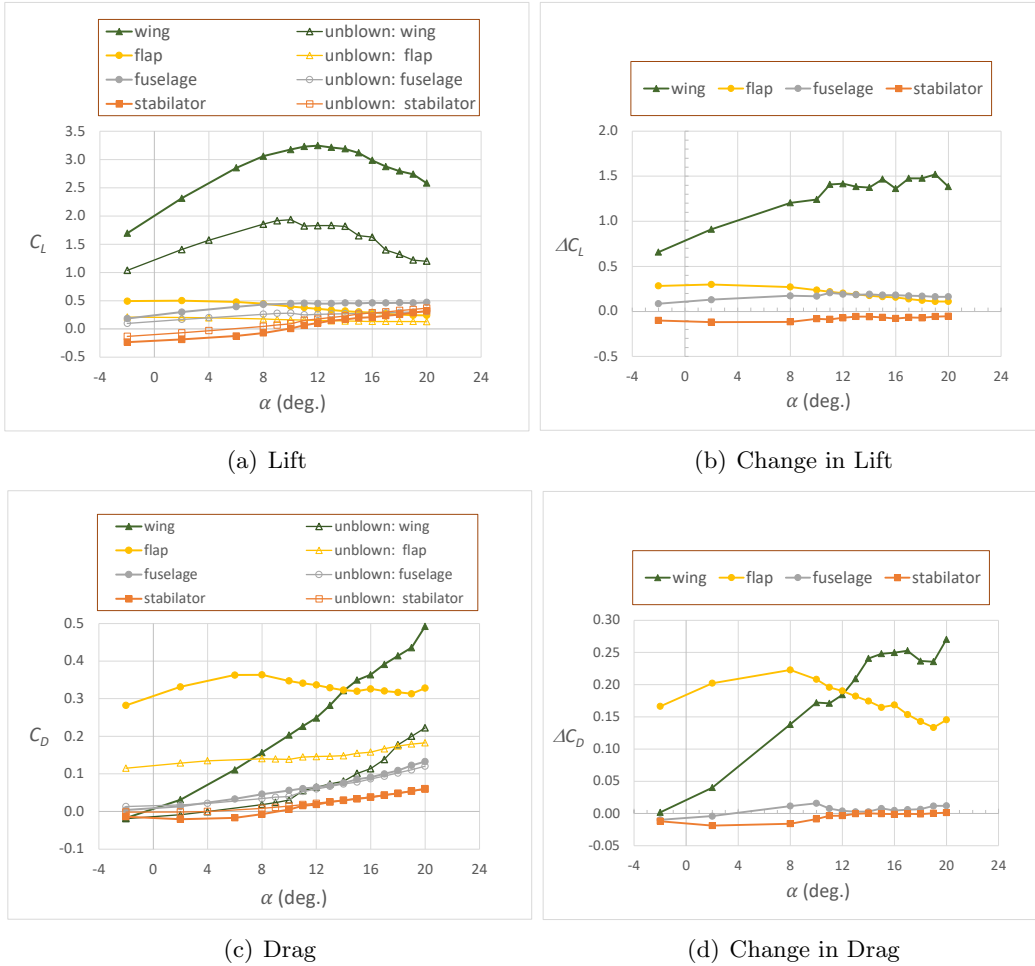(b) Change in Lift

(c) Drag

(d) Change in Drag

Figure 30. The Effects of High-Lift Blowing on Component Lift and Drag. Landing Configuration No Aileron Deflection. Blown Wing Results with a Freestream at 58 KEAS. Unblown Wing Results with a Freestream at 88 KEAS, USM3D SA QCR.

3.3 Cruise Power Propeller Modeling

For landing with the DEP high-lift system, the cruise propellers were intended to be in an idling, windmilling state with the conditions set at 1540 RPM, a thrust of $T = $ -8.02 lbf, and a torque of $Q = 0.65$ lbf-ft. It was hypothesized that the idling cruise propellers could be excluded altogether for these calculations.

To verify the hypothesis, new Kestrel solutions were computed for an α sweep with the cruise propellers idling and the high-lift propeller conditions at 5035 RPM, $T = 50.65$ lbf, and $Q = 16.23$ lbf-ft. For a quick assessment, the new solutions were compared with previous Kestrel solutions where the cruise propeller were excluded, even though the high-lift propeller conditions were slightly different (4702 RPM, $T = 49.3$ lbf, and $Q = 16$ lbf-ft). First, there was negligible impact from the difference in high-lift propeller conditions on pressure coefficient on the upper surface of the wing, even though there were slightly different velocities in the propeller plane, as shown in Figure 31 for $\alpha = 10°$. Second, Figure 32 shows the negligible differences in lift, drag, and pitching moment coefficients between the Kestrel results for the cruise propellers included or excluded. Since neither excluding the cruise propellers, nor the slight difference in high-lift propeller conditions had an impact on lift, drag, and pitching moment coefficients, it was concluded that the idle cruise propellers could be excluded from additional solutions.

As a further assessment using USM3D with the SA QCR turbulence model, solutions were computed at angles of attack of $\alpha = 2°$, $\alpha = 14°$, and $\alpha = 18°$ for either the cruise propellers modeled as idling or excluded from the simulation, with the high-lift propeller conditions at 5035 RPM, $T = 50.65$ lbf, and $Q = 16.23$ lbf-ft. The USM3D results also indicate negligible differences in C_L and C_D, and small differences in C_m whether the propellers were included or were excluded from the solution, as shown in Figure 33. Therefore, the full angle of attack sweep was computed without the cruise propellers in the USM3D simulations.
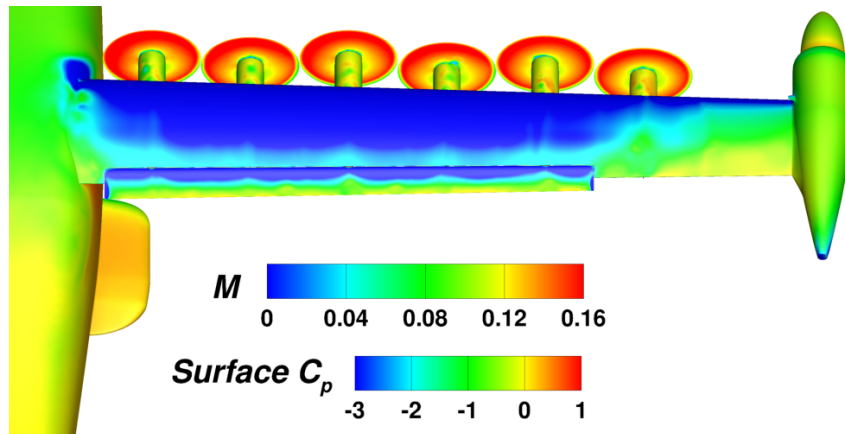
(a) High-Lift Propellers at 5035 RPM and 50.65 lbf
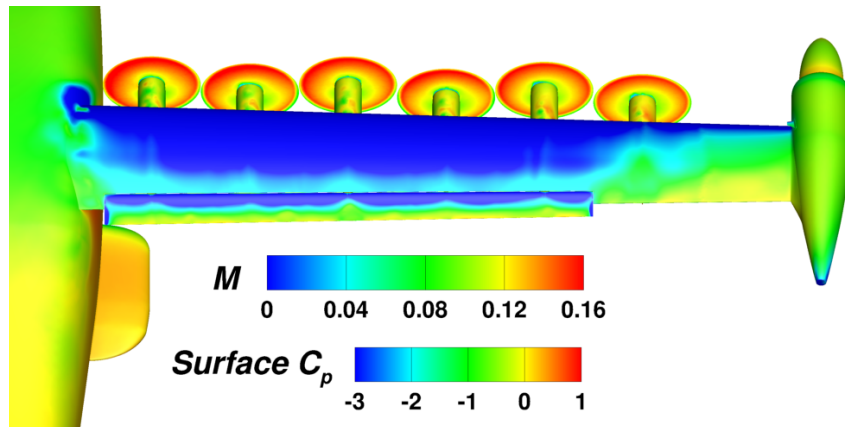
(b) High-Lift Propellers at 4702 RPM and 49.35 lbf

Figure 31. Effect of Different High-Lift Propeller Conditions on Pressure Coefficient. Landing Configuration at 58 KEAS, $\alpha = 10°$, No Aileron Deflection, High-Lift Blowing, Kestrel SA RC.
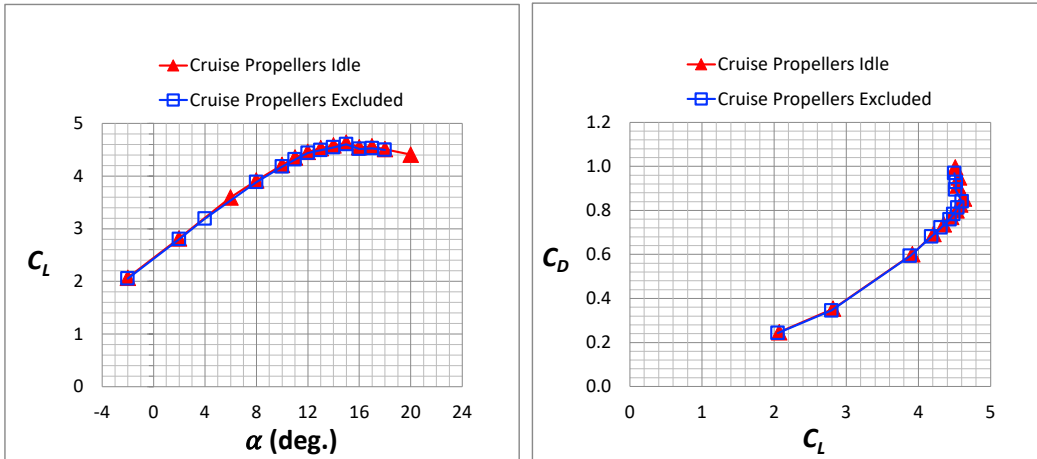
(a) Lift Coefficient versus Angle of Attack

(b) Drag Polar
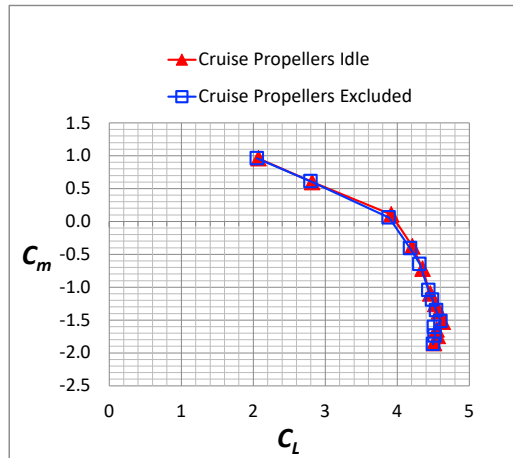
(c) Pitching Moment Coefficient versus Lift Coefficient

Figure 32. Effect of Excluding the Cruise Propellers in the Simulation. Landing Configuration at 58 KEAS, No Aileron Deflection, Kestrel SA RC. High-Lift Blowing Conditions at 5035 RPM, $T = 50.65$ lbf, and $Q = 16.23$ lbf-ft for the Cruise Propellers Idle Solutions and at 4702 RPM, $T = 49.3$ lbf, and $Q = 16$ lbf-ft for the Cruise Propellers Excluded Solutions.

(a) Lift Coefficient versus Angle of Attack

(b) Drag Polar

(c) Pitching Moment Coefficient versus Lift Coefficient

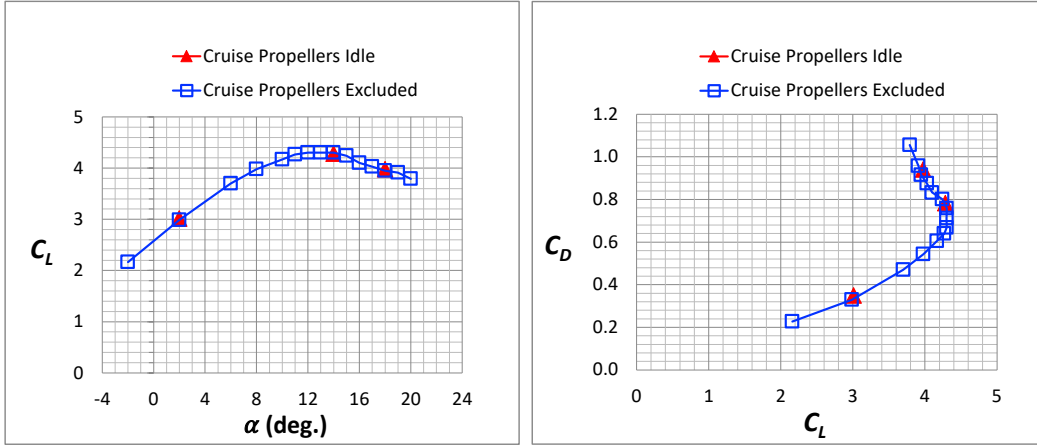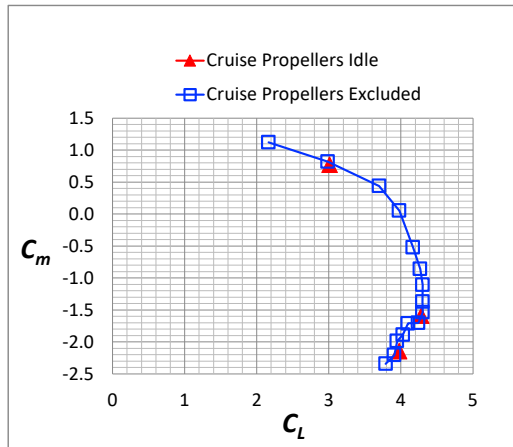Figure 33. Effect of Excluding the Cruise Propellers in the Simulation. Landing Configuration at 58 KEAS, No Aileron Deflection, USM3D SA QCR. High-Lift Blowing Conditions at 5035 RPM, $T = 50.65$ lbf, and $Q = 16.23$ lbf-ft.

3.4 Aerodynamic Performance with the DEP High-Lift System Operating and No Aileron Deflection
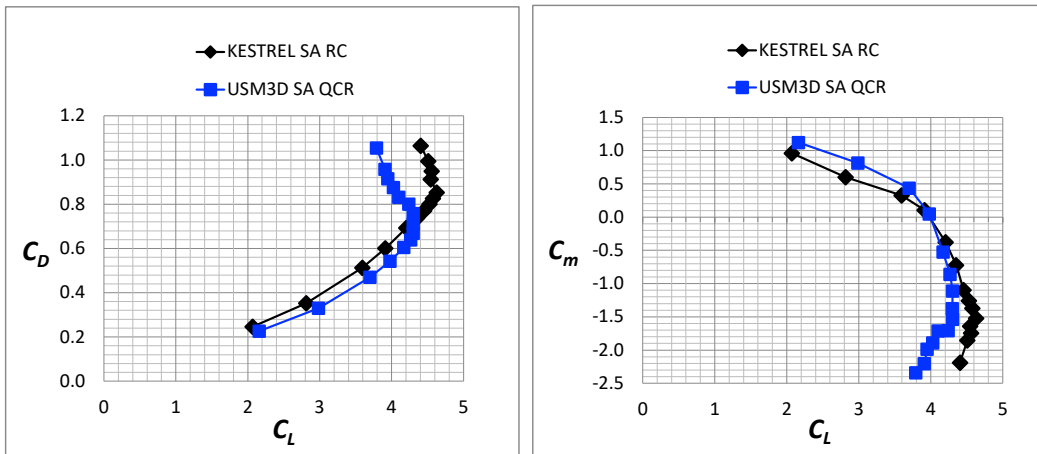
Figure 34 shows the comparison of aerodynamic coefficients between Kestrel and USM3D, the two CFD codes used at NASA LaRC, for the landing configuration with the DEP high-lift system operating. The lift coefficient compared well up through $\alpha = 12°$ (Figure 34(a)). The Kestrel code predicted an increasing lift coefficient up to $C_{L,max}$= 4.65 at $\alpha = 15°$, with a slight drop in lift at $\alpha = 16°$. The USM3D code predicted an increasing lift coefficient up to $C_{L,max}$= 4.5, with increasing angle of attack up through $\alpha = 12°$, then the lift remains constant through $\alpha = 14°$. The difference in lift coefficient at high angles of attack may result from the different SA turbulence model options that were used with Kestrel and USM3D. Accurately predicting high-lift performance is difficult with RANS approaches as flow separation increases with angle of attack. Using slightly different turbulence model variations may result in different flow separation regions that increase the difference in lift coefficient between the codes. The same option to the SA turbulence model was not available for both codes at the time of this work. Another less likely cause of the poor comparison of lift coefficient at high angles of attack might be a result of the difference in modeling the thrust distribution between the two codes. As mentioned in Section 2.7.1, a uniform jump actuator disk model resulted in a slightly smaller lift coefficient, compared to the triangular thrust distribution at $\alpha = 3.5°$ with the Kestrel code. If the difference in the actuator disk loading was the issue, then authors would have also expected a lower lift coefficient from USM3D across the angle-of-attack range, but the lift from USM3D was higher than Kestrel for $\alpha < 10$.

The Kestrel code predicted higher drag over the angle-of-attack range than the USM3D code (Figure 34(b)). The drag polar in Figure 34(c) shows that the USM3D codes predicted less drag for a given lift up to $C_L = 4.3$. However, the maximum lift coefficient predicted by USM3D was $C_L = 4.3$, whereas Kestrel predicted increasing lift up to $C_L = 4.65$, with drag increasing for both codes as angle-of-attack increases. Pitching moment coefficient was near zero for both codes near $C_L \approx 4$ (as lift was increasing, $\alpha = 8°$), and for $C_L < 3.8$ USM3D predicts a slightly larger positive pitching moment coefficient. As C_L was increased towards stall, USM3D predicts a slightly more negative pitching moment than Kestrel, $C_L > 4.0$ ($\alpha > 8°$) (Figure 24(d)).
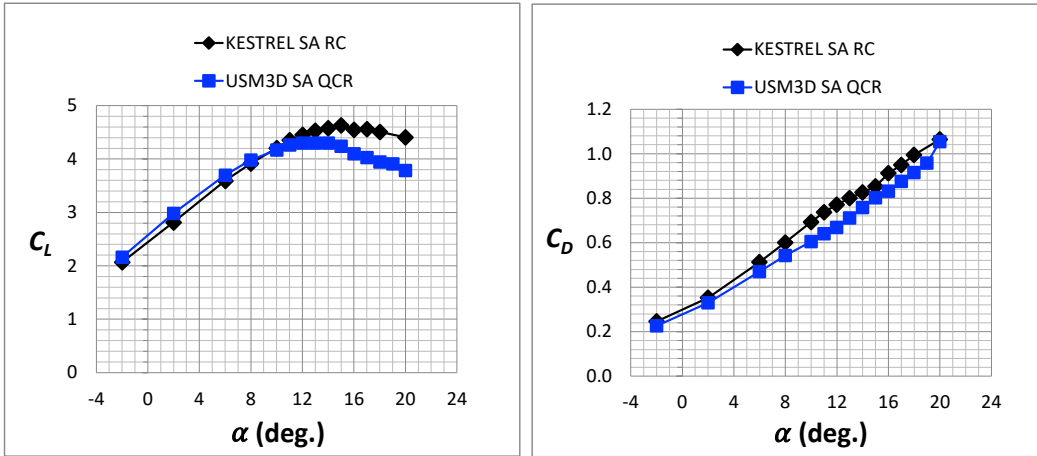
(a) Lift Coefficient versus Angle of Attack

(b) Drag Coefficient versus Angle of Attack

(c) Drag Polar

(d) Pitching Moment Coefficient versus Lift Coefficient

Figure 34. Two Code Comparison of Aerodynamic Performance. Landing Configuration at 58 KEAS with No Aileron Deflection. High-Lift Blowing at 5035 RPM, $T = 50.65$ lbf, $Q = 16.23$ lbf-ft, and $P_{out} = 11.6$ kW. Cruise Propellers Excluded from the USM3D Simulations and Idle in the Kestrel Simulations.

Further insight to the similarities and differences in lift coefficient between the two codes is gained in the comparison of pressure coefficient contours and streamlines in Figures 35–37 for $\alpha = 10°$, $\alpha = 14°$ and $\alpha = 16°$, respectively. In these figures, the conditions are slightly different, but as discussed in Section 3.3 the impacts on force and moment coefficients were negligible. The USM3D SA QCR solutions have the cruise propellers excluded and the high-lift blowing conditions at 5035 RPM, $T = 50.65$ lbf, $Q = 16.23$ lbf-ft, and $P_{out} = 11.6$ kW. The Kestrel solutions at these same conditions did not have the variables needed in the solution file to create streamlines and the code version is no longer available to extract new variables from the solution. Therefore, the Kestrel SA RC solutions in Figures 35–37 have high-lift blowing conditions at 4702 RPM, $T = 49.3$ lbf, $Q = 16$ lbf-ft, and $P_{out} = 10.7$ kW and the cruise propellers are included at idling conditions.

The lift coefficient compares well between the two codes at $\alpha = 10°$ and therefore, the solutions look similar, but with minor differences. The condensed streamlines on the inboard wing in the USM3D solution indicate a trail from a vortex (Figure 35(a)), that appears more at the wingroot in the Kestrel result (Figure 35(b)). Additionally, both solutions indicate some flow separation outboard near the wingtip that extends about 25% forward from the trailing edge. At $\alpha = 14°$, the lift coefficient is $C_L = 4.54$ and $C_L = 4.3$ from Kestsrel and USM3D, respectively. Therefore, it is not surprising to see differences in the streamlines from the two codes. The flow separation at the wingtip nacelle does not extend fully forward to the wing leading edge in the Kestrel solution (Figure 36(b)), as it does in the USM3D solution (Figure 36(a)). At $\alpha = 16°$, there is an even larger difference in lift coefficient between the two codes, with Kestrel at $C_L = 4.51$ and USM3D at $C_L = 4.1$. Figure 37 shows that both codes have similar flow separation regions near the wingroot and wingtip, but the USM3D solution has an additional region of separated flow downstream of the third high-lift nacelle from the centerline, that is not present in the Kestrel solution.

A noticeable difference in C_p between the two solutions occurs on the high-lift nacelles as a result of the different thrust and torque profiles used for each code. The uniform thrust and torque coefficient actuator boundary condition had a more uniform velocity profile across the propeller patch, whereas the triangular thrust and torque distribution had a maximum velocity out towards the tip at $r/R_{prop} = 0.9$. Therefore, the USM3D solutions had larger regions of $C_p = 1$ on the nacelles downstream of the propeller plane, due to higher velocity flow near the nacelle surface than the Kestrel solutions.
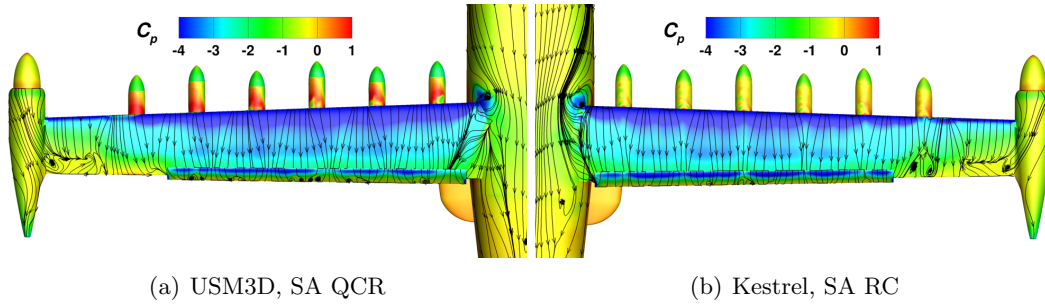
(a) USM3D, SA QCR　　　　　　　　(b) Kestrel, SA RC

Figure 35. Code Comparison of Pressure Coefficient and Streamlines at $\alpha = 10°$. Landing Configuration at 58 KEAS with No Aileron Deflection. USM3D SA QCR: High-Lift Blowing at 5035 RPM, $T = 50.65$ lbf, $Q = 16.23$ lbf-ft, $P_{out} = 11.6$ kW, and Cruise Propellers Excluded. Kestrel SA RC: High-Lift Blowing at 4702 RPM, $T = 49.3$ lbf, $Q = 16$ lbf-ft, $P_{out} = 10.7$ kW, and Idle Cruise Propellers.
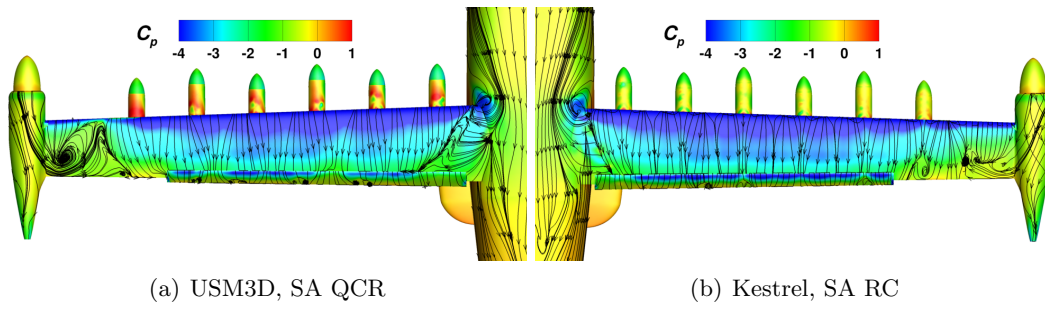

(a) USM3D, SA QCR　　　　　　　　(b) Kestrel, SA RC

Figure 36. Code Comparison of Pressure Coefficient and Streamlines at $\alpha = 14°$. Landing Configuration at 58 KEAS with No Aileron Deflection. USM3D SA QCR: High-Lift Blowing at 5035 RPM, $T = 50.65$ lbf, $Q = 16.23$ lbf-ft, $P_{out} = 11.6$ kW, and Cruise Propellers Excluded. Kestrel SA RC: High-Lift Blowing at 4702 RPM, $T = 49.3$ lbf, $Q = 16$ lbf-ft, $P_{out} = 10.7$ kW, and Idle Cruise Propellers.
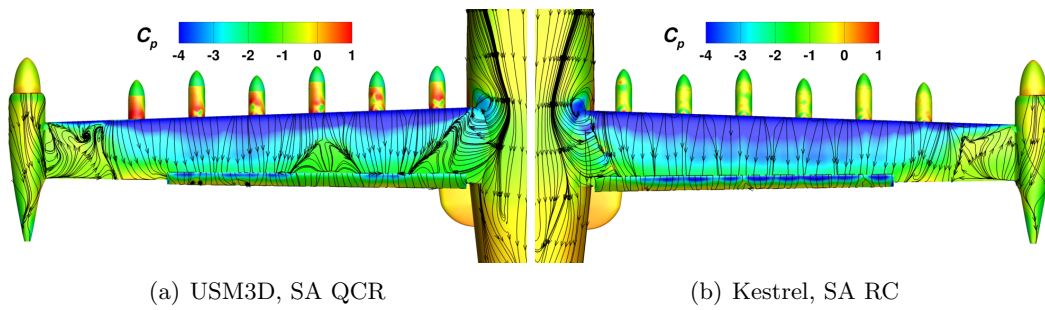

(a) USM3D, SA QCR　　　　　　　　(b) Kestrel, SA RC

Figure 37. Code Comparison of Pressure Coefficient and Streamlines at $\alpha = 16°$. Landing Configuration at 58 KEAS with No Aileron Deflection. USM3D SA QCR: High-Lift Blowing at 5035 RPM, $T = 50.65$ lbf, $Q = 16.23$ lbf-ft, $P_{out} = 11.6$ kW, and Cruise Propellers Excluded. Kestrel SA RC: High-Lift Blowing at 4702 RPM, $T = 49.3$ lbf, $Q = 16$ lbf-ft, $P_{out} = 10.7$ kW, and Idle Cruise Propellers.
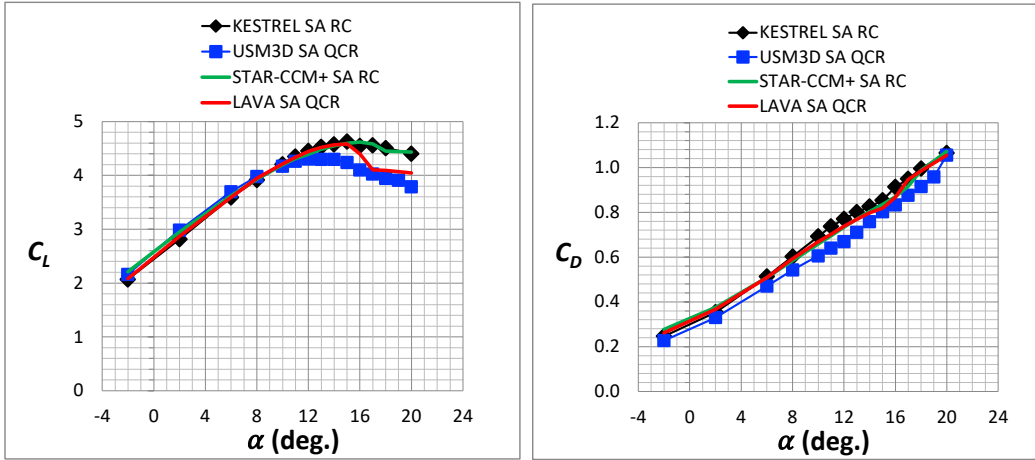
3.5 Four Code Comparison of Aerodynamic Performance with the DEP High-Lift System Operating and No Aileron Deflection

Figure 38 shows the comparison of the aerodynamic coefficients for the four codes used in the X-57 aerodynamic database for the landing configuration with the DEP high-lift system operating. The Kestrel, LAVA, and STAR-CCM+ results included the idling cruise propellers, but the cruise propellers were excluded in the USM3D simulations. As discussed in Section 3.3, excluding or modeling the idling propellers had a negligible impact on lift, drag, and pitching moment.

The four codes show good agreement for C_L and predicted a linear lift-curve slope for $-2° \leq \alpha \leq 8°$, Figure 38(a). The drag coefficient data from STAR-CCM+ and LAVA fall between the data from USM3D and Kestrel (Figure 38(b)). There was an excellent agreement between the two CFD codes using the SA RC turbulence model, Kestrel and STAR-CCM+. For these SA RC data, the lift curve (Figure 38(a)) and drag polar (Figure 38(c)) are nearly identical, and the pitching moment curves compare well except for two data where $C_L \leq 3$ (Figure 38(d)). Additionally, although not perfect agreement in $C_{L,max}$ for USM3D and LAVA, C_L also compared well between the two codes using SA QCR turbulence models for $\alpha > 16°$. These data suggest that turbulence models predicted different flow separation regions. However, without experimental data, the authors are unsure which solutions are the accurate assessment of the flow. The trend of pitching moment coefficient was somewhat similar for all codes, but with different codes comparing for $C_L \leq 3$, than at $C_L > 3$. These data represent the importance of using multiple codes and turbulence models to provide an uncertainty bound on the aerodynamic database prior to the first flight of the X-57 Maxwell airplane.

(a) Lift Coefficient versus Angle of Attack

(b) Drag Coefficient versus Angle of Attack
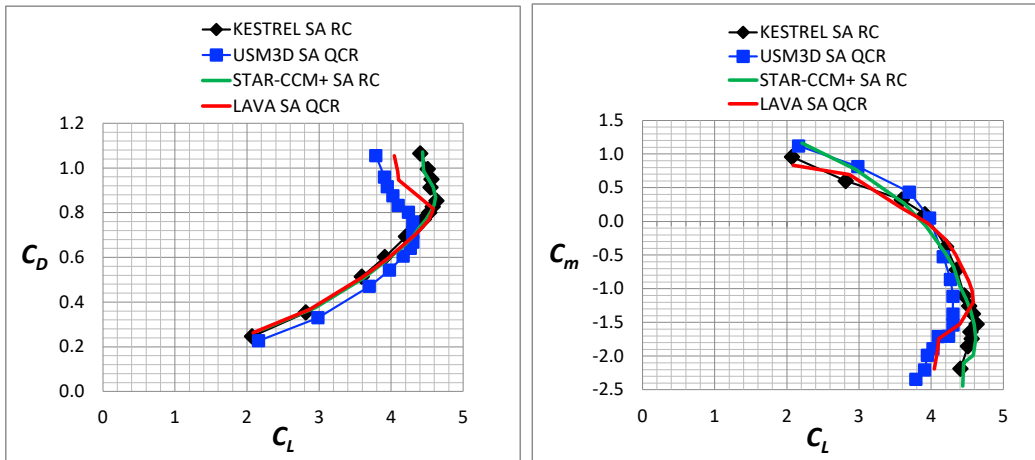
(c) Drag Polar

(d) Pitching Moment Coefficient versus Lift Coefficient

Figure 38. Four Code Comparison of Aerodynamic Performance. Landing Configuration at 58 KEAS with No Aileron Deflection. High-Lift Blowing at 5035 RPM, $T = 50.65$ lbf, $Q = 16.23$ lbf-ft, and $P_{out} = 11.6$ kW.

3.6 Aileron Effectiveness, Right Aileron Deflection, with the DEP High-Lift System Operating

The aileron effectiveness discussed in this section was the effect of the aileron deflection (δ_a) on rolling moment coefficient (C_l) for the landing configuration with the DEP high-lift propellers modeled with blowing conditions of $T = 50.65$ lbf, $Q = 16.23$ lbf-ft, at 5035 RPM; and the cruise propellers modeled with idle conditions at $T = $ -8.02 lbf, $Q = 0.65$ lbf-ft, at 1540 RPM. A positive δ_a was defined with the trailing edge deflected downward, and a negative δ_a with the trailing edge deflected upward. The comparison of C_l between Kestrel and USM3D for 58 KCAS at $\alpha = 2°$ and for $\alpha = 14°$ is shown in Figure 39. A top view of the skin friction coefficient (C_f) contours for $\alpha = 2°$ and $\alpha = 14°$ for each of the aileron deflection angles, are shown in Appendices A and B for Kestrel and USM3D, respectively.

The Kestrel and USM3D data are in excellent agreement for $\alpha = 2°$ as shown in Figure 39(a). The comparison of C_f contours between Kestrel and USM3D are shown in Figures 40 to 43 for $\delta_a = -15°$ to $\delta_a = 18°$. The flow contours are mostly similar, but some differences are evident. For example, the contours have a slightly different coloring in the blown-wing area with Kestrel solution having lower C_f values directly downstream of each nacelle than the USM3D solution. This difference in the upper surface of the blown-wing may be from the difference in thrust distribution that the two codes are using for the actuator disk; Kestrel with a triangular thrust distribution and USM3D with a uniform loading approach. However, since the differences are not asymmetric, there was no impact on C_l. Additionally, the Kestrel solutions have a flow separation region downstream of the most outboard high-lift nacelles for $\delta_a = -15°$ and $\delta_a = -10°$ that was not present in the USM3D solution.

Both codes indicate a better aileron effectiveness for negative aileron deflections (Figure 39(a)), indicated by the steeper slope for $\delta_a < 0°$, than for $\delta_a > 0°$. Looking at specific data, the rolling moment coefficient for Kestrel was $C_l = 0.0285$ for $\delta_a = -10°$, but it was only $C_l = $ -0.0193 for $\delta_a = 10°$. The C_f contours are mostly the same for the whole airplane upper surface, except the aileron regions; see the Kestrel solutions in Figure 41(a) for $\delta_a = -10°$ and Figure 42(a) for $\delta_a = 10°$. Figure 44 shows this same Kestrel data, but for smaller scale of C_f and a zoomed in view of the left and right ailerons for $\delta_a = -10°$ and $\delta_a = 10°$ at $\alpha = 2°$. The flow contours are similar on the neutral, left aileron. However, the right aileron for $\delta_a = 10°$ (Figure 44(b)) has mostly separated flow (dark blue contours) on the aileron that was deflected trailing edge down, which made it less effective than $\delta_a = -10°$. The more effective aileron deflection of $\delta_a = -10°$ (Figure 44(a)) also has flow separation on the outboard half of the aileron, but does have attached flow in the wake of the outboard-most high lift nacelle, albeit with a small separation zone directly downstream of the nacelle.
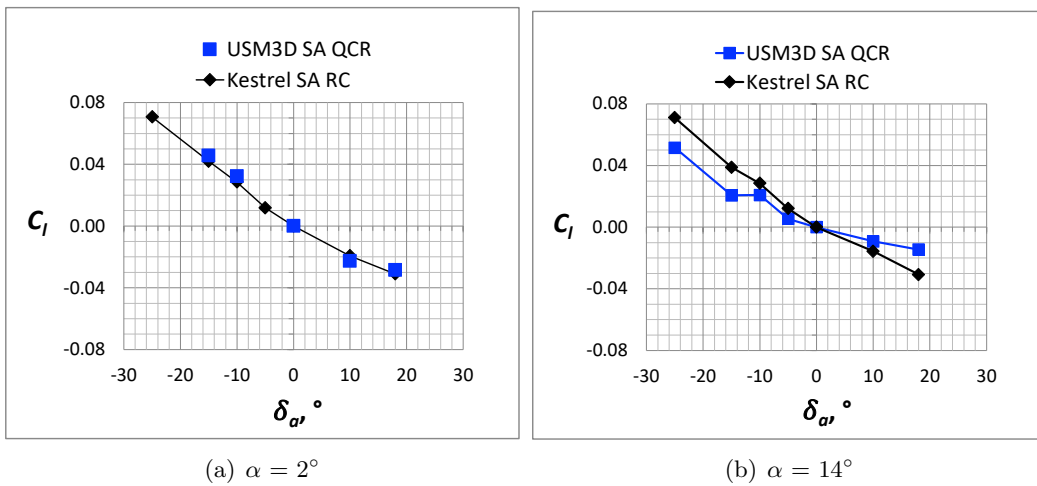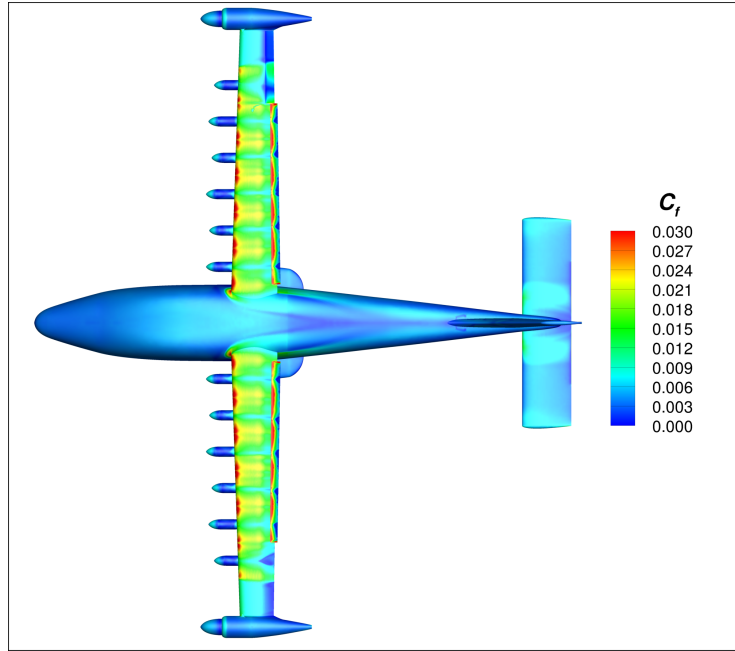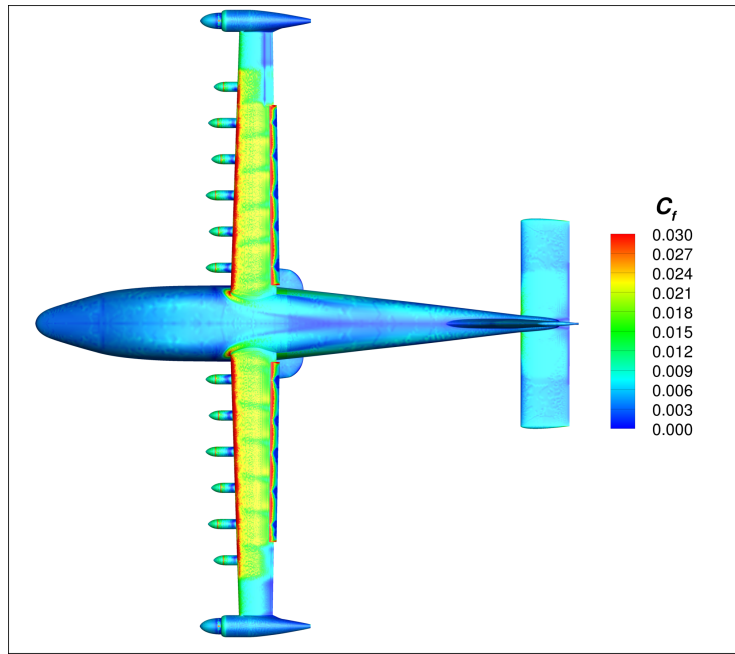
(a) $\alpha = 2°$

(b) $\alpha = 14°$

Figure 39. Kestrel and USM3D Code Comparisons of Aileron Effectiveness. Landing Configuration at 58 KEAS. High-Lift Blowing at 5035 RPM, $T = 50.65$ lbf, $Q = 16.23$ lbf-ft, and $P_{out} = 11.6$ kW. Cruise Propellers at 1540 RPM, $T = -8.02$ lbf, and $Q = 0.65$ lbf-ft.
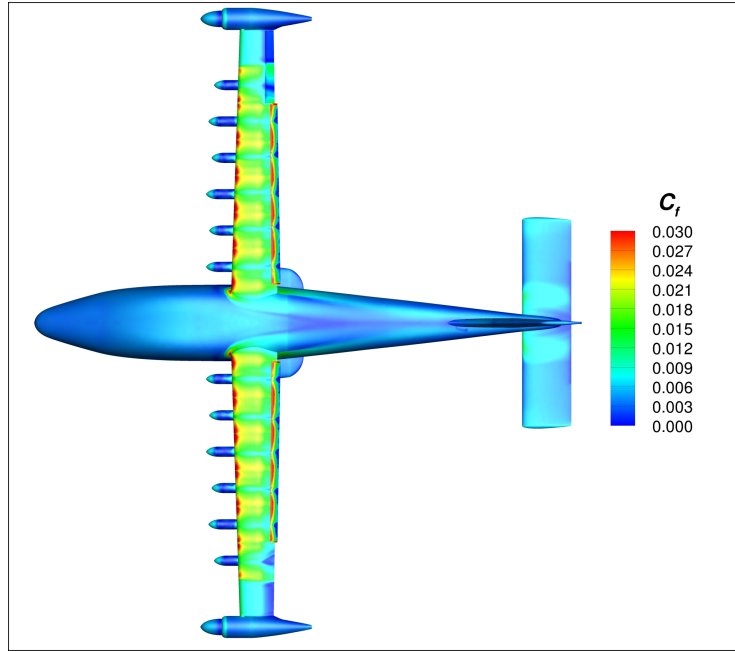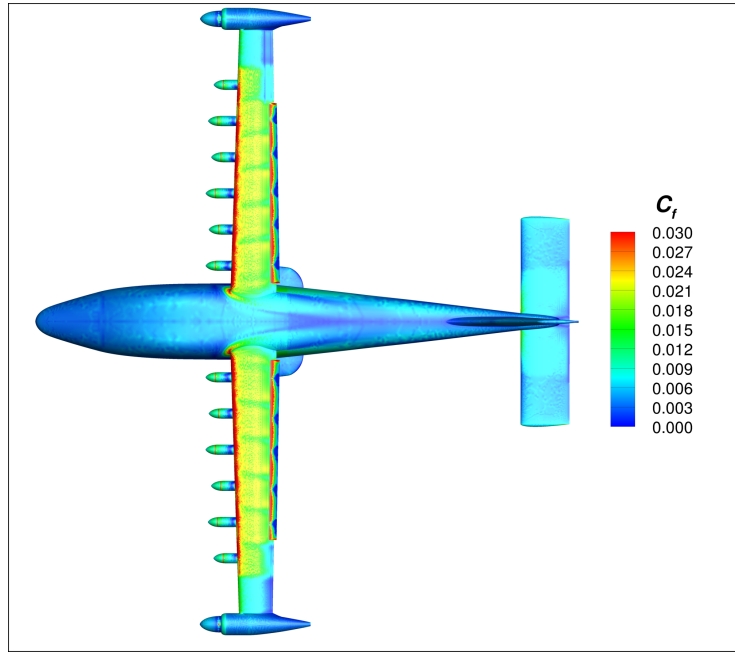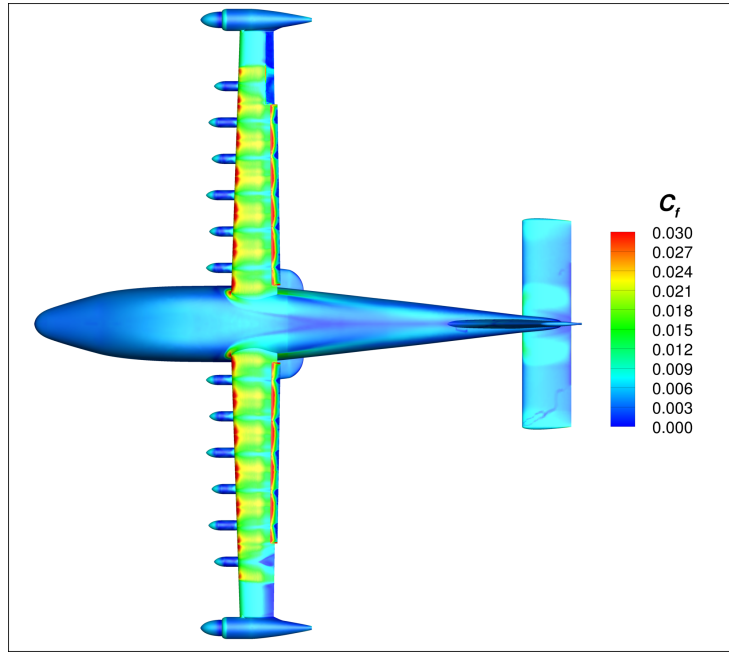
(a) Kestrel SA RC

(b) USM3D SA QCR

Figure 40. Comparison of Skin Friction Coefficient Contours for $\delta_a = -15°$ at $\alpha = 2°$. Landing Configuration at 58 KEAS. High-Lift Blowing at 5035 RPM, $T = 50.65$ lbf, and $Q = 16.23$ lbf-ft. Cruise Propellers at 1540 RPM, $T = -8.02$ lbf, and $Q = 0.65$ lbf-ft.
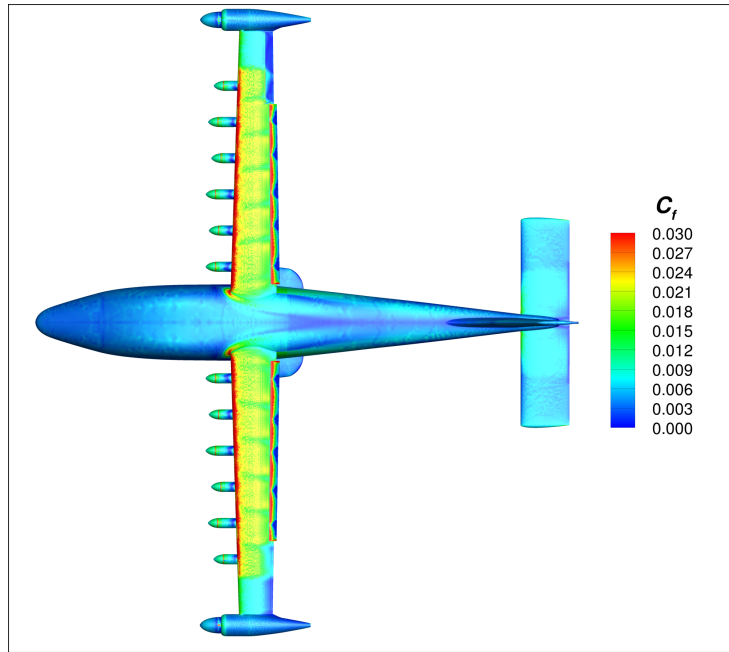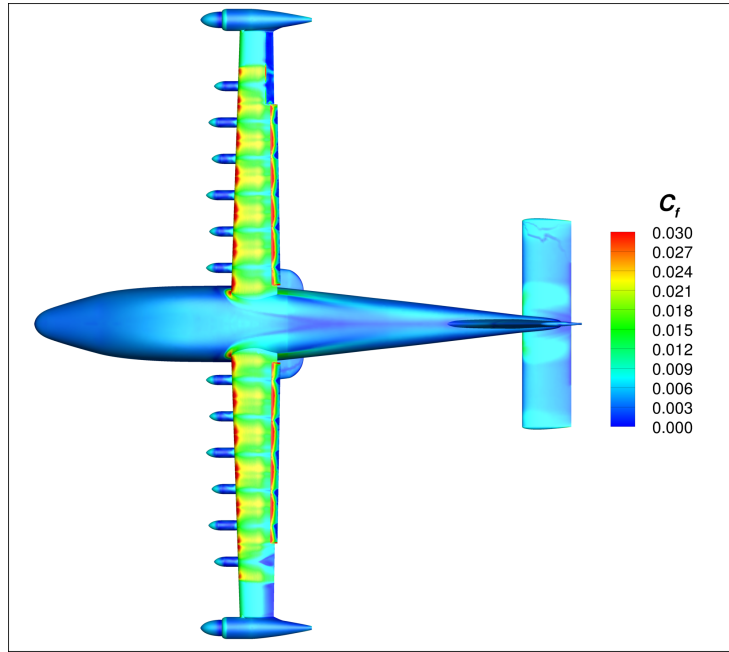
(a) Kestrel SA RC

(b) USM3D SA QCR

Figure 41. Comparison of Skin Friction Coefficient Contours for $\delta_a = -10°$ at $\alpha = 2°$. Landing Configuration at 58 KEAS. High-Lift Blowing at 5035 RPM, $T = 50.65$ lbf, and $Q = 16.23$ lbf-ft. Cruise Propellers at 1540 RPM, $T = $ -8.02 lbf, and $Q = 0.65$ lbf-ft.
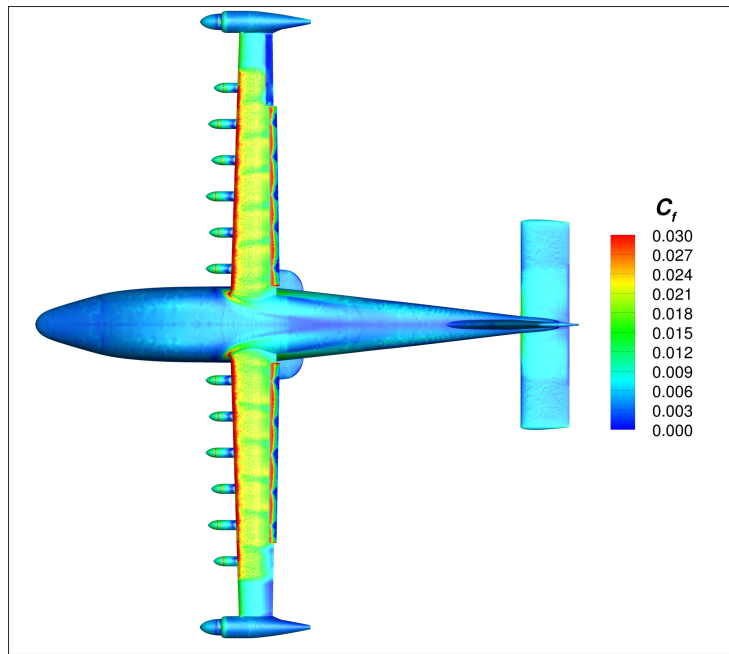
(a) Kestrel SA RC

(b) USM3D SA QCR

Figure 42. Comparison of Skin Friction Coefficient Contours for $\delta_a = 10°$ at $\alpha = 2°$. Landing Configuration at 58 KEAS. High-Lift Blowing at 5035 RPM, $T = 50.65$ lbf, and $Q = 16.23$ lbf-ft. Cruise Propellers at 1540 RPM, $T = -8.02$ lbf, and $Q = 0.65$ lbf-ft.
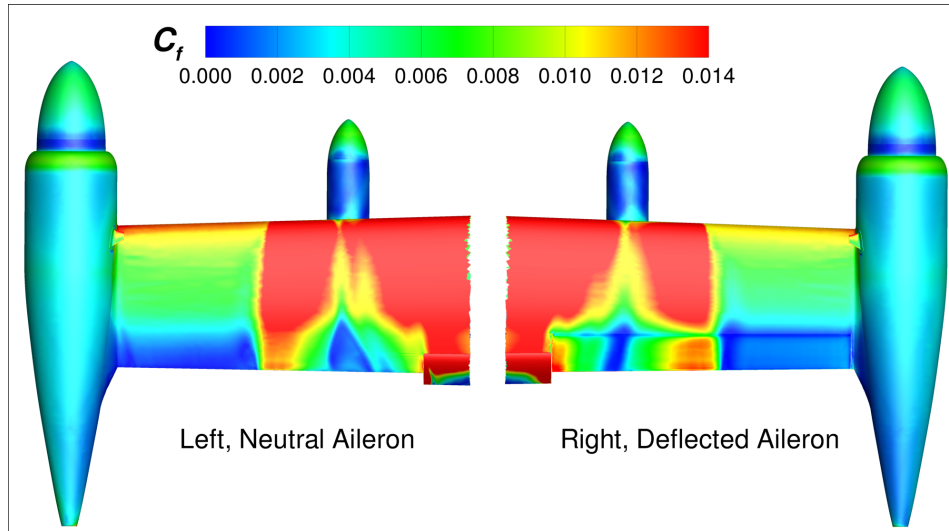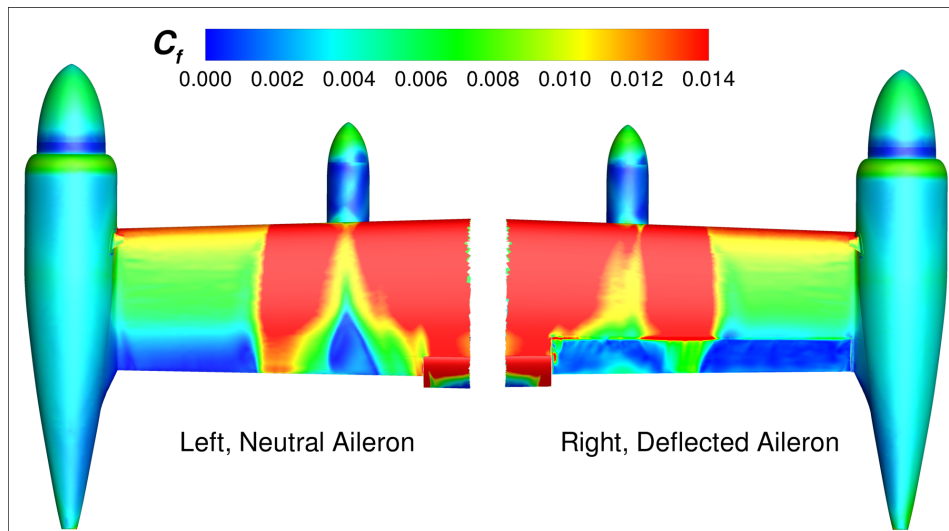
(a) Kestrel SA RC

(b) USM3D SA QCR

Figure 43. Comparison of Skin Friction Coefficient Contours for $\delta_a = 18°$ at $\alpha = 2°$. Landing Configuration at 58 KEAS. High-Lift Blowing at 5035 RPM, $T = 50.65$ lbf, and $Q = 16.23$ lbf-ft. Cruise Propellers at 1540 RPM, $T = $ -8.02 lbf, and $Q = 0.65$ lbf-ft.

67

(a) $\delta_a = -10°$

(b) $\delta_a = 10°$

Figure 44. Skin Friction Coefficient from Kestrel data in the Aileron Regions for $\alpha = 2°$. Landing Configuration at 58 KEAS. High-Lift Blowing at 5035 RPM, $T = 50.65$ lbf, and $Q = 16.23$ lbf-ft. Cruise Propellers at 1540 RPM, $T = $ -8.02 lbf, and $Q = 0.65$ lbf-ft.

In general, the USM3D code predicted less aileron effectiveness over the range of aileron deflection for $\alpha = 14°$ than Kestrel (Figure 39(b)), but the codes were in relatively good agreement for $\delta_a = -10°$, $\delta_a = -5°$ and $\delta_a = 10°$ for an $\alpha = 14°$. Both codes indicated a better aileron effectiveness for negative aileron deflections, than for positive deflections. For example, the rolling moment coefficient for Kestrel was $C_l = 0.0285$ for $\delta_a = -10°$, but only $C_l = -0.0157$ for $\delta_a = 10°$. Similarly for USM3D, $C_l = 0.0208$ for $\delta_a = -10°$, but only $C_l = -0.0093$ for $\delta_a = 10°$.

At $\delta_a = -25°$, $\delta_a = -15°$ and $\delta_a = 18°$, the USM3D data indicate much less aileron effectiveness than the Kestrel data. Figures 45–46 show the comparison of C_f and C_p contours in the aileron regions for $\delta_a = -25°$ at $\alpha = 14°$. For the USM3D solution (Figure 45(a)), the flow separation appears to extend to the wing leading edge for the outboard half of both ailerons. There was flow separation upstream of the ailerons in the Kestrel solution, but the separation does not extend forward to the leading edge as it does in the USM3D solutions. Additionally, the inboard section of the right aileron has higher skin friction values (Figure 45) and slightly higher pressure (red contours in Figure 46(b)) in the Kestrel solution, than in the USM3D solution (white contours in Figure 46(a)). Therefore, Kestrel predicted a more effective aileron than USM3D for $\delta_a = -25°$ at $\alpha = 14°$.

The effect of angle of attack on rolling moment is shown in Figure 47(a) for Kestrel data and in Figure 47(b) for USM3D data. The Kestrel code predicted that the aileron effectiveness was independent of angle of attack, at least between $\alpha = 2°$ and $\alpha = 14°$. Both $\alpha = 2°$ and $\alpha = 14°$ were prestall conditions, according to the Kestrel data in Figure 34(a). The aileron effectiveness may be diminished at post stall conditions if the outboard flow separation moves forward to the leading edge as it did for Kestrel data at $\alpha = 16°$ with no aileron deflection (Figure 37(b)). The USM3D code predicted the aileron was more effective at $\alpha = 2°$, and less effective at $\alpha = 14°$. According to the USM3D data in Figure 34(a), $\alpha = 2°$ was prestall, while $\alpha = 14°$ was post stall.

Figure 48 shows the four code comparison of aileron effectiveness for $\alpha = 2°$ and $\alpha = 14°$. In general, the codes compare well for $\alpha = 2°$ (Figure 48(a)). The Star-CCM+ exhibits better rolling moment effectiveness, or higher rolling moment coefficients, than the other codes for $\delta_a < 0°$, but matches USM3D and Kestrel data well for $\delta_a > 0°$. The LAVA code predicts better rolling moment effectiveness for $\delta_a > 0°$, than the other codes. In general, the codes compare well for $\alpha = 14°$ (Figure 48(b)), except USM3D has a lower C_l for $\delta_a < -10°$.

Finally, Figure 49 shows a comparison of Kestrel pressure coefficient contours on the right aileron for $\delta_a = 18°$, $\delta_a = 0°$, and $\delta_a = -25°$ at $\alpha = 14°$. For the positive aileron deflection (trailing edge down), there was suction with $C_p < 0$ on and ahead of the aileron (Figure 49(a)), which acts to increase lift and generates a negative rolling moment ($C_l = -0.0308$). The pressure coefficient on the aileron was mostly $C_p = 0$ for the neutral aileron and $C_l = 0$ for the symmetric configuration with neutral ailerons. For a negative aileron deflection (trailing edge up), there was positive pressure coefficient on the aileron and a noticeable reduction in suction on the wing ahead of the aileron (Figure 49(c)), which decreased lift and generated a positive rolling moment ($C_l = 0.0711$).
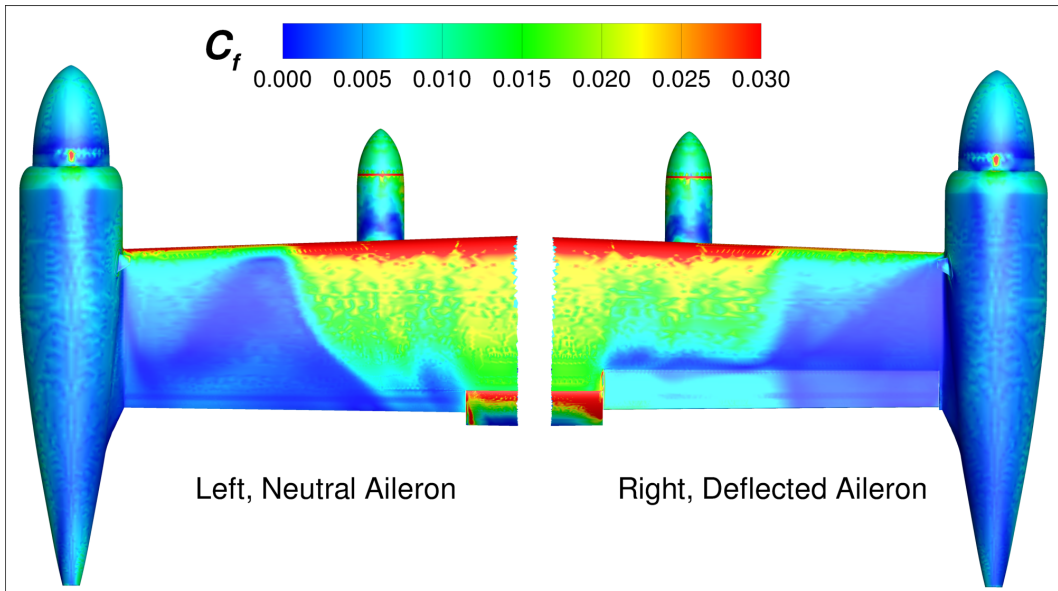
(a) USM3D SA QCR
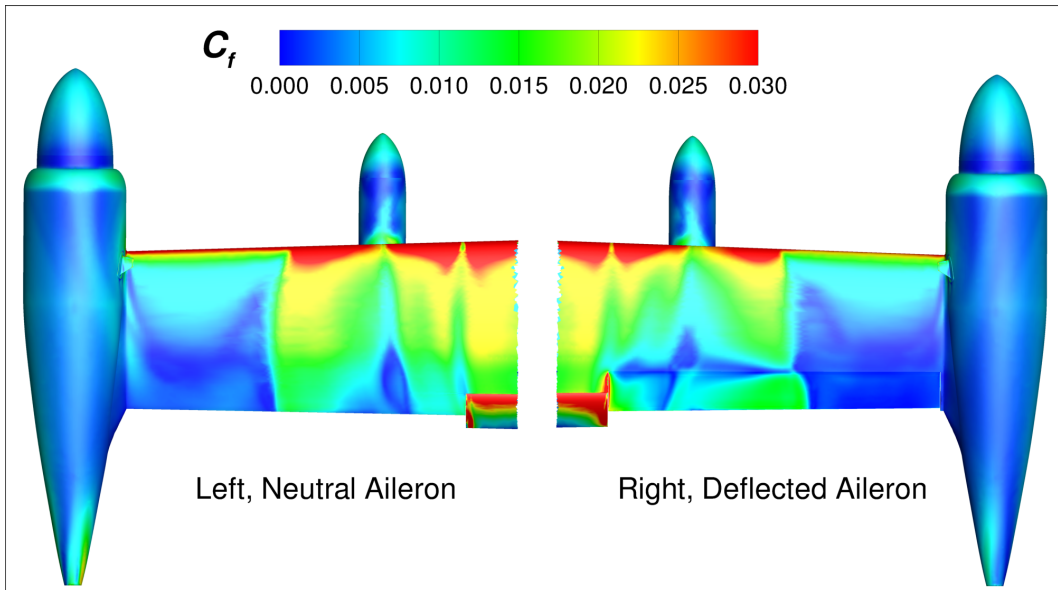
(b) Kestrel SA RC

Figure 45. Comparison of Skin Friction Coefficient between Kestrel and USM3D data in the Aileron Regions for $\delta_a = -25°$ at $\alpha = 14°$. Landing Configuration at 58 KEAS. High-Lift Blowing at 5035 RPM, $T = 50.65$ lbf, and $Q = 16.23$ lbf-ft. Cruise Propellers at 1540 RPM, $T = $ -8.02 lbf, and $Q = 0.65$ lbf-ft.
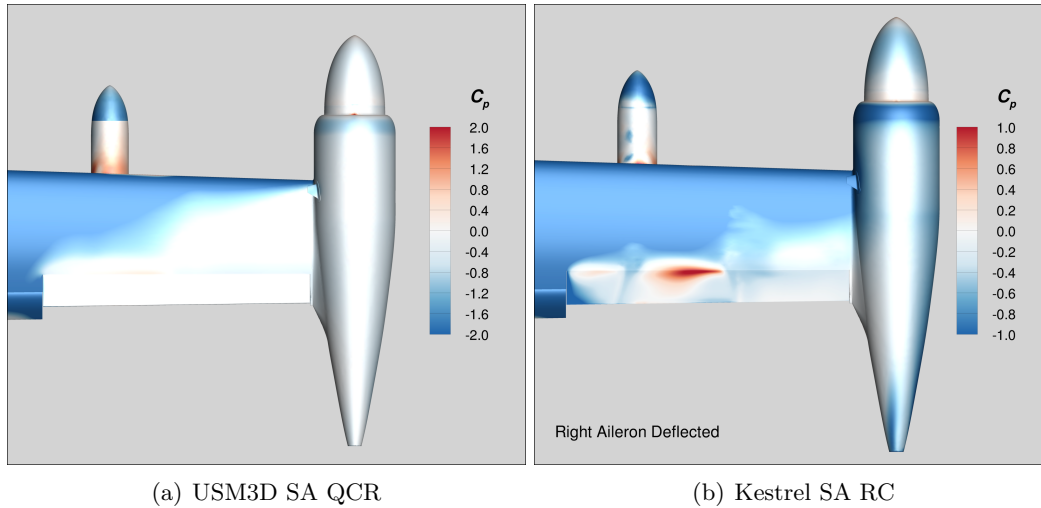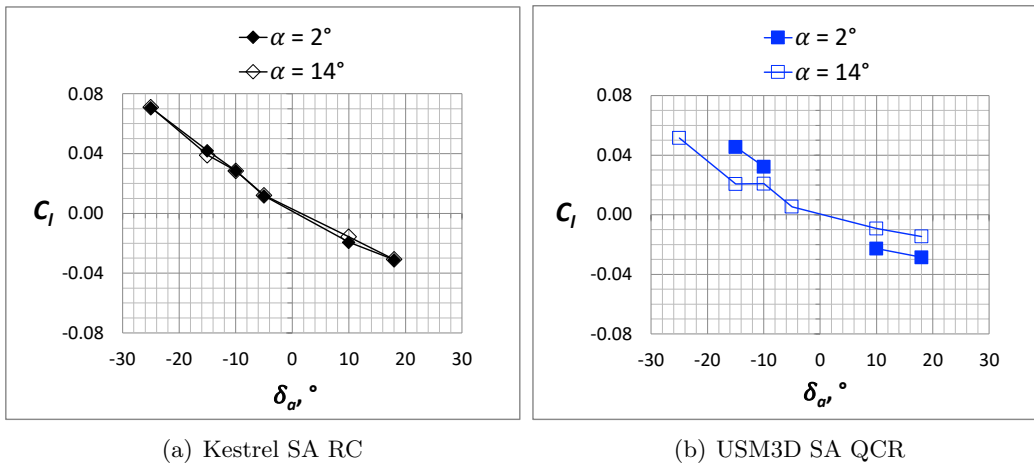
(a) USM3D SA QCR   (b) Kestrel SA RC

Figure 46. Comparison of Pressure Coefficient between Kestrel and USM3D data, the Right Deflected Aileron for $\delta_a = -25°$ at $\alpha = 14°$. Landing Configuration at 58 KEAS. High-Lift Blowing at 5035 RPM, $T = 50.65$ lbf, and $Q = 16.23$ lbf-ft. Cruise Propellers at 1540 RPM, $T = $ -8.02 lbf, and $Q = 0.65$ lbf-ft.

(a) Kestrel SA RC   (b) USM3D SA QCR

Figure 47. Effect of Angle of Attack on Aileron Effectiveness. Landing Configuration at 58 KEAS. High-Lift Blowing at 5035 RPM, $T = 50.65$ lbf, and $Q = 16.23$ lbf-ft. Cruise Propellers at 1540 RPM, $T = $ -8.02 lbf, and $Q = 0.65$ lbf-ft.

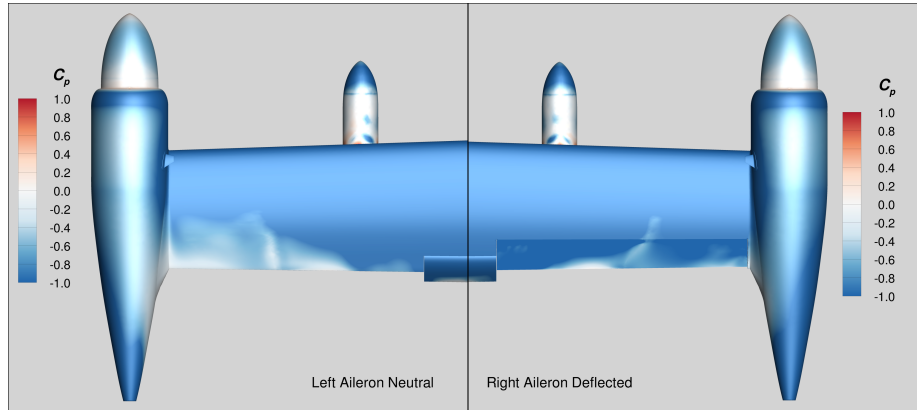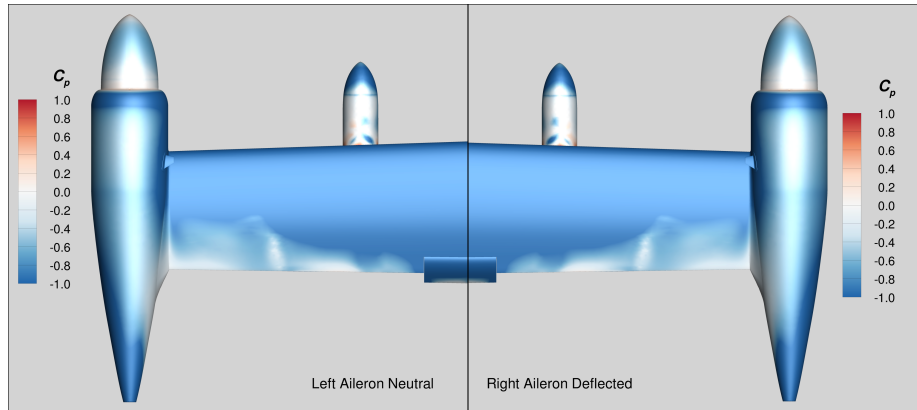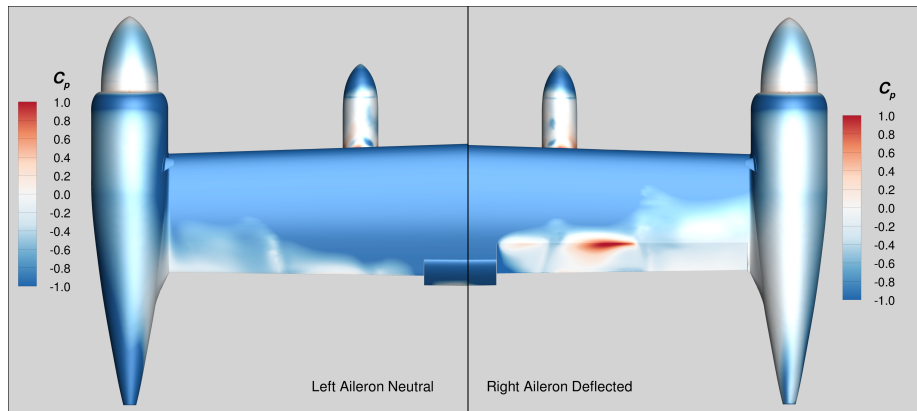(a) $\alpha = 2°$ (b) $\alpha = 14°$
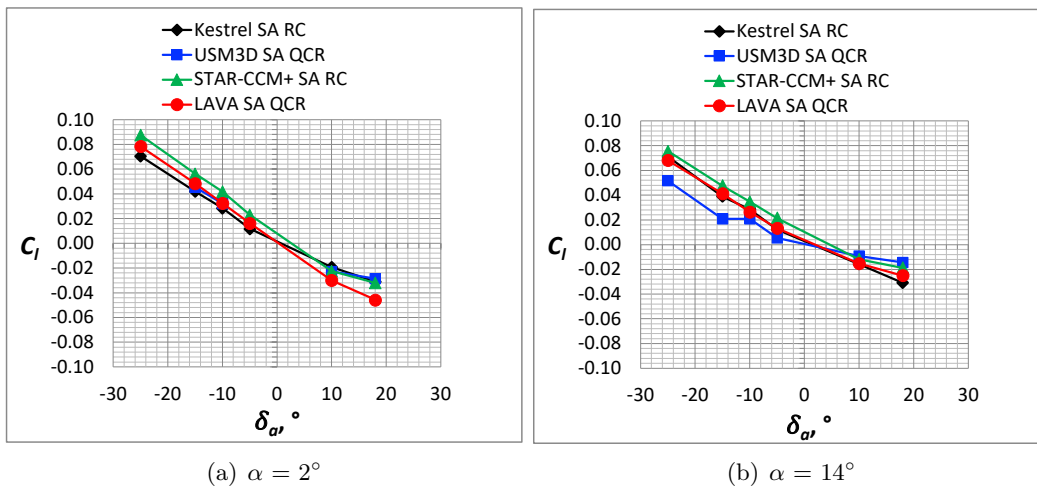
Figure 48.   Four Code Comparison of Rolling Moment as a function of Aileron Deflection. Landing Configuration at 58 KEAS. High-Lift Blowing at 5035 RPM, $T = 50.65$ lbf, and $Q = 16.23$ lbf-ft. Cruise Propellers at 1540 RPM, $T = $ -8.02 lbf, and $Q = 0.65$ lbf-ft.

(a) $\delta_a = 18°$

(b) $\delta_a = 0°$

(c) $\delta_a = -25°$

Figure 49. Comparison of Pressure Coefficient on the Right Deflected Aileron for $\delta_a = -25°$ and $\delta_a = 18°$ at $\alpha = 14°$, Kestrel SA RC. Landing Configuration at 58 KEAS. High-Lift Blowing at 5035 RPM, $T = 50.65$ lbf, and $Q = 16.23$ lbf-ft. Cruise Propellers at 1540 RPM, $T = $ -8.02 lbf, and $Q = 0.65$ lbf-ft.

3.7 Effect of Aileron Deflection on Aerodynamic Performance, With DEP High-Lift System Operating and Idle Cruise Propellers

Figures 50 and 51 show the code comparisons between Kestrel and USM3D for the aerodynamic coefficients as a function of aileron deflection at $\alpha = 2°$ and $\alpha = 14°$, respectively. It is clear that the primary effects of aileron deflection are on rolling moment and drag, with a slight impact on lift and pitching moment, and minimal influence on side force and yawing moment. The corresponding skin friction contours at $\alpha = 2°$ and $\alpha = 14°$ are shown in Appendix A (Figures 59–72) for Kestrel solutions, and are shown in Appendix B (Figures 73–82) for USM3D solutions.

The effects of aileron deflection on rolling moment were discussed in the previous section, and therefore, not revisited here. The drag change with aileron deflection is shown in Figures 50(b) and 51(b), and there is almost a constant difference in drag between the Kestrel and USM3D results for each of the angles of attack, 2° and 14°. The difference in drag may be attributed to the different modification (RC vs QCR) to the standard SA turbulence model that was available for each code. The Kestrel results will be discussed to help explain the change in drag with aileron deflection. The effect on drag with positive aileron deflection (down) is an increase in drag for both $\alpha = 2°$ and $\alpha = 14°$. For $\alpha = 2°$, the drag increases $\Delta C_D = 0.0141$, which is a 4.0% increase in configuration drag for the right aileron deflected down $\delta_a = 18°$. For $\alpha = 14°$, the drag increases $\Delta C_D = 0.0274$, which is an increase of 3.3% in the configuration drag for $\delta_a = 18°$. For negative aileron deflections, the trend in drag change from the undeflected case is different between $\alpha = 2°$ and $\alpha = 14°$. At $\alpha = 2°$, for aileron deflections of $\delta_a = -5°$ and $\delta_a = -10°$ the drag decreases slightly, $\Delta C_D = -0.0038$, compared to the undeflected case. At $\alpha = 2°$ and $\delta_a = -25°$, the drag increases from the minimum drag with an increase of $\Delta C_D = 0.0086$. However, for the $\alpha = 14°$ case, the drag generally decreases with decreasing aileron deflection (up deflection) to a minimum drag at $\delta_a = -25°$, with a $\Delta C_D = -0.0083$ compared to the undeflected case.

To help understand why the drag trends are different for $\alpha = 2°$ and $\alpha = 14°$ at negative aileron deflections, we can examine some aspects of the complicated flow field around the aileron. Note that the inboard section of the aileron is immersed in the high velocity flow of the outboard high-lift propeller, as illustrated in Figure 52 with Mach contours at two axial stations (aileron is shaded light gray). There is an additional complexity with the aileron deflection controlling the lift locally at the wingtip, and it appears to influence the effects of the wingtip vortex on the wingtip nacelle (discussed below).

First, examine the skin friction coefficient contours on the upper and lower surfaces around the deflected aileron for $\alpha = 2°$ in Figures 59–65. At aileron deflections of $\delta_a = 10°$ (Figure 64(a)) and $\delta_a = 18°$ (Figure 65(a)), the flow separates from the aileron upper surface on the inboard section (in the wake of the high-lift propeller flow). Flow separation in the inboard region also occurs on the aileron lower surface for a deflection of $\delta_a = -25°$ (Figure 59(b)). This flow separation contributes to the drag at both high positive and high negative aileron deflections. There are very low skin friction values on the outboard, unblown section of the aileron on both surfaces for all aileron deflections. Next, examine the skin friction

coefficient contours on the upper and lower surfaces around the deflected aileron for $\alpha = 14°$ in Figures 66–72. Again, the flow separates from the upper surface of the inboard portion of the aileron at both $\delta_a = 10°$ (Figure 71(a)) and $\delta_a = 18°$ (Figure 72(a)), and is attached for all other aileron deflections. On the inboard section of the aileron lower surface, the flow is attached for all aileron deflections except at $\delta_a = -25°$, where there is a partial span section with separated flow that is centered around the outboard high-lift nacelle (Figure 66(b)).

Figure 53 is a plot of pressure distributions at y = 171.728 inches, which is about midspan of the aileron section outboard of the high-lift propeller flow (see Figure 52). For $\alpha = 14°$ (Figure 53(b)), the pressure distributions for the lower surface at the negative aileron deflections show a spike in minimum pressure for 166 inches < x < 168 inches, which indicates strong flow acceleration around the corner of the aileron hinge, and the pressure recovers continuously to the trailing-edge at x = 172 inches. The flow is attached on the lower surface even for the $\delta_a = -25°$ case, which is the maximum up aileron deflection. Now examine the pressure distributions for the $\alpha = 2°$ solutions (Figure 53(a)). For $\delta_a = -25°$, after the strong acceleration around the hinge line, there is a brief pressure recovery (167 inches < x < 168 inches), an apparent constant pressure region (168 inches < x < 170 inches) indicating some flow separation, and then a slight pressure recovery in the last few percent (2 inches) of the aileron. The pressure recovery trend is very different between $\delta_a = -25°$ and the other negative aileron deflections. These data show that for an aileron deflection of $\delta_a = -25°$, there is no flow separation at $\alpha = 14°$, but there is lower surface flow separation at $\alpha = 2°$. At $\alpha = 2°$, this flow separation from the lower surface of the aileron contributes to the drag increase for $\delta_a = -25°$ that we do not see at the other negative aileron deflections (Figure 50(b)).

As briefly mentioned above, another aspect that contributes to the change in drag with aileron deflection is the influence the aileron has on the wingtip vortex at $\alpha = 14°$. Figures 54–55 ($\alpha = 2°$) and Figures 56–57 ($\alpha = 14°$) show the pressure coefficient distribution on the aft end of the cruise nacelles on the left wingtip (undeflected aileron) compared to the right wingtip (deflected aileron). Comparing Figures 56 and 57 show the effect of the right aileron deflection on C_p distributions for $\alpha = 14°$. Note that there was increased suction on the aft portion of the cruise nacelle on the right side with the aileron deflected down $\delta_a = 18°$ (Figure 57(b)), as compared to the aileron deflected up $\delta_a = -25°$ (Figure 56(b)), contributing to increased drag. Figure 56 shows the comparison of nacelle aft pressure distributions between the left undeflected aileron and the right aileron deflected up at $\delta_a = -25°$. The up deflected aileron unloads the lift at the tip, reduces the wingtip vortex, and increases the pressure recovery on the aft portion of the cruise nacelle Figure 56(b), as compared to the undeflected aileron in Figure 56(a). The increased pressure recovery contributed to the reduction in drag for the negative aileron deflections at $\alpha = 14°$. The effect of aileron changes on the wingtip nacelles is significantly reduced at $\alpha = 2°$. Figures 54–55 have the same comparisons at $\alpha = 2°$. For the $\delta_a = 18°$ aileron down case (Figure 55), there is only a small increase in suction very near the trailing-edge of the cruise nacelle. For the $\delta_a = -25°$ aileron up case (Figure 54), there is no discernible difference in the cruise nacelle pressure distribution from the undeflected case, and there is only a change in the pressures on the aft-facing

disk of the geometry that represents the core of the cooling flow leaving the cruise nacelle.

Another interesting flow feature was uncovered when investigating the flow over the aileron at $\alpha = 14°$. Figure 58 shows the flow field Mach distribution at a longitudinal cut of x = 166 inches. A secondary vortex is generated outside of the outboard high-lift propeller flow. This secondary vortex entrains the high velocity propeller flow and pulls some of the high velocity flow outboard onto the aileron, increasing the aileron coverage with high velocity flow. However, outboard of the vortex core, low velocity air is pulled away from the surface and pulled inboard. This effect can be seen on a C_p contour Figures 66-72, where just outboard of the high velocity flow from the outboard high-lift propeller, there is a region at about midspan of the aileron where the separation moves significantly forward on the upper surface of the wing.

The changes in lift coefficient with aileron deflection increased approximately $\Delta C_L = 0.3$ at $\alpha = 2°$ and $\Delta C_L = 0.1$–0.2 for $\alpha = 14°$ as the aileron deflection was increased through the range of $\delta_a = -25°$ to $\delta_a = 18°$ (Figures 50(a) and 51(a)). Figure 49 for $\alpha = 14°$ can be used to explain the slight differences in lift with aileron deflection. At $\delta_a = -25°$ (Figure 49(c)), the aileron trailing edge is deflected upward, which pressurized the aileron and a portion of the wing upstream of the aileron (red contours) and resulted in less lift than an undeflected aileron (Figure 49(b)). The lift increased slightly as the aileron deflection increased because of reduced pressure upstream of the aileron. As the δ_a continued to increase with the trailing edge deflected down beyond the undeflected position, the flow accelerated and pressure dropped even further (Figure 49(a)) for a maximum lift at the maximum δ_a.
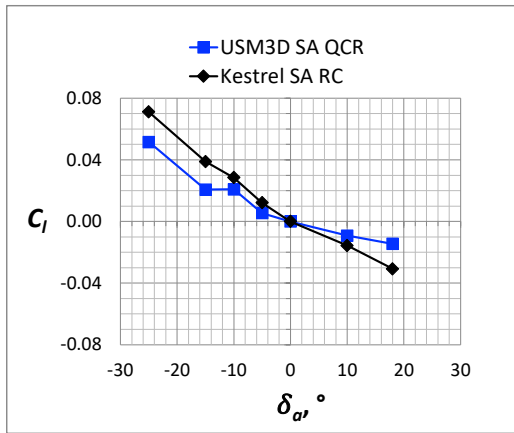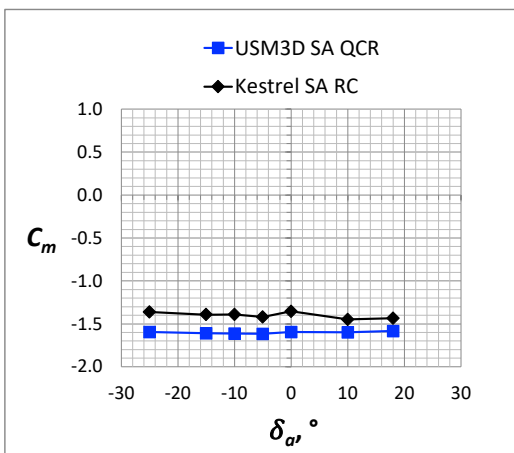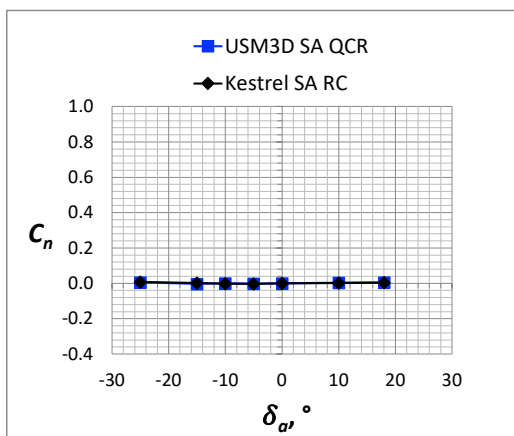
(a) Lift Coefficient

(b) Drag Coefficient

(c) Side Force Coefficient

(d) Rolling Moment Coefficient

(e) Pitching Moment Coefficient

(f) Yawing Moment Coefficient
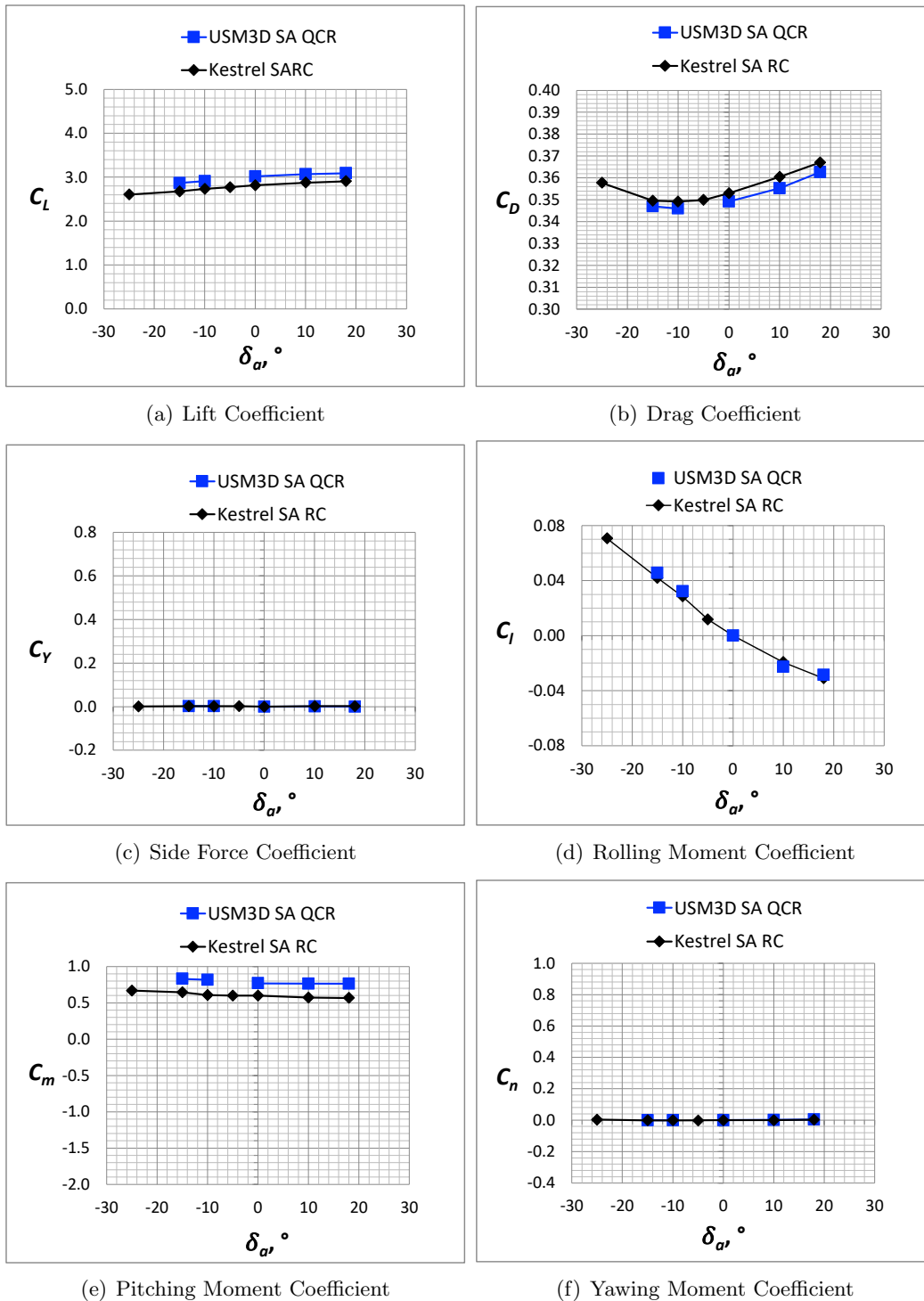
Figure 50. Code Comparisons of the Aerodynamic Coefficients with a Right Aileron Deflection for the Landing Configuration at 58 KEAS and $\alpha = 2°$. High-Lift Blowing at 5035 RPM, $T = 50.65$ lbf, and $Q = 16.23$ lbf-ft. Cruise Propellers at 1540 RPM, $T = $ -8.02 lbf, and $Q = 0.65$ lbf-ft.
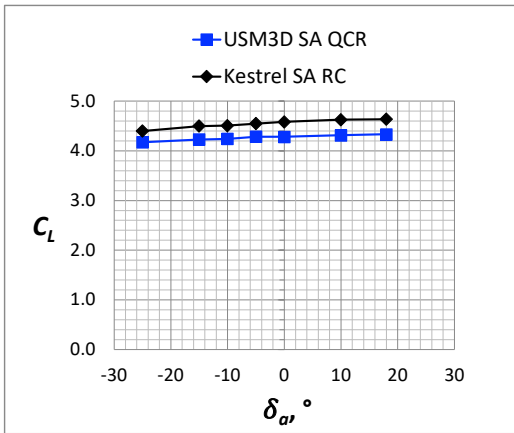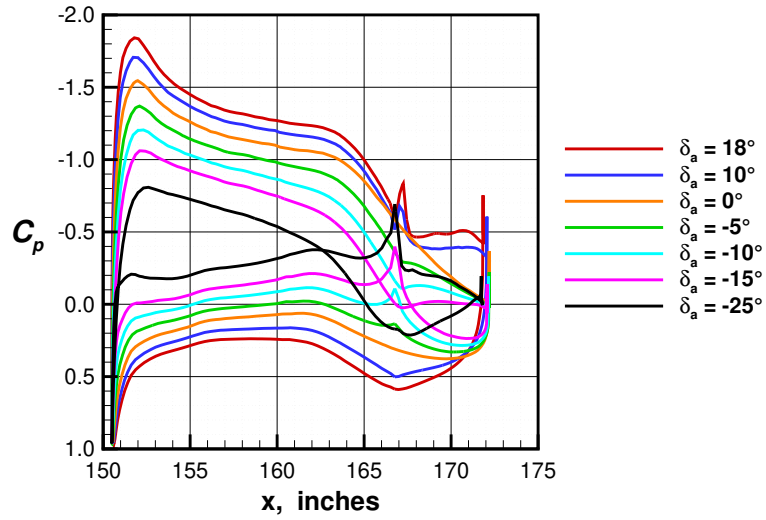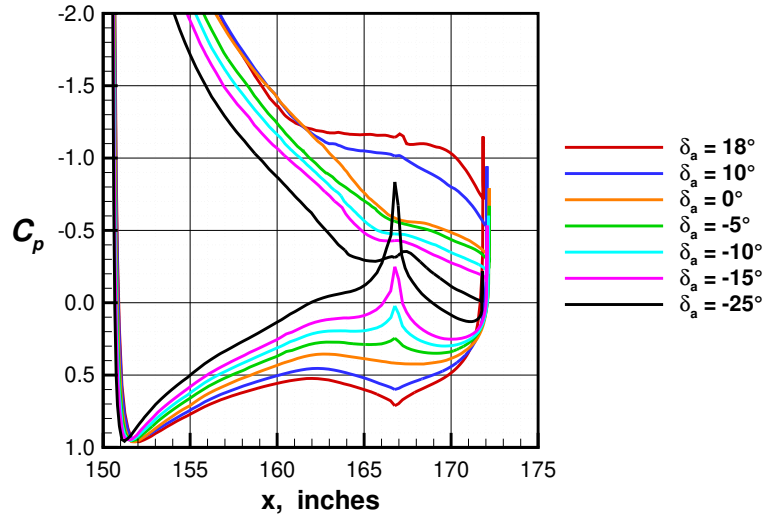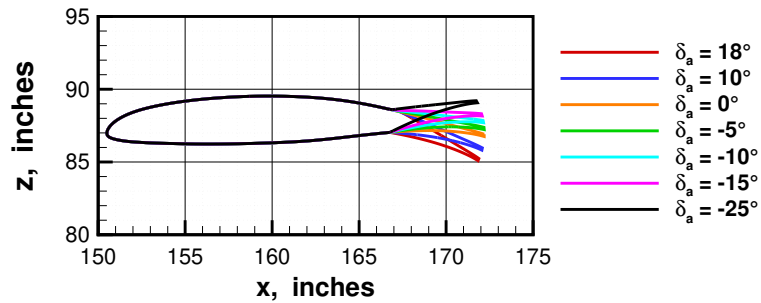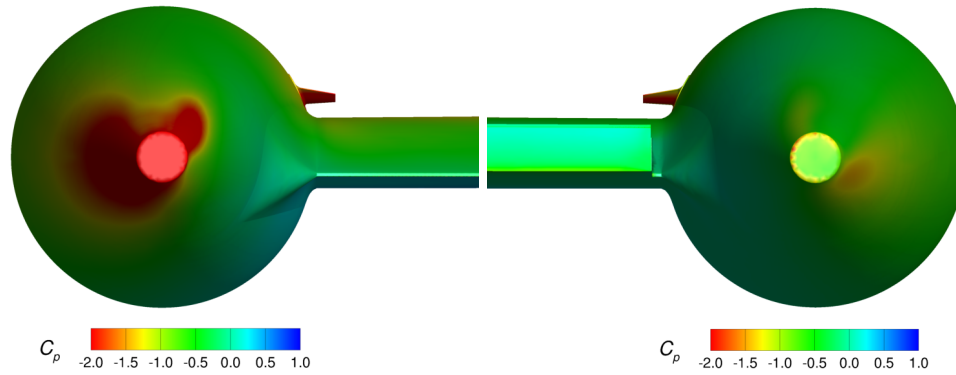
(a) Lift Coefficient
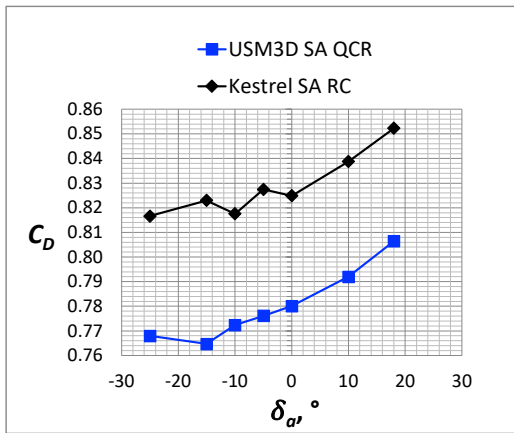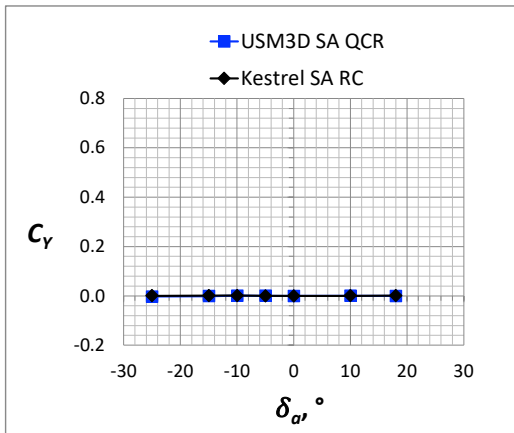
(b) Drag Coefficient

(c) Side Force Coefficient

(d) Rolling Moment Coefficient

(e) Pitching Moment Coefficient

(f) Yawing Moment Coefficient

Figure 51. Code Comparisons of the Aerodynamic Coefficients with a Right Aileron Deflection for the Landing Configuration at 58 KEAS and $\alpha = 14°$. High-Lift Blowing at 5035 RPM, $T = 50.65$ lbf, and $Q = 16.23$ lbf-ft. Cruise Propellers at 1540 RPM, $T = $ -8.02 lbf, and $Q = 0.65$ lbf-ft.
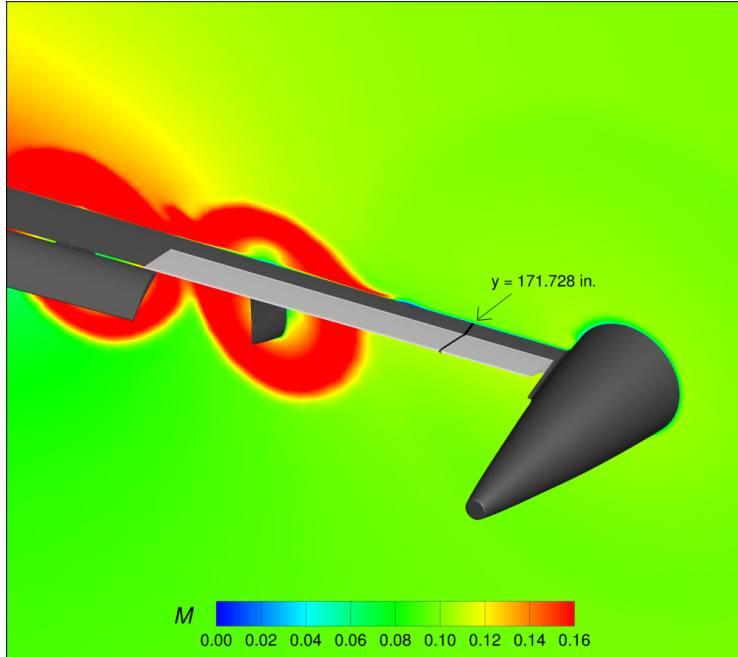
(a) x = 160 in.
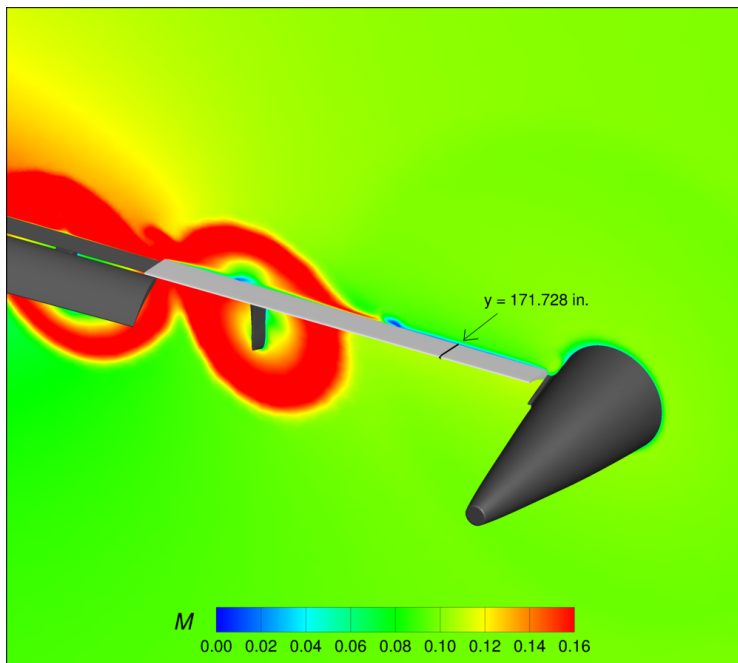
(b) x = 168 in.

Figure 52.   Mach Contours Illustrating the Propeller Wake for the Landing Configuration with a Right Aileron Deflection of $\delta_a = -25°$ for 58 KEAS and $\alpha = 2°$. High-Lift Blowing at 5035 RPM, $T = 50.65$ lbf, and $Q = 16.23$ lbf-ft. Cruise Propellers at 1540 RPM, $T = $ -8.02 lbf, and $Q = 0.65$ lbf-ft.

79

(a) C_p Distributions for $\alpha = 2°$

(b) C_p Distributions for $\alpha = 14°$

(c) Geometry Distributions

Figure 53. Comparisons of Pressure Coefficient Distributions at y = 171.728 inches, for the Landing Configuration with a Right Aileron Deflection at 58 KEAS. High-Lift Blowing at 5035 RPM, $T = 50.65$ lbf, and $Q = 16.23$ lbf-ft. Cruise Propellers at 1540 RPM, $T = $ -8.02 lbf, and $Q = 0.65$ lbf-ft.
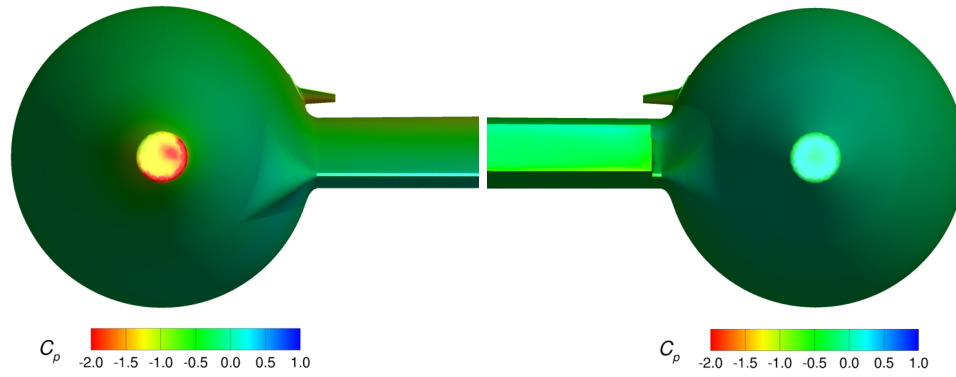
(a) Left Cruise Nacelle, Undeflected Aileron   (b) Right Cruise Nacelle, $\delta_a = -25°$

Figure 54. Pressure Coefficient on the Ailerons and Cruise Nacelles. Landing Configuration with $\delta_a = -25°$ at 58 KEAS and $\alpha = 2°$. High-Lift Blowing at 5035 RPM, $T = 50.65$ lbf, and $Q = 16.23$ lbf-ft. Cruise Propellers at 1540 RPM, $T = $ -8.02 lbf, and $Q = 0.65$ lbf-ft.
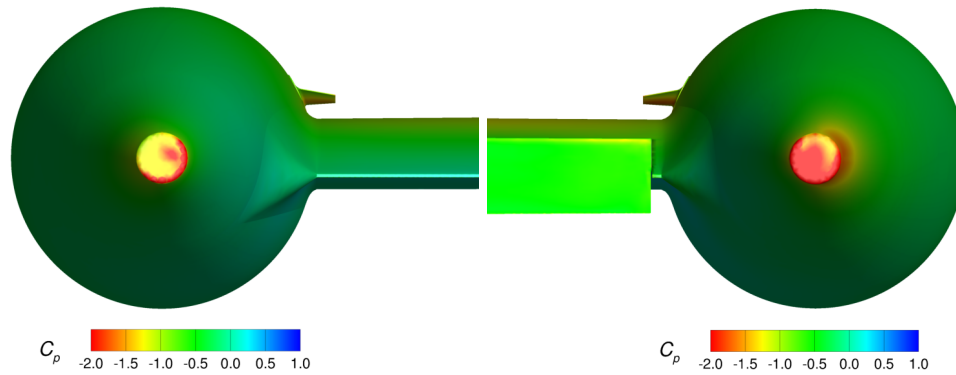

(a) Left Cruise Nacelle, Undeflected Aileron   (b) Right Cruise Nacelle, $\delta_a = 18°$

Figure 55. Pressure Coefficient on the Ailerons and Cruise Nacelles. Landing Configuration with $\delta_a = 18°$ at 58 KEAS and $\alpha = 2°$. High-Lift Blowing at 5035 RPM, $T = 50.65$ lbf, and $Q = 16.23$ lbf-ft. Cruise Propellers at 1540 RPM, $T = $ -8.02 lbf, and $Q = 0.65$ lbf-ft.

(a) Left Cruise Nacelle, Undeflected Aileron   (b) Right Cruise Nacelle, $\delta_a = -25°$

Figure 56. Pressure Coefficient on the Ailerons and Cruise Nacelles. Landing Configuration with $\delta_a = -25°$ at 58 KEAS and $\alpha = 14°$. High-Lift Blowing at 5035 RPM, $T = 50.65$ lbf, and $Q = 16.23$ lbf-ft. Cruise Propellers at 1540 RPM, $T = $ -8.02 lbf, and $Q = 0.65$ lbf-ft.
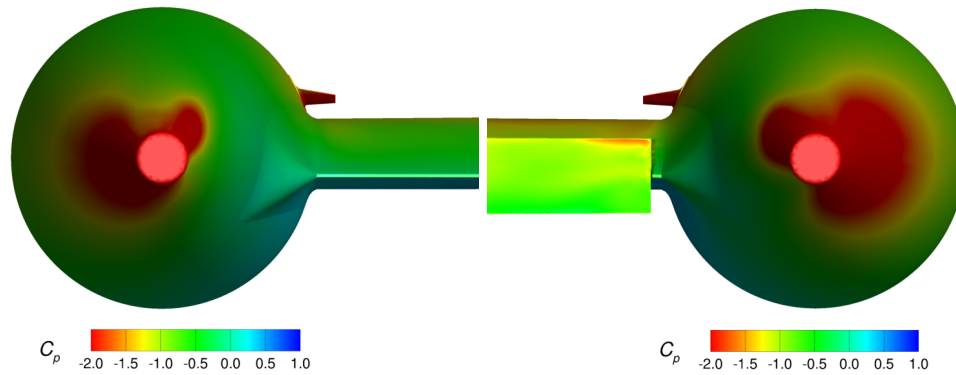
(a) Left Cruise Nacelle, Undeflected Aileron   (b) Right Cruise Nacelle, $\delta_a = 18°$

Figure 57. Pressure Coefficient on the Ailerons and Cruise Nacelles. Landing Configuration with $\delta_a = 18°$ at 58 KEAS and $\alpha = 14°$. High-Lift Blowing at 5035 RPM, $T = 50.65$ lbf, and $Q = 16.23$ lbf-ft. Cruise Propellers at 1540 RPM, $T = $ -8.02 lbf, and $Q = 0.65$ lbf-ft.
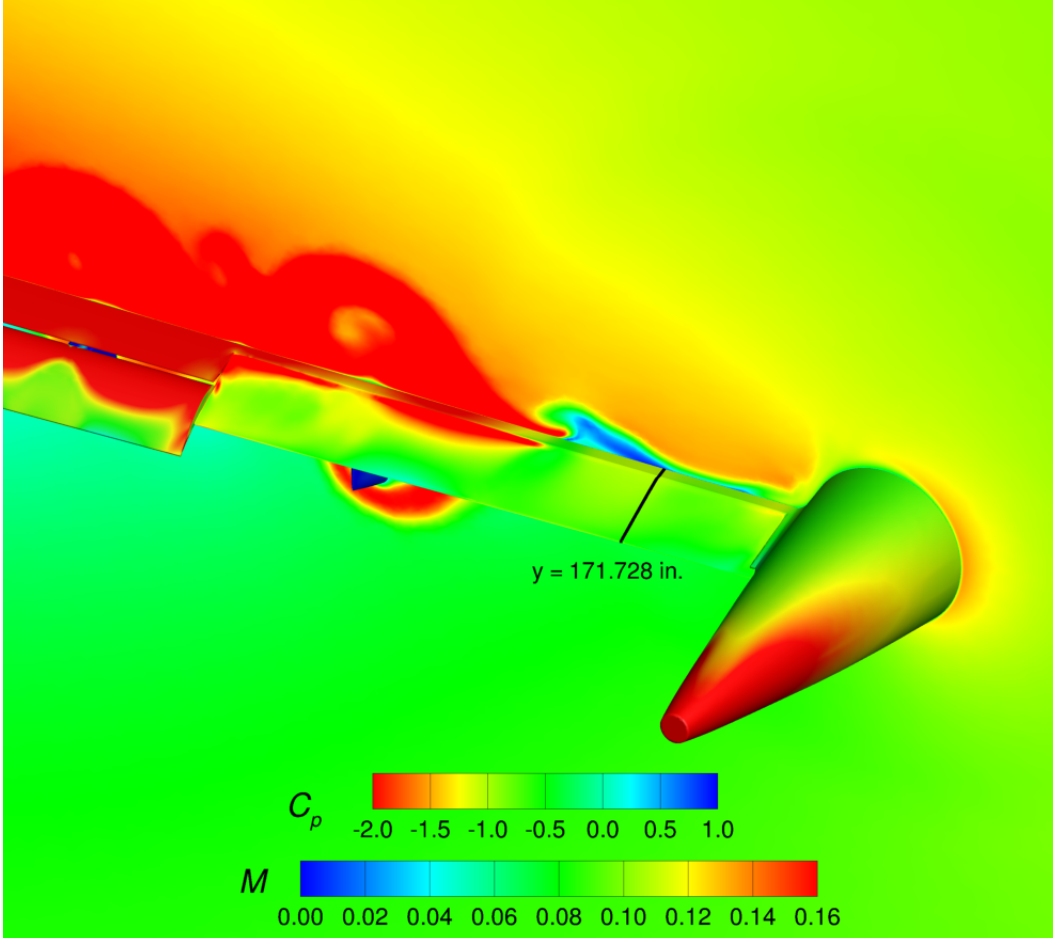
Figure 58. Pressure Coefficient on the Airplane Surface and Mach Contours at x = 166 inches. Landing Configuration with $\delta_a = 10°$ at 58 KEAS and $\alpha = 14°$. High-Lift Blowing at 5035 RPM, $T = 50.65$ lbf, and $Q = 16.23$ lbf-ft. Cruise Propellers at 1540 RPM, $T = -8.02$ lbf, and $Q = 0.65$ lbf-ft.

4 Conclusions

The X-57 Maxwell is an all-electric airplane with a distributed electric propulsion system for high-lift augmentation at takeoff and landing conditions. The Kestrel and USM3D computational fluid dynamics flow solvers were used at NASA Langley to investigate the aerodynamic performance and aileron effectiveness of the X-57 airplane. The landing configuration investigated in this paper had a flap deflection of 30° with the distributed electric propulsion system operating high-lift blowing propellers. The aileron effectiveness was investigated with the pilot's right aileron deflected, while keeping the left aileron undeflected. The flow conditions were an airspeed of 58 knots equivalent airspeed, an altitude of 6000 feet, and a flight unit Reynolds number of 0.588E+06 per foot. The high-lift propellers and idle-power

cruise propellers were modeled with an actuator disk model. The high-lift blowing conditions per propeller were at 5035 RPM, a thrust of 50.65 lbf, and a torque of 16.23 lbf-ft. The cruise propellers conditions were at 1540 RPM, an idling thrust of -8.02 lbf, and torque of 0.65 lbf-ft.

The X-57 Maxwell achieves its maximum lift at landing from a combination of a flap deflection of 30° and high lift blowing from the distributed electric propulsion system. The 30° flap deflection, without high-lift blowing, adds a linear increment of about $\Delta C_L = 0.84$ and the lift curve slope follows the 2π/radian of the basic airfoil theory for moderate angles of attack. The high-lift blowing adds a $\Delta C_L = 1.1$ at $\alpha = 0°$ but the lift curve slope is higher than the unblown case. Initially, at $\alpha = 0°$, the lift curve slope is 1.9 times the 2π/radian lift-curve slope, and the slope does decrease with increasing angle of attack, up to maximum lift at $\alpha = 12°$. This increase in lift curve slope with the high-lift blowing is because the powered lift from the distributed electric propulsion system increases the flow turning, compared to the unblown configuration. The effective turning from high-lift blowing decreases as angle of attack increases. It is also worth noting that the wing area, the characteristic dimension for conversion of forces to coefficients, has been reduced 58% compared to the P2006 Tecnam base aircraft, with the same fuselage and empennage wetted area. Therefore, the value of the X-57 drag coefficient is scaled 58% higher than the Tecnam drag coefficient at similar drag force values. The small wing area, combined with the high value of the zero-lift drag coefficient and the high operating lift coefficients (induced drag), push the actual value of the X-57 drag coefficients to a higher range than is typical for General Aviation aircraft.

There were negligible differences in lift, drag, and pitching moment whether the idle-powered cruise propellers were modeled with the actuator disk or excluded from the simulation. Solutions were computed for an angle-of-attack sweep from $\alpha = -2°$ to $\alpha = 20°$ with no aileron deflection, the high-lift propellers blowing and the cruise propellers excluded from the simulation. Solutions were also computed with the high-lift propellers blowing and with idle-powered cruise propellers, for aileron deflections from $\delta_a = -25°$ to $\delta_a = 18°$, at $\alpha = -2°$ and at $\alpha = 14°$.

In general, the Kestrel and USM3D codes compared well for lift, drag, and pitching moment for the landing configuration with no aileron control. The lift coefficient predicted from the codes compared well up to $\alpha = 12°$. The Kestrel code, with SA RC turbulence model, predicted an increasing lift coefficient up to $C_{L,max}$= 4.65 at $\alpha = 15°$. The USM3D code with SA QCR turbulence model predicted an increasing lift coefficient up to $C_{L,max}$= 4.5 at $\alpha = 12°$, then the lift remained constant through $\alpha = 14°$. The probable culprit for the difference in lift coefficient for high angles of attack was the different options (RC vs QCR) used with the standard SA turbulence model. Unfortunately, both codes did not offer the same option to the standard SA turbulence model. The Kestrel code predicted more drag across the range of angle of attack than the USM3D code. The codes compared fairly well for pitching moment coefficient across the range of angle of attack. Further comparison of Kestrel and USM3D results to Star-CCM+ and LAVA show an improved comparison of lift at high angles of attack when the same options to the SA turbulence model were used. Although the maximum lift coefficient was slightly different between the four CFD codes, all codes predict lift well above the

X-57 Maxwell airplane powered landing goal of a maximum lift coefficient of 4.0.

The Kestrel results indicate good aileron effectiveness at both $\alpha = 2°$ and $\alpha = 14°$, with slightly better rolling moment from negative aileron deflections. The Kestrel and USM3D codes compared well for aileron effectiveness at $\alpha = 2°$. However, the Kestrel code predicts better aileron effectiveness at $\alpha = 14°$ than USM3D. There was more flow separation in the region outboard of the last high-lift nacelle for the USM3D solutions at $\alpha = 14°$, which diminished the ability of the aileron to be effective at rolling the airplane. The Kestrel code predicted that aileron effectiveness was essentially independent of angle of attack for both $\alpha = 2°$ and $\alpha = 14°$, but effectiveness may be diminished for higher angles of attack since results showed massive flow separation outboard of the last high-lift nacelle and ahead of the aileron for $\alpha = 16°$.

The primary effects of the aileron deflection on the configuration aerodynamic coefficients were on rolling moment and drag, with a slight impact on lift and pitching moment, and minimal influence on side force and yawing moment. There was almost a constant difference in drag between the Kestrel and USM3D results for each of the studied angles of attack, 2° and 14°, most likely from the turbulence model differences between RC and QCR. For the Kestrel results, the effect on drag with positive aileron deflection (down) was an increase in drag for both $\alpha = 2°$ and $\alpha = 14°$. For $\alpha = 2°$, the drag increased $\Delta C_D = 0.0141$, which was a 4.0% increase in configuration drag for the right aileron deflected down $\delta_a = 18°$. For $\alpha = 14°$, the drag increased $\Delta C_D = 0.0274$, which was an increase of 3.3% in the configuration drag for $\delta_a = 18°$. For negative aileron deflections, the trend in drag change from the undeflected case was different between $\alpha = 2°$ and $\alpha = 14°$. At $\alpha = 2°$, for aileron deflections of $\delta_a = -5°$ and $\delta_a = -10°$ the drag decreased slightly, $\Delta C_D = -0.0038$. At $\alpha = 2°$ and aileron deflection $\delta_a = -25°$, the drag increased from the minimum drag with an increase of $\Delta C_D = 0.0086$ due to lower surface flow separation from the aileron. However, for the $\alpha = 14°$ case, the drag generally decreased with decreasing aileron deflection (up deflection) to a minimum drag at $\delta_a = -25°$, with a $\Delta C_D = -0.0083$ compared to the undeflected case. At $\alpha = 14°$, the maximum aileron deflected trailing edge down ($\delta_a = -18°$) resulted in the largest flow separation and the maximum drag, while the rotating the aileron trailing edge up reduced flow separation and decreased drag to a minimum at $\delta_a = -25°$.

References

1. Borer, N. K.; Patterson, M. D.; Viken, J. K.; Moore, M. D.; Clarke, S.; Redifer, M. E.; Christie, R. J.; Stoll, A., Dubois, A.; Bevirt, J.; and Gibson, A. R., Foster, T. J.; and Osterkamp, P. G.: Multidimensional Design and Performance of the NASA SCEPTOR Distributed Electric Propulsion Flight Demonstrator. AIAA 2016-3920, June 2016.

2. Patterson, M. D.; Derlaga, J. M.; and Borer, N. K.: High-Lift Propeller System Configuration Selection for NASA's SCEPTOR Distributed Electric Propulsion Flight Demonstrator. 16th AIAA Aviation Technology, Integration, and Operations Conference. AIAA 2016-3922, June 2016.

3. Borer, N. K.; Patterson, M. D.; Derlaga, J. M.; Litherland, B. L.; Deere, K. A.; and Stoll, A.: Flight Performance Maneuver Planning for NASA's X-57 "Maxwell" Flight Demonstrator- Part 1: Power-off Glides. AIAA Aviation 2019 Forum. AIAA 2019-2855, June 2019.

4. Borer, N. K.; Patterson, M. D.; Derlaga, J. M.; Litherland, B. L.; Deere, K. A.; and Stoll, A.: Comparison of Mixed-Order Aero-Propulsive Performance Predictions for Distributed Electric Propulsion Configurations. Invited paper for AIAA Transformational Flight Program Committee. AIAA 2016-3981, June 2016.

5. Borer, N. K.; Derlaga, J. M.; Deere, K. A.; Carter, M. B.; Viken, S. A.; Patterson, M. D.; Litherland, B. L.; and Stoll, A.: Comparison of Aero-Propulsive Performance Predictions for Distributed Electric Propulsion Configurations. Invited paper for AIAA Transformational Flight Program Committee. AIAA 2017-0209, January 2017.

6. Viken, J. K.; Viken, S. A.; Deere, K. A.; and Carter, M. B.; Design of the Cruise and Flap Airfoil for the X-57 Maxwell Distributed Electric Propulsion Aircraft. Aviation Forum 2017, 35th AIAA Applied Aerodynamics Conference, AIAA 2017-3922, June 2017.

7. Deere, K. A.; Viken, J. K.; Viken, S. A.; Carter, M. B.; Wiese, M. R.; and Farr, N. L.: Computational Analysis of a Wing Designed for the X-57 Distributed Electric Propulsion Aircraft. Aviation Forum 2017, 35th AIAA Applied Aerodynamics Conference, AIAA 2017-3923, June 2017.

8. Deere, K. A.; Viken, S. A.; Carter, M. B.; Viken, J. K.; Derlaga, J. M.; and Stoll, A.: Comparison of High-Fidelity Computational Tools for Wing Design of a Distributed Electric Propulsion Aircraft. Aviation Forum 2017, 35th AIAA Applied Aerodynamics Conference, AIAA 2017-3925, June 2017.

9. Deere, K. A.; Viken, S. A.; Carter, M. B.; Viken, J. K.; Wiese, M. R.; and Farr, N. L.: Computational Analysis of Powered Lift Augmentation for the LEAPTech Distributed Electric Propulsion Wing. Aviation Forum 2017, 35th AIAA Applied Aerodynamics Conference, AIAA 2017-3921, June 2017.

10. Deere, K. A.; Viken, J. K.; Viken, S. A.; Carter, M. B.; Cox, D.; Wiese, M. R.; and Farr, N. L.: Computational Component Build-up for the X-57 Distributed Electric Propulsion Aircraft. SciTech AIAA 2018-1275, January 2018.

11. van der Meer, S.; and Veldhuis, L.: Numerical Assessment of Directional Stability and Control with Tip-mounted Propellers. Master's Thesis at the Delft University of Technology, January 24, 2020.

12. Deere, K. A.; Viken, J. K.; Viken, S. A.; Carter, M. B.; Cox, D.; Wiese, M. R.; and Farr, N. L.: Computational Analysis of the X-57 Maxwell Airplane at Unpowered Conditions (Preliminary Fuselage). NASA TM-20210011034, April 2022.

13. Frink, N. T.; Pirzadeh, S. Z.; Parikh, P. C.; Pandya, M. J.; and Bhat, M. K.: The NASA Tetrahedral Unstructured Software System. The Aeronautical Journal, Vol. 104, No. 1040, October 2000, pp. 491–499.

14. Abdol-Hamid, K. S., Frink, N. T., Deere, K. A., and Pandya, M. J.: Propulsion Simulations Using Advanced Turbulence Models with the Unstructured-Grid CFD Tool, TetrUSS. AIAA 2004-0714, January 2004.

15. McDaniel, D. R., and Tuckey, T.R.: HPCMP CREATE-AV Kestrel New Capabilities and Future Directions. AIAA SciTech Forum, AIAA 2019-0840, 7-11 January 2019.

16. Shafer, T. C., Green, B. E., Hallissy, B. P., and Hine, D. H.: Advanced Navy Applications Using CREATE-AV Kestrel. AIAA SciTech Forum, AIAA 2014-0418, 13-17 January 2014.

17. Siemens Digital Industries Software, "Simcenter STAR-CCM+ Software," Costa Mesa, CA, Version 13.04.10, retrieved 30 June 2023. `https://www.plm.automation.siemens.com/global/en/products/simcenter/STAR-CCM.html`

18. Kiris, C. C., Housman, J. A., Barad, M. F., Brehm, C., Sozer, E., and Moini-Yeta, S.; Computational Framework for Launch, Ascent, and Vehicle Aerodynamics (LAVA). Aerospace Science and Technology, Vol. 55, 2016, pp. 189-219.

19. Yoo, S. Y.; Duensing, J. C.; Deere, K. A.; Viken, J. K., and Frederick, M. A.: Computational Analysis on the Effects of High-lift Propellers and Wingtip Cruise Propellers on the X-57 Airplane. AIAA-2023-3382, June 2023.

20. Duensing, J. C.; Yoo, S. Y.; Maldonado, D.; Housman, J. A.; Jensen, J. C.; and Kiris, C. C..: Establishing Best Practices for X-57 Maxwell CFD Database Generation. AIAA-2019-0274, January 2019.

21. Yoo, S., and Duensing, J.: Computational Analysis of the External Aerodynamics of the Unpowered X-57 Mod-III Aircraft. AIAA-2019-3698, June 2019.

22. Spalart, P. R.; and Allmaras, S. R.: A One-Equation Turbulence Model for Aerodynamic Flows. Recherché, No. 1, 1994, pp. 5-21.

23. Pao, S. P.: USMC6-TetrUSS Grid and Solution Cutter: A Brief Users' Guide. Version 4, NASA Langley Research Center. October 2008.

24. Drela, M., and Youngren, H.: XROTOR User Guide, updated 13 November 2003, retrieved 30 June 2023. `http://web.mit.edu/drela/Public/web/xrotor/xrotor_doc.txt`

25. Hahn, A.: Open Vehicle Sketch Pad Aircraft Modeling Strategies. 51st AIAA Aerospace Sciences Meeting including the New Horizons Forum and Aerospace Exposition. 2013.

26. Belben, J. B.; McDonald, R. A..: Enabling Rapid Conceptual Design Using Geometry-Based Multi-Fidelity Models in VSP. 51st AIAA Aerospace Sciences Meeting, AIAA2013-0328, January 2013.

27. Samareh, J.: GridTool: A Surface Modeling and Grid Generation Tool. Proceedings of the Workshop on Surface Modeling, Grid Generation, and Related Issues in CFD Solutions, NASA CP–3291, May 9–11, 1995.

28. Helden Aerospace Inc.: https://heldenaero.com/heldenmesh/ [retrieved 30 June 2023]

29. Pirzadeh, S.: Unstructured Viscous Grid Generation by Advancing-Layers Method. AIAA Journal, Vol. 32, No. 8, pp. 1735–1737, August 1994.

30. Pirzadeh, S.: Structured Background Grids for Generation of Unstructured Grids by Advancing Front Method. AIAA Journal, Vol. 31, No. 2, pp. 257–265, February 1993.

31. Second AIAA CFD High Lift Prediction Workshop Gridding Guidelines, https://hiliftpw.larc.nasa.gov/Workshop2/GriddingGuidelines-HiLiftPW2-v2.pdf March 2013. [retrieved 30 June 2023]

32. Deere, Karen A.; Viken, Jeffrey K.; Viken, Sally A.; Carter, Melissa B.; Wiese, Michael R.; and Farr, Norma L.: Computational Analysis of the X-57 Maxwell Airplane at Unpowered Conditions (Preliminary Fuselage). NASA TM-20210011034, May 2021.

Appendices

(a) Upper Surface
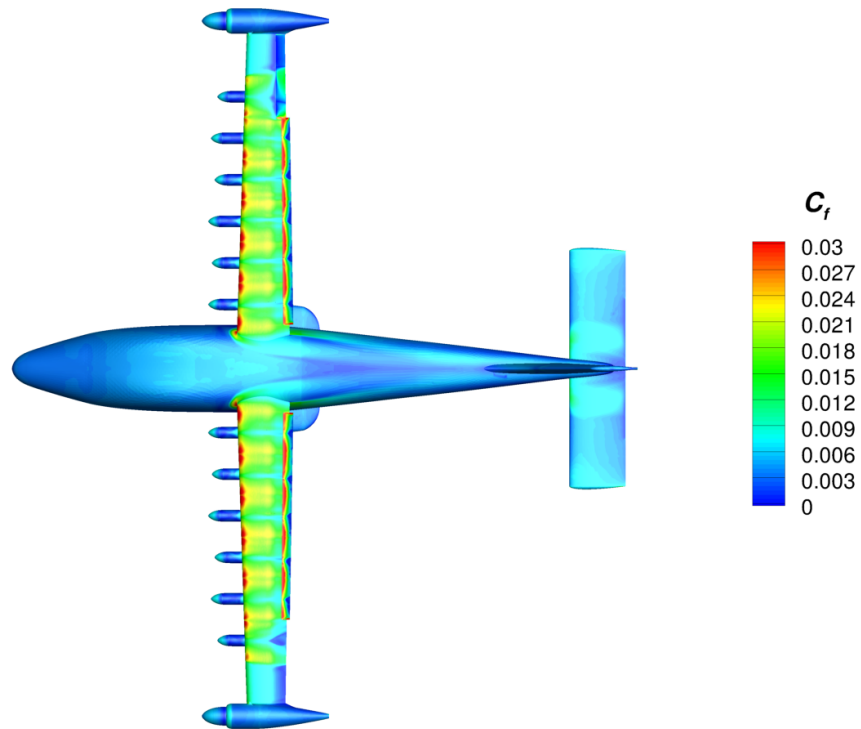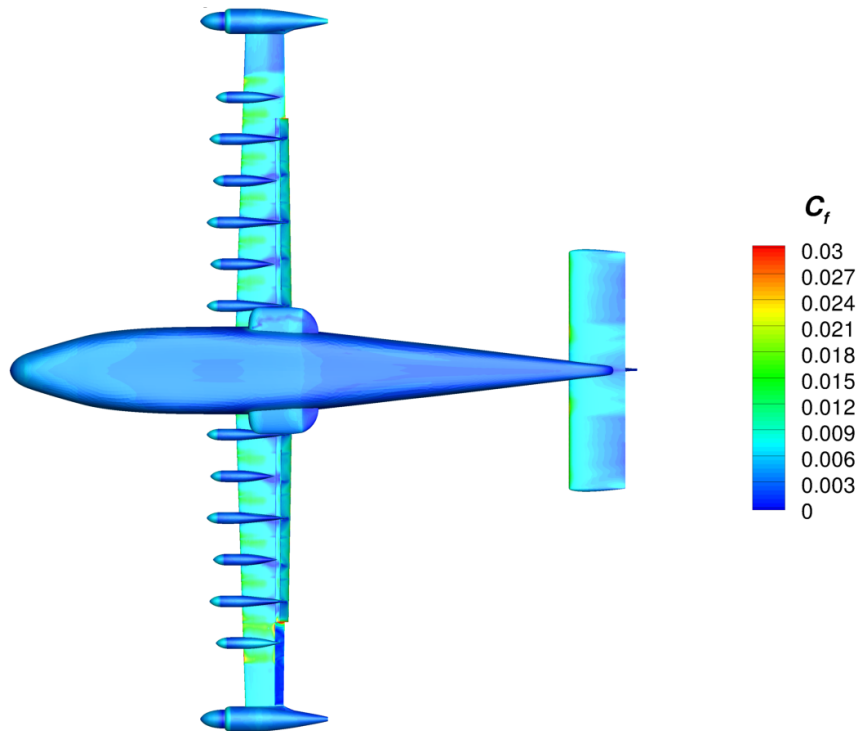
(b) Lower Surface

Figure 59. Skin Friction Coefficient for the Landing Configuration with $\delta_a = -25°$ at 58 KEAS and $\alpha = 2°$. High-Lift Blowing at 5035 RPM, $T = 50.65$ lbf, and $Q = 16.23$ lbf-ft. Cruise Propellers at 1540 RPM, $T = -8.02$ lbf, and $Q = 0.65$ lbf-ft. Kestrel SA RC.
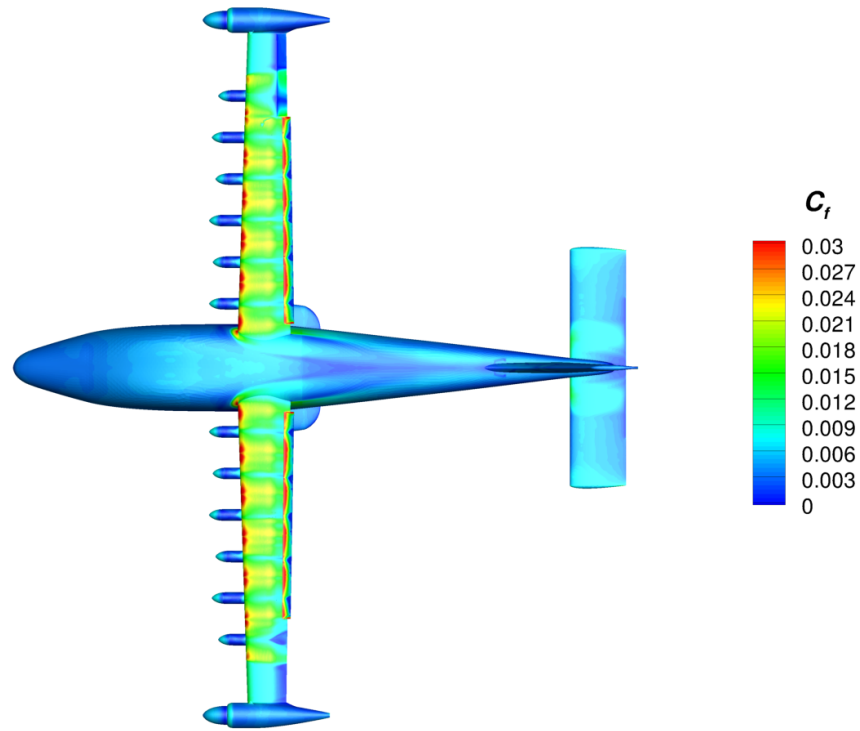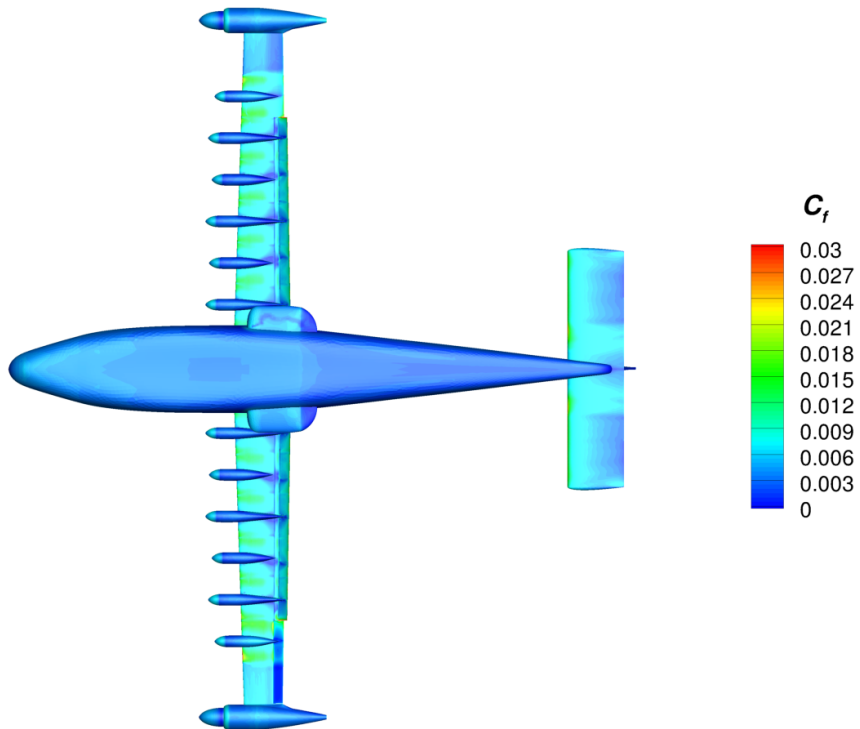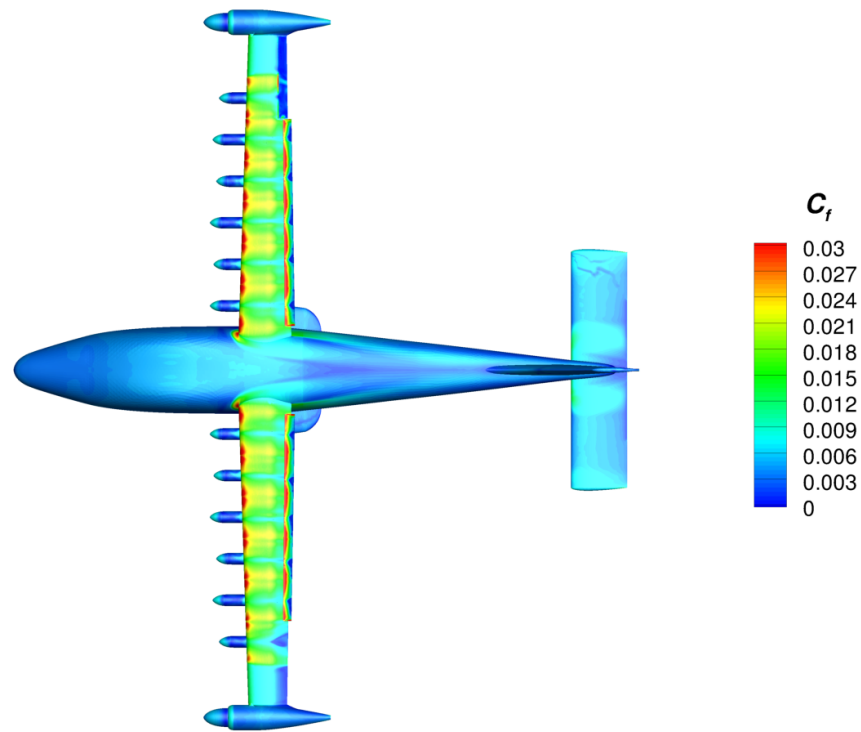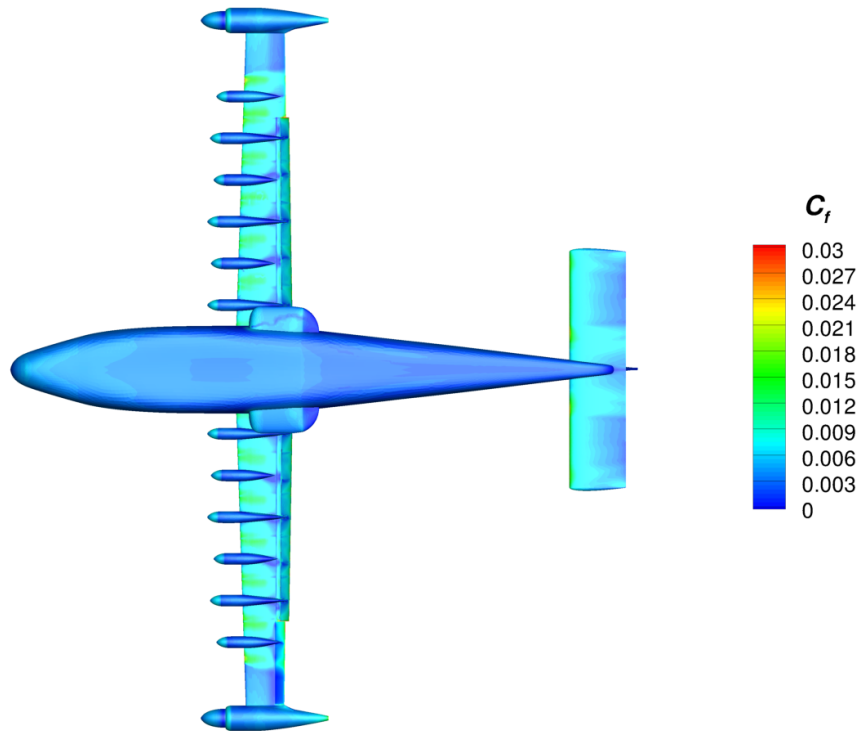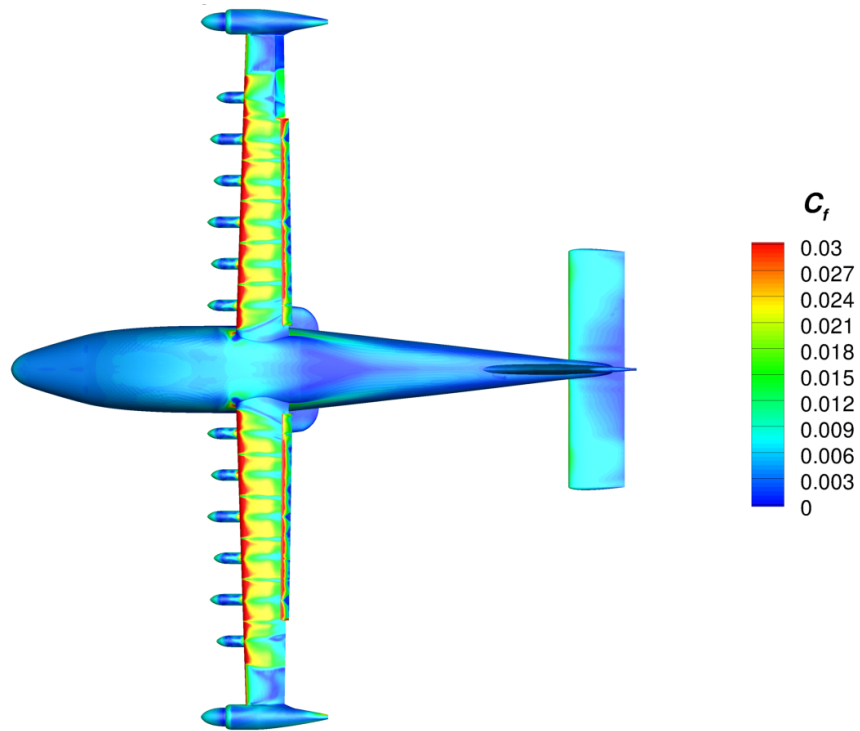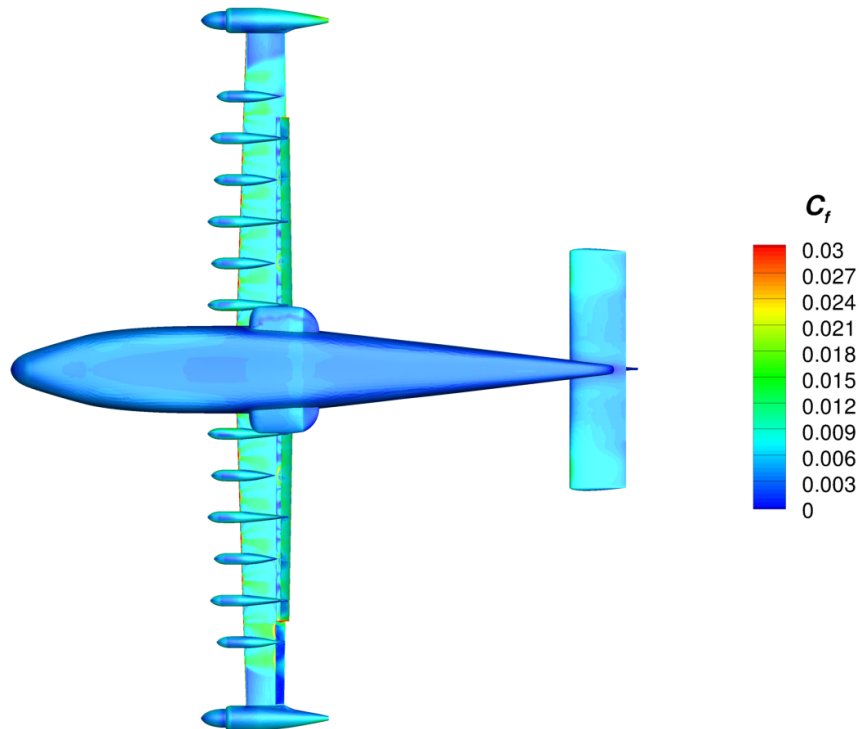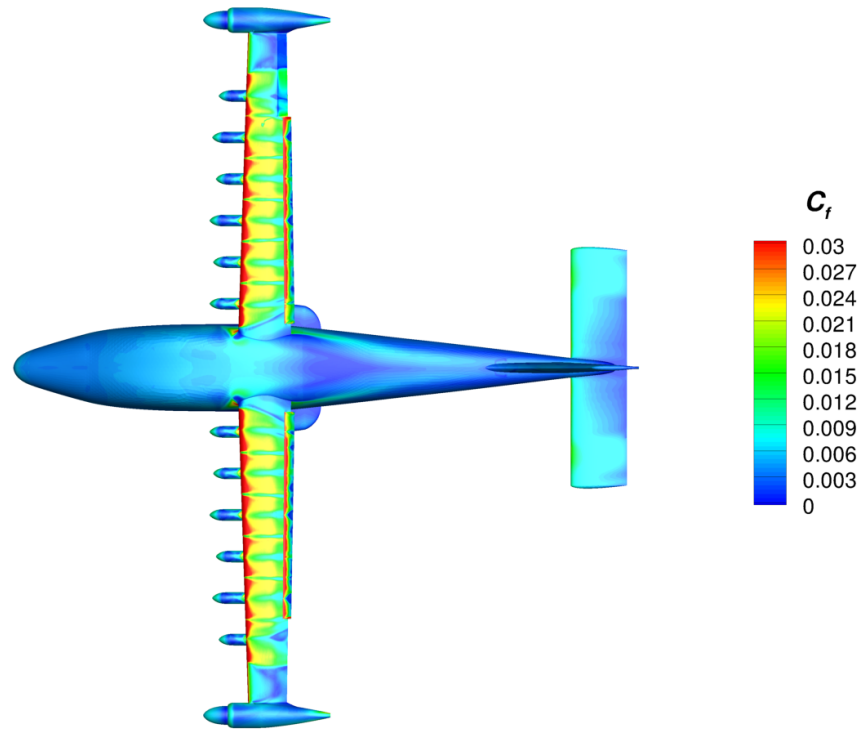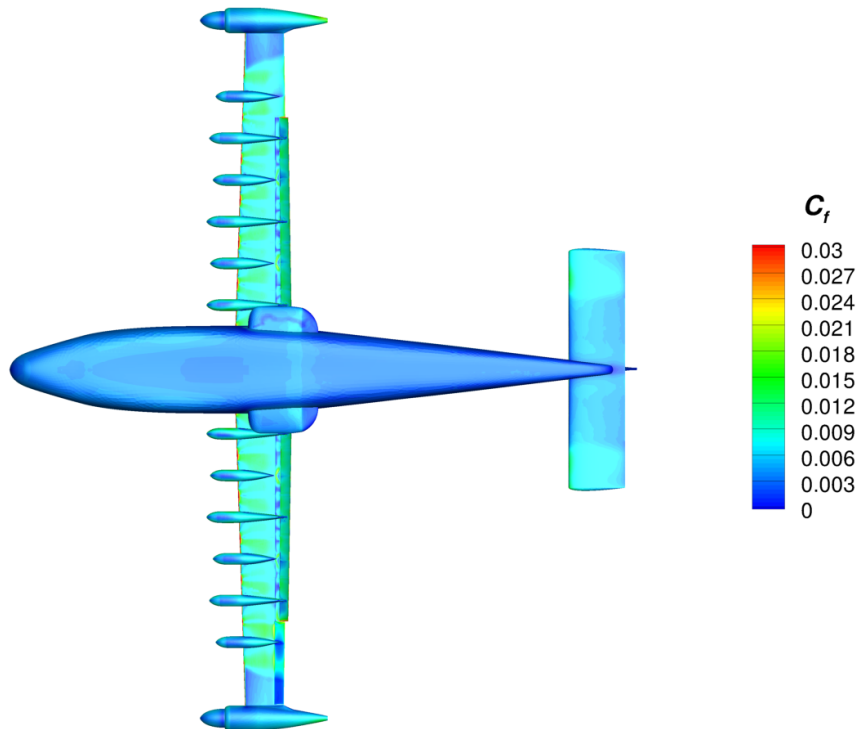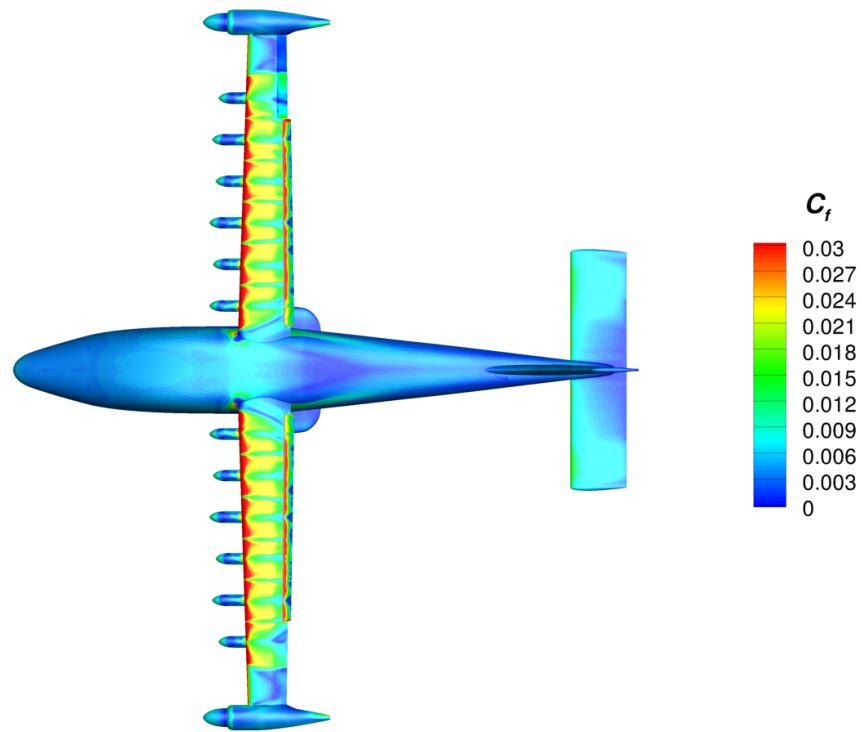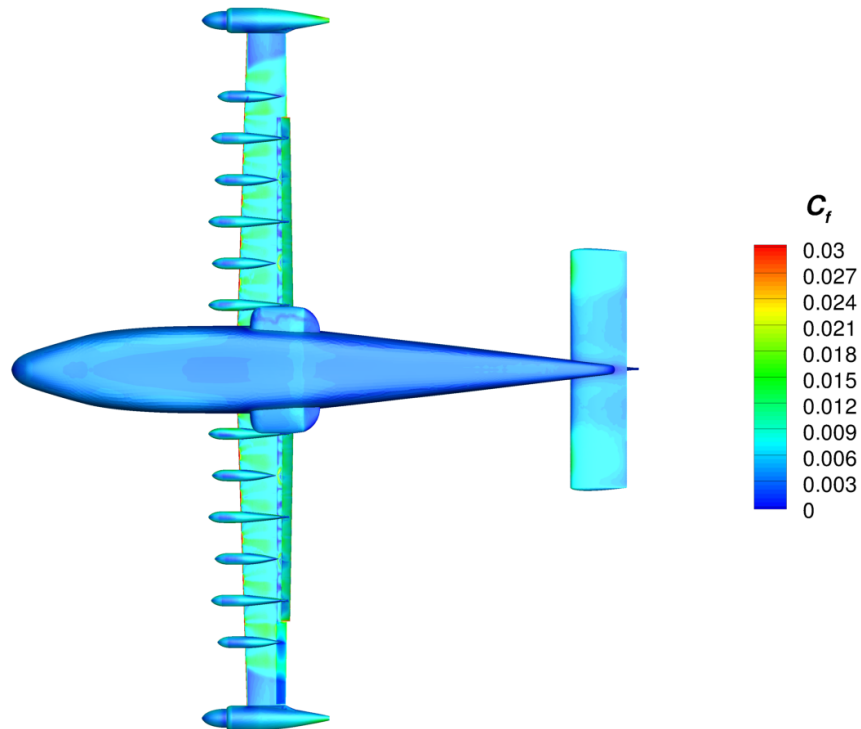
(a) Upper Surface

(b) Lower Surface

Figure 60. Skin Friction Coefficient for the Landing Configuration with $\delta_a = -15°$ at 58 KEAS and $\alpha = 2°$. High-Lift Blowing at 5035 RPM, $T = 50.65$ lbf, and $Q = 16.23$ lbf-ft. Cruise Propellers at 1540 RPM, $T = -8.02$ lbf, and $Q = 0.65$ lbf-ft. Kestrel SA RC.
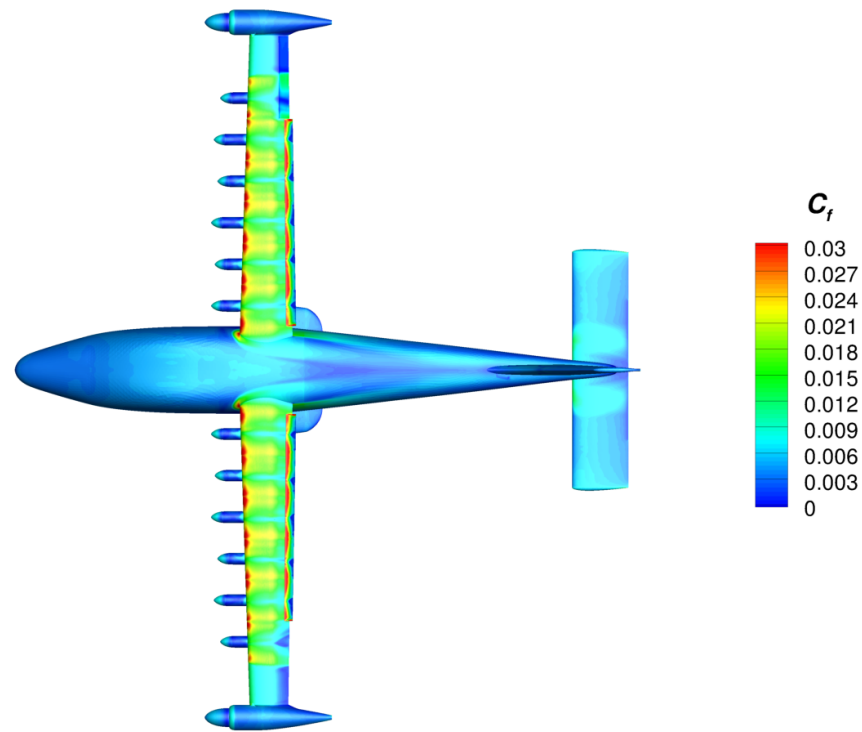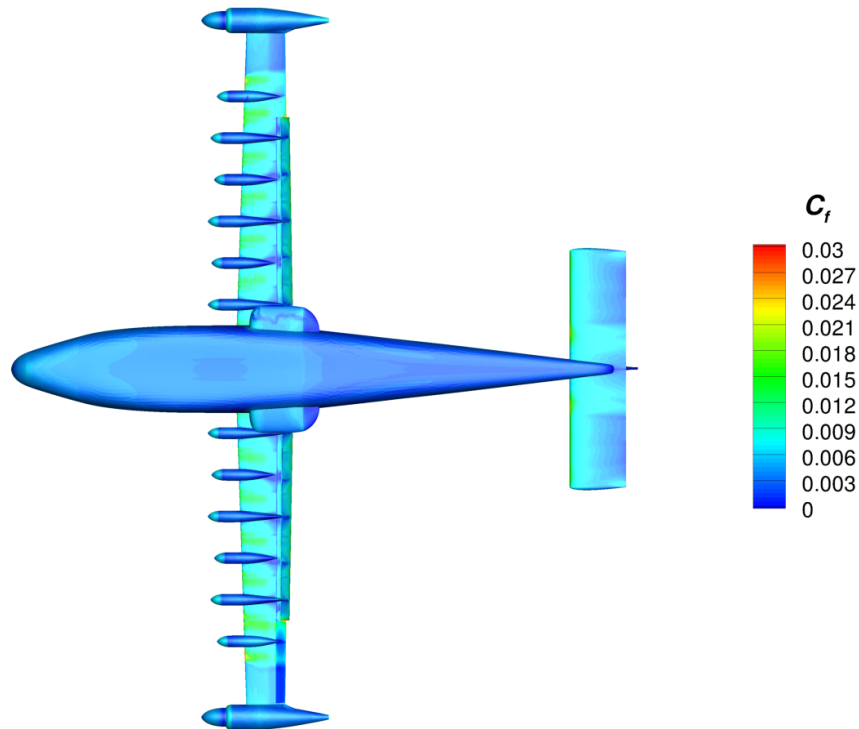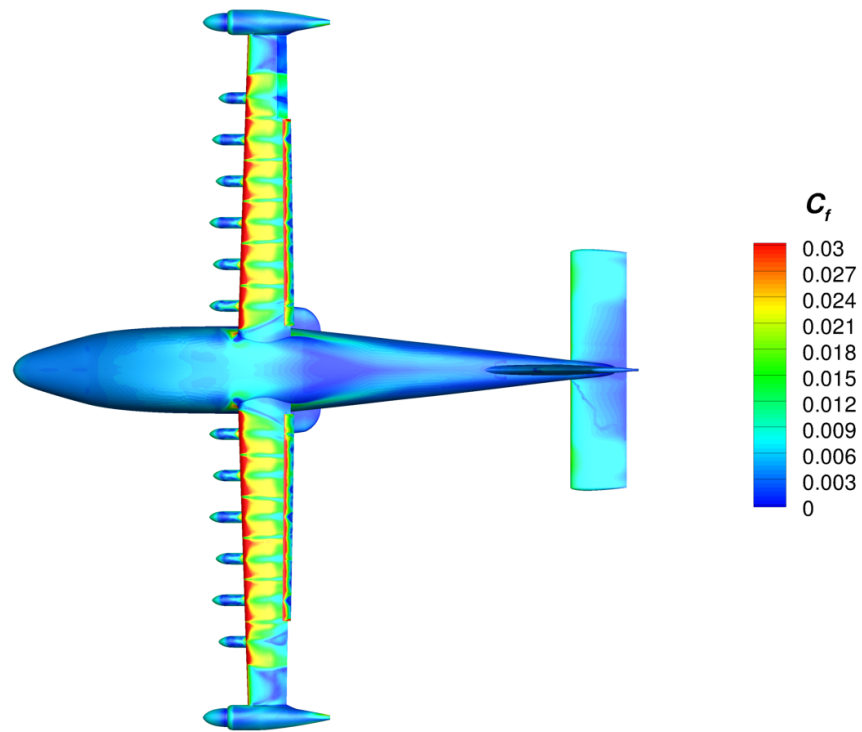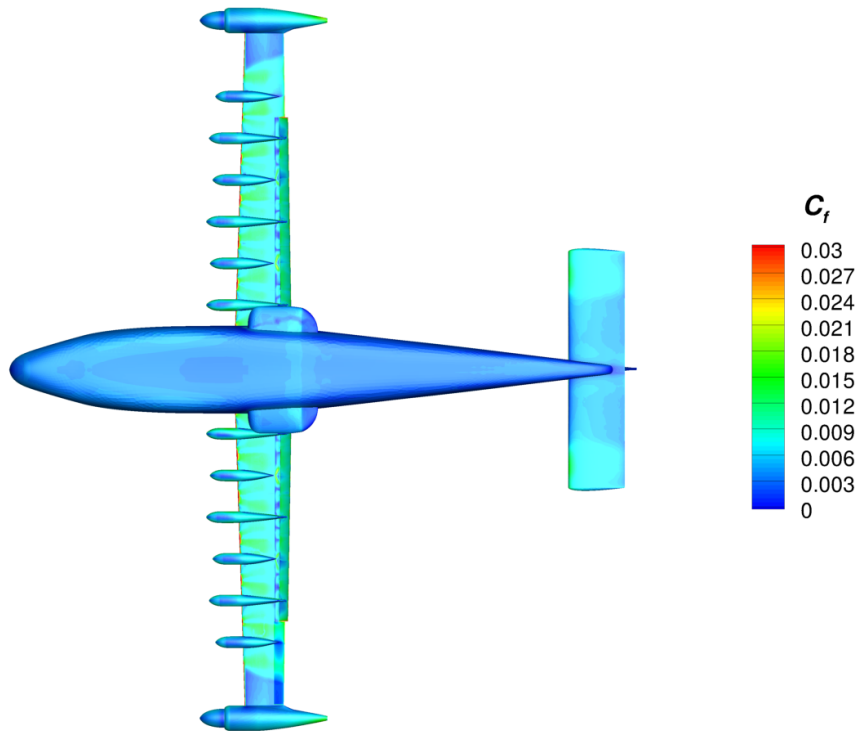
(a) Upper Surface

(b) Lower Surface

Figure 61. Skin Friction Coefficient for the Landing Configuration with $\delta_a = -10°$ at 58 KEAS and $\alpha = 2°$. High-Lift Blowing at 5035 RPM, $T = 50.65$ lbf, and $Q = 16.23$ lbf-ft. Cruise Propellers at 1540 RPM, $T = $ -8.02 lbf, and $Q = 0.65$ lbf-ft. Kestrel SA RC.
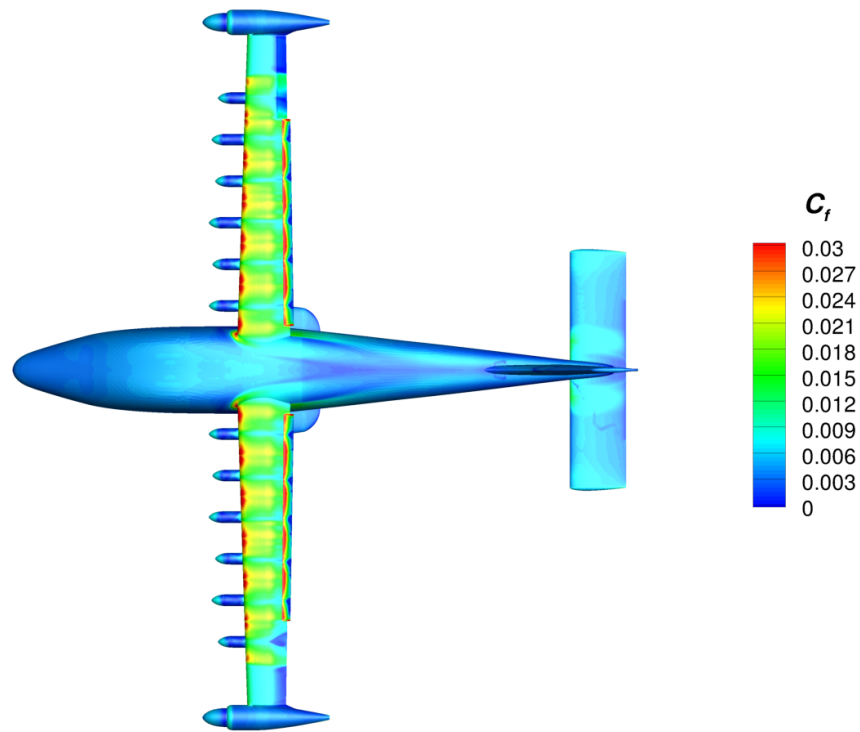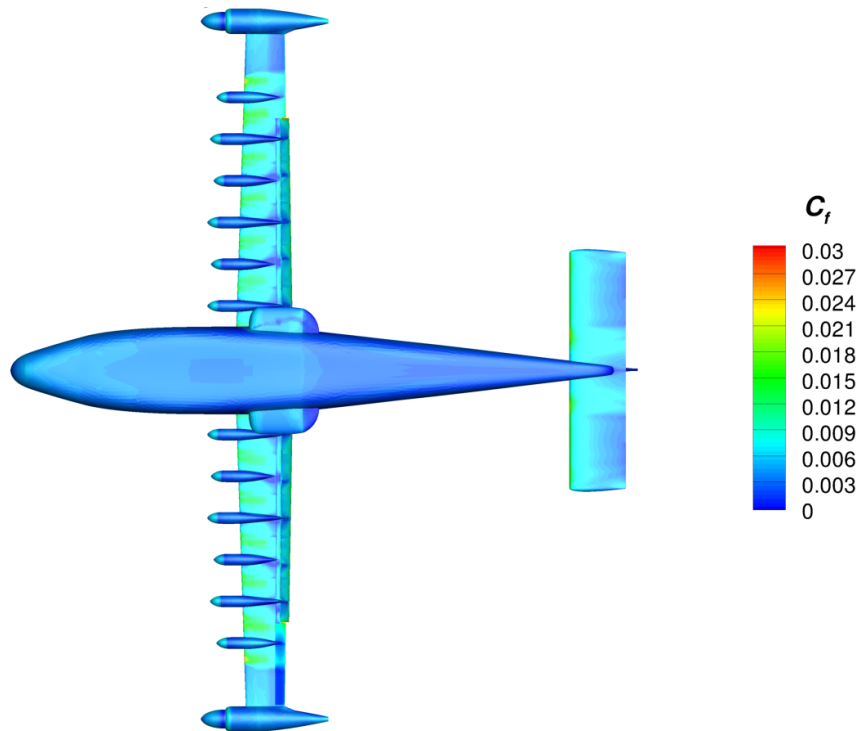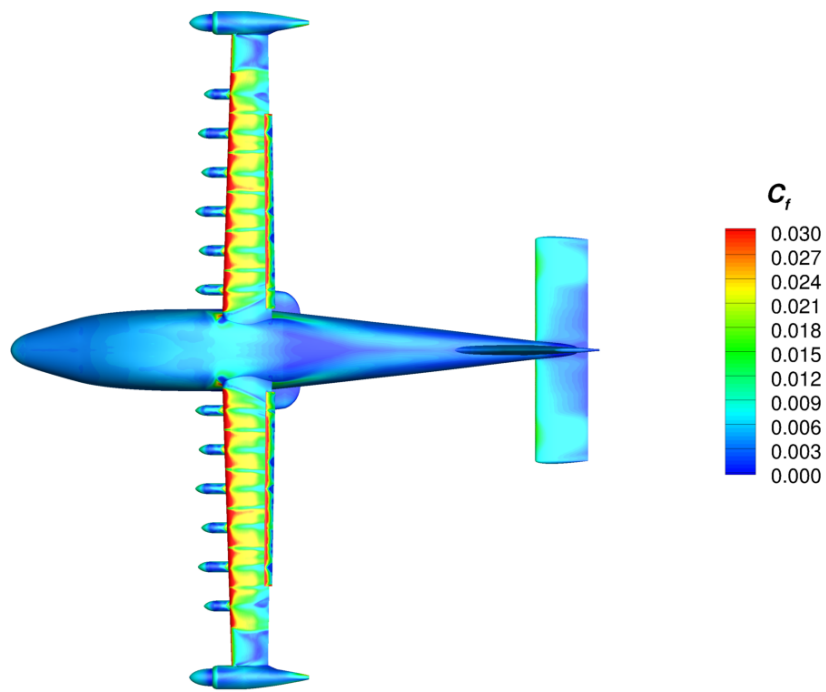
(a) Upper Surface

(b) Lower Surface

Figure 62. Skin Friction Coefficient for the Landing Configuration with $\delta_a = -5°$ at 58 KEAS and $\alpha = 2°$. High-Lift Blowing at 5035 RPM, $T = 50.65$ lbf, and $Q = 16.23$ lbf-ft. Cruise Propellers at 1540 RPM, $T = -8.02$ lbf, and $Q = 0.65$ lbf-ft. Kestrel SA RC.
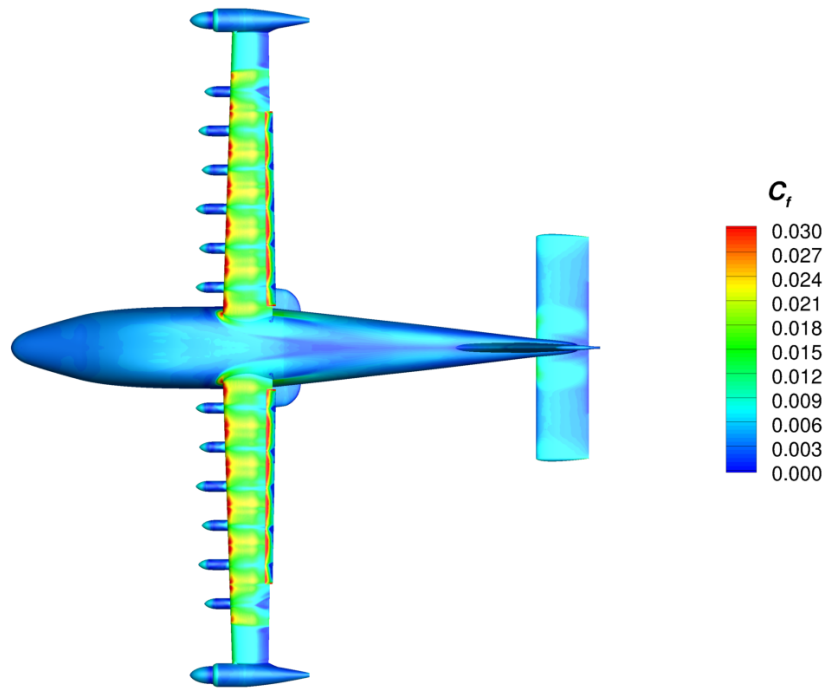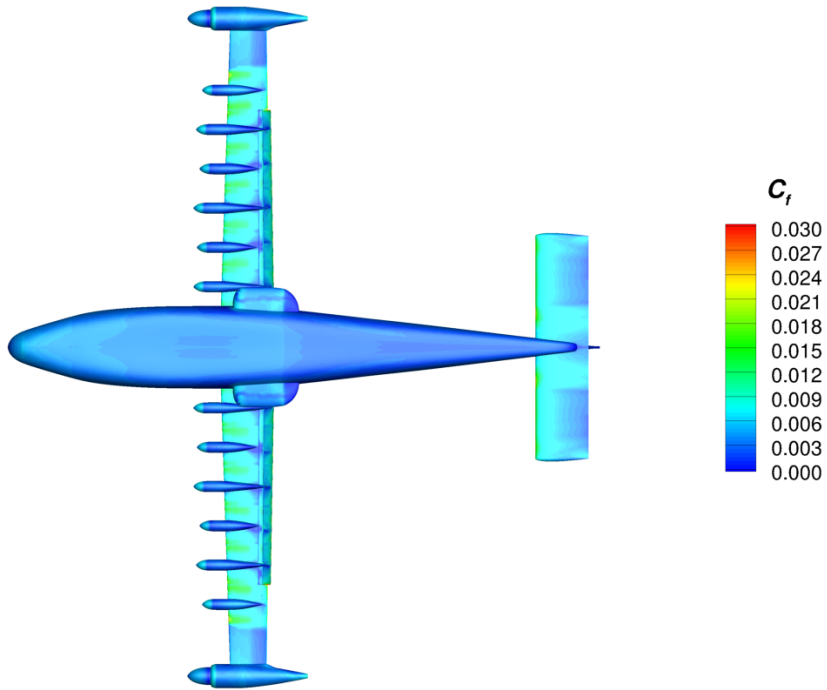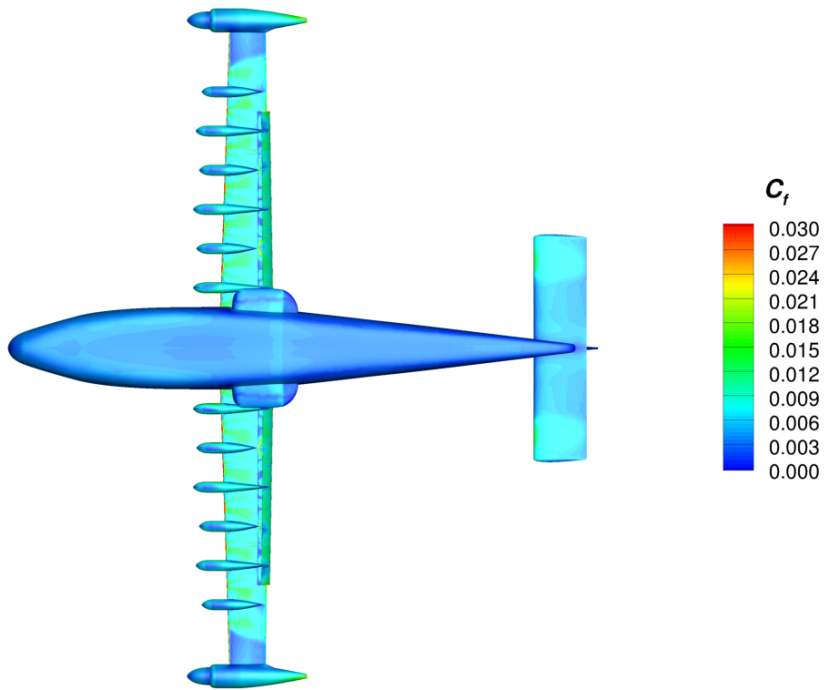
(a) Upper Surface

(b) Lower Surface

Figure 63. Skin Friction Coefficient for the Landing Configuration with $\delta_a = 0°$ at 58 KEAS and $\alpha = 2°$. High-Lift Blowing at 5035 RPM, $T = 50.65$ lbf, and $Q = 16.23$ lbf-ft. Cruise Propellers at 1540 RPM, $T = -8.02$ lbf, and $Q = 0.65$ lbf-ft. Kestrel SA RC.
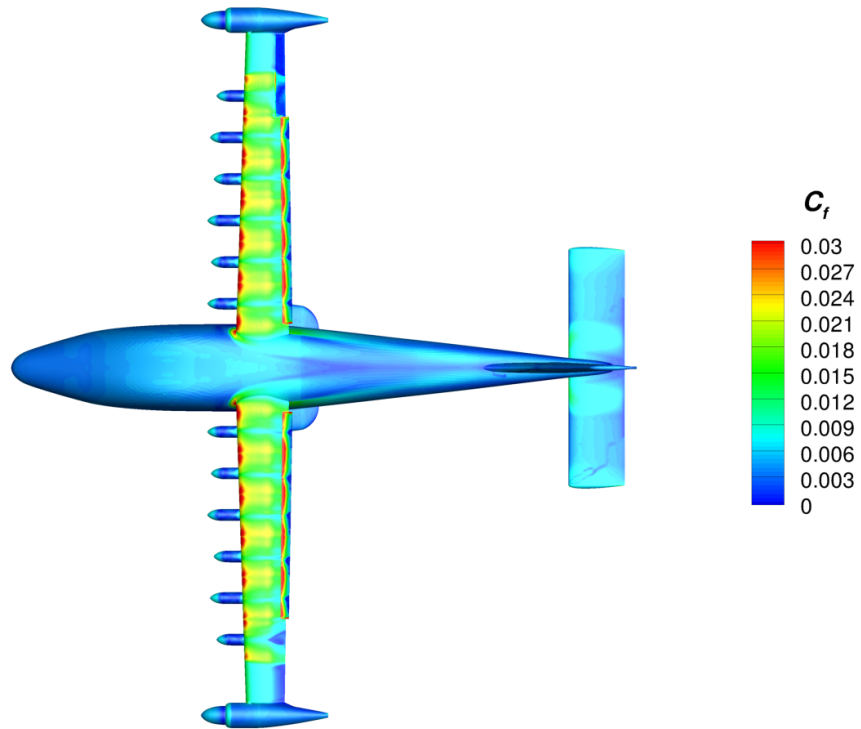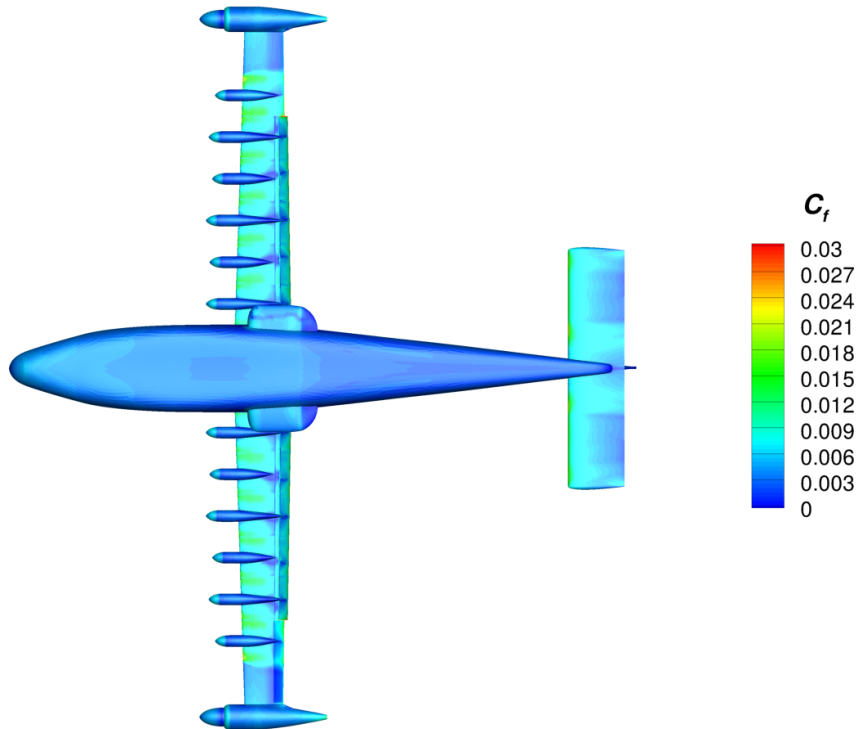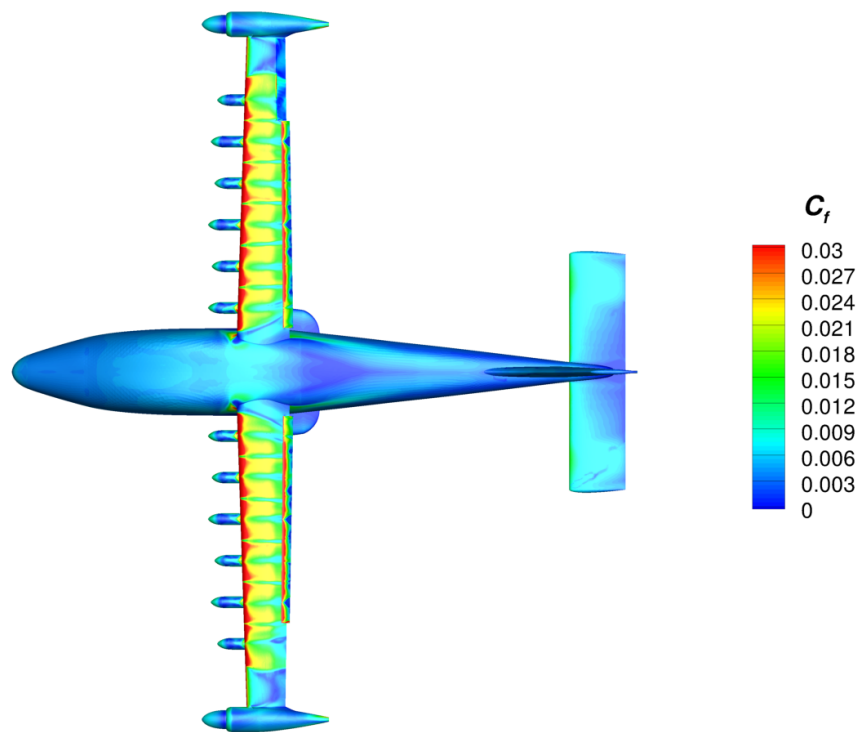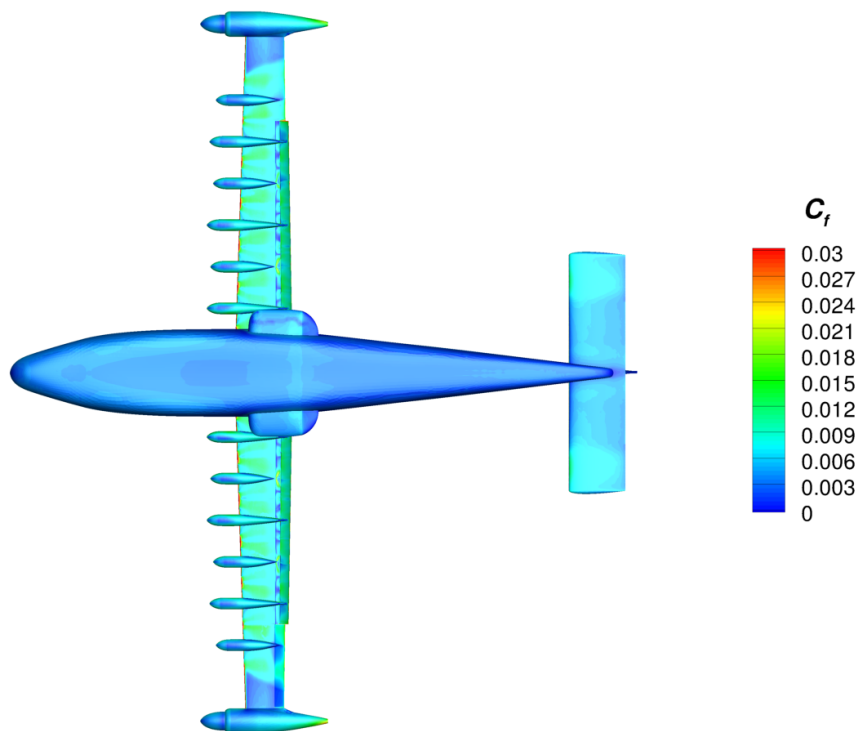
(a) Upper Surface

(b) Lower Surface

Figure 64. Skin Friction Coefficient for the Landing Configuration with $\delta_a = 10°$ at 58 KEAS and $\alpha = 2°$. High-Lift Blowing at 5035 RPM, $T = 50.65$ lbf, and $Q = 16.23$ lbf-ft. Cruise Propellers at 1540 RPM, $T = -8.02$ lbf, and $Q = 0.65$ lbf-ft. Kestrel SA RC.
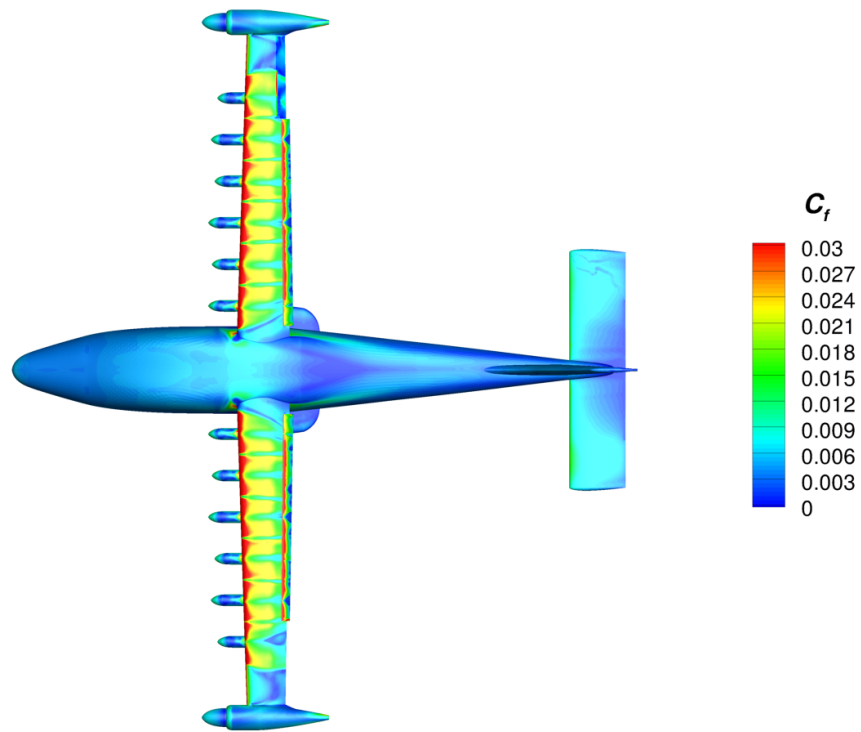
(a) Upper Surface

(b) Lower Surface

Figure 65. Skin Friction Coefficient for the Landing Configuration with $\delta_a = 18°$ at 58 KEAS and $\alpha = 2°$. High-Lift Blowing at 5035 RPM, $T = 50.65$ lbf, and $Q = 16.23$ lbf-ft. Cruise Propellers at 1540 RPM, $T = -8.02$ lbf, and $Q = 0.65$ lbf-ft. Kestrel SA RC.
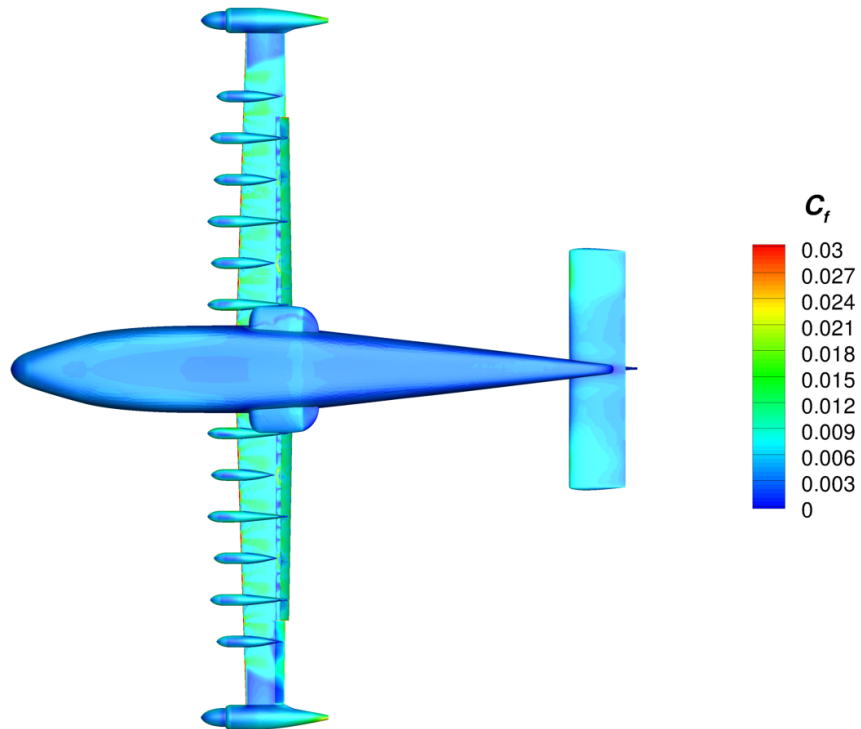
(a) Upper Surface

(b) Lower Surface

Figure 66. Skin Friction Coefficient for the Landing Configuration with $\delta_a = -25°$ at 58 KEAS and $\alpha = 14°$. High-Lift Blowing at 5035 RPM, $T = 50.65$ lbf, and $Q = 16.23$ lbf-ft. Cruise Propellers at 1540 RPM, $T = -8.02$ lbf, and $Q = 0.65$ lbf-ft. Kestrel SA RC.
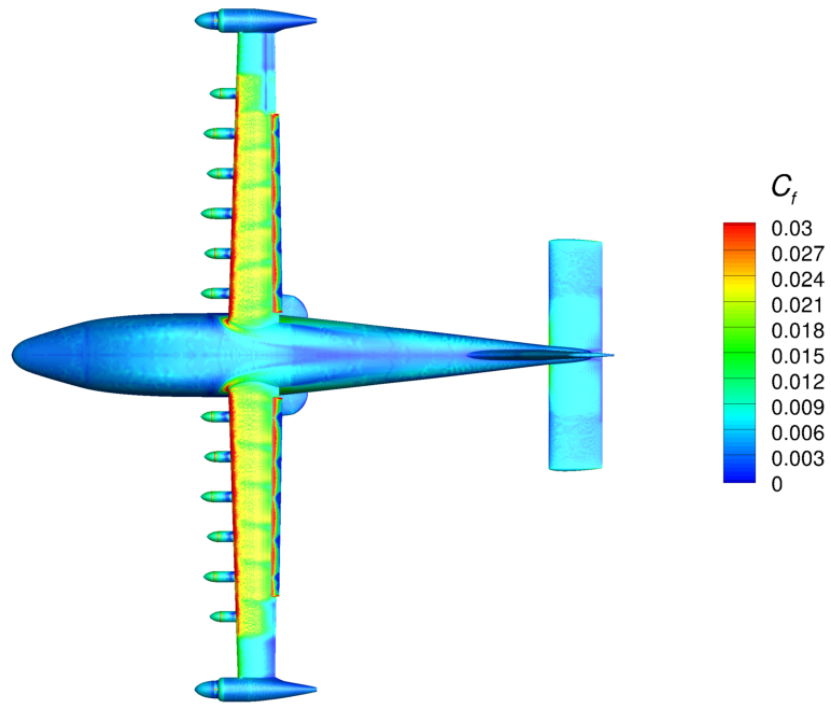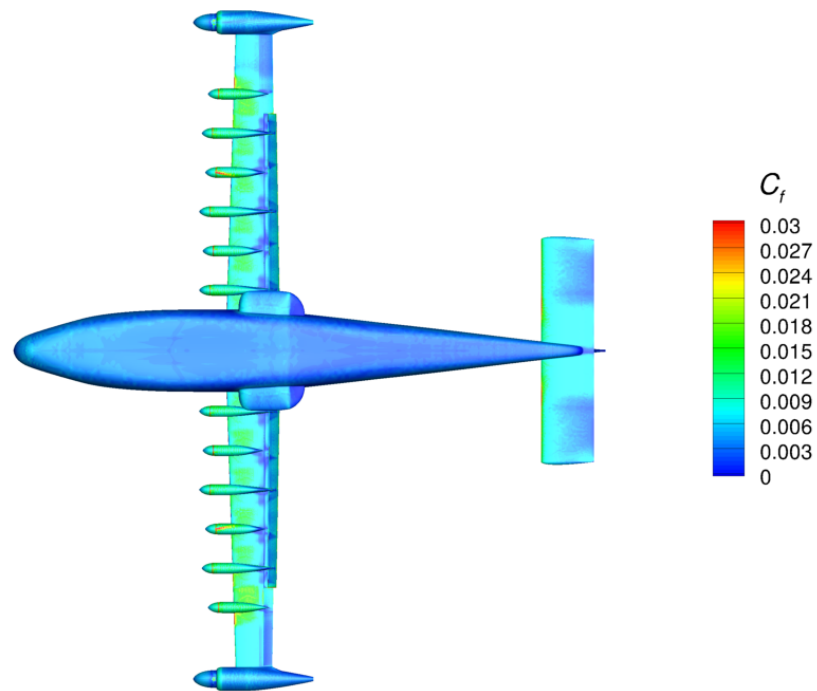
(a) Upper Surface

(b) Lower Surface

Figure 67. Skin Friction Coefficient for the Landing Configuration with $\delta_a = -15°$ at 58 KEAS and $\alpha = 14°$. High-Lift Blowing at 5035 RPM, $T = 50.65$ lbf, and $Q = 16.23$ lbf-ft. Cruise Propellers at 1540 RPM, $T = -8.02$ lbf, and $Q = 0.65$ lbf-ft. Kestrel SA RC.
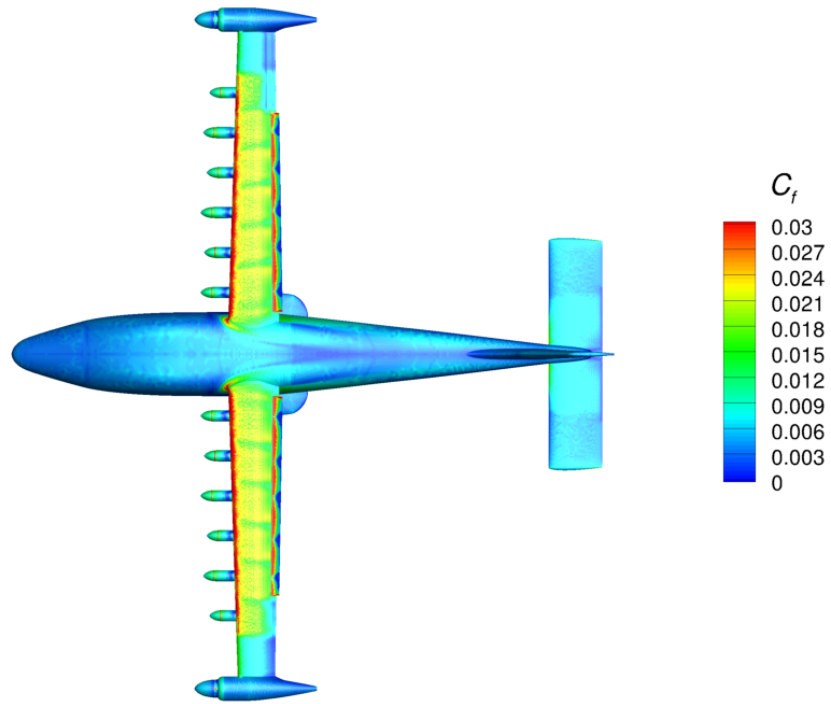
(a) Upper Surface

(b) Lower Surface

Figure 68. Skin Friction Coefficient for the Landing Configuration with $\delta_a = -10°$ at 58 KEAS and $\alpha = 14°$. High-Lift Blowing at 5035 RPM, $T = 50.65$ lbf, and $Q = 16.23$ lbf-ft. Cruise Propellers at 1540 RPM, $T = -8.02$ lbf, and $Q = 0.65$ lbf-ft. Kestrel SA RC.
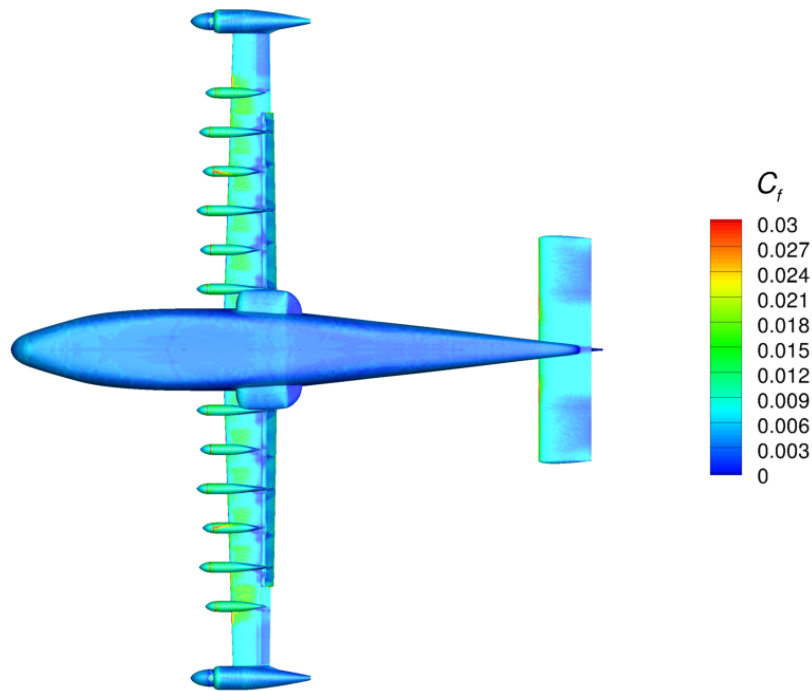
(a) Upper Surface

(b) Lower Surface

Figure 69. Skin Friction Coefficient for the Landing Configuration with $\delta_a = -5°$ at 58 KEAS and $\alpha = 14°$. High-Lift Blowing at 5035 RPM, $T = 50.65$ lbf, and $Q = 16.23$ lbf-ft. Cruise Propellers at 1540 RPM, $T = -8.02$ lbf, and $Q = 0.65$ lbf-ft. Kestrel SA RC.
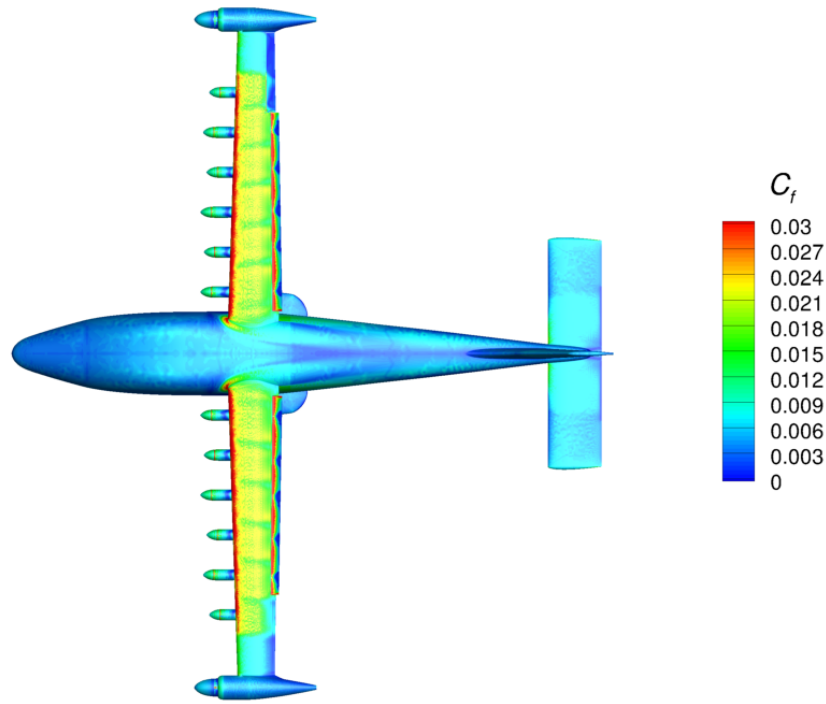
(a) Upper Surface

(b) Lower Surface

Figure 70. Skin Friction Coefficient for the Landing Configuration with $\delta_a = 0°$ at 58 KEAS and $\alpha = 14°$. High-Lift Blowing at 5035 RPM, $T = 50.65$ lbf, and $Q = 16.23$ lbf-ft. Cruise Propellers at 1540 RPM, $T = -8.02$ lbf, and $Q = 0.65$ lbf-ft. Kestrel SA RC.
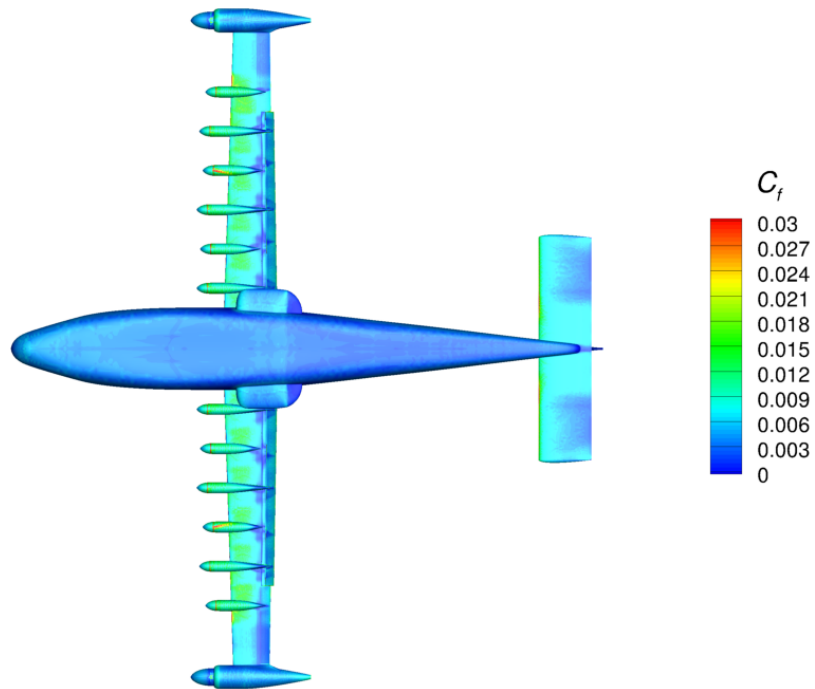
(a) Upper Surface

(b) Lower Surface

Figure 71. Skin Friction Coefficient for the Landing Configuration with $\delta_a = 10°$ at 58 KEAS and $\alpha = 14°$. High-Lift Blowing at 5035 RPM, $T = 50.65$ lbf, and $Q = 16.23$ lbf-ft. Cruise Propellers at 1540 RPM, $T = -8.02$ lbf, and $Q = 0.65$ lbf-ft. Kestrel SA RC.
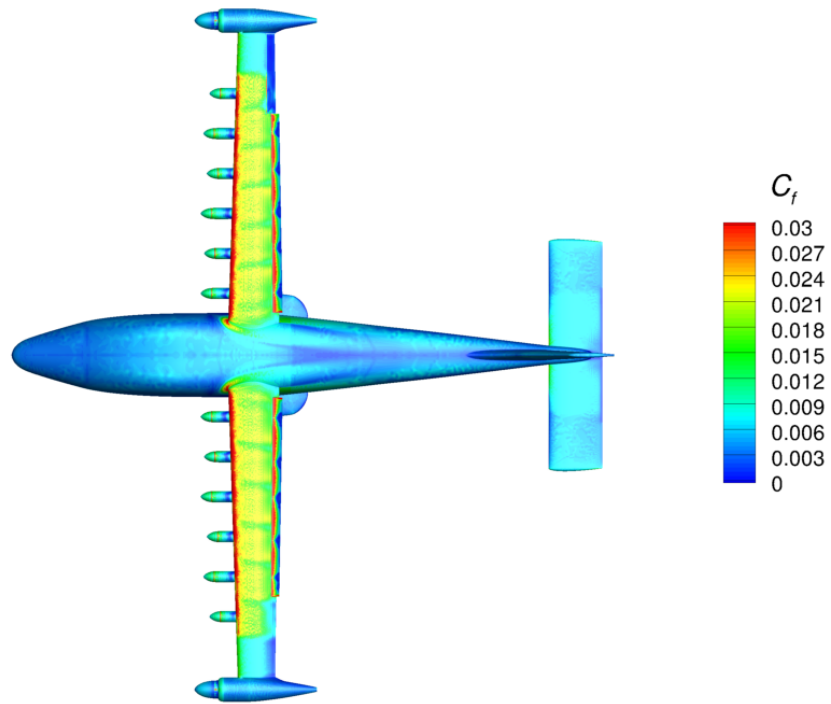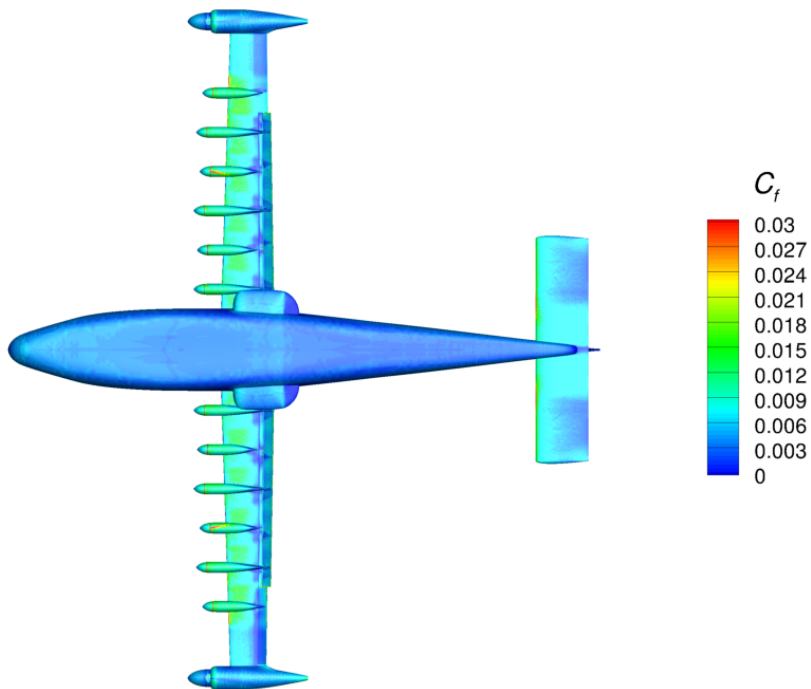
(a) Upper Surface

(b) Lower Surface

Figure 72. Skin Friction Coefficient for the Landing Configuration with $\delta_a = 18°$ at 58 KEAS and $\alpha = 14°$. High-Lift Blowing at 5035 RPM, $T = 50.65$ lbf, and $Q = 16.23$ lbf-ft. Cruise Propellers at 1540 RPM, $T = -8.02$ lbf, and $Q = 0.65$ lbf-ft. Kestrel SA RC.

B USM3D Skin Friction Coefficient Contours: Landing Configuration, 30° Flap Deflection, With Aileron Deflections

(a) Upper Surface

(b) Lower Surface

Figure 73. Skin Friction Coefficient for the Landing Configuration with $\delta_a = -15°$ at 58 KEAS and $\alpha = 2°$. High-Lift Blowing at 5035 RPM, $T = 50.65$ lbf, and $Q = 16.23$ lbf-ft. Cruise Propellers at 1540 RPM, $T = -8.02$ lbf, and $Q = 0.65$ lbf-ft. USM3D SA QCR2000.
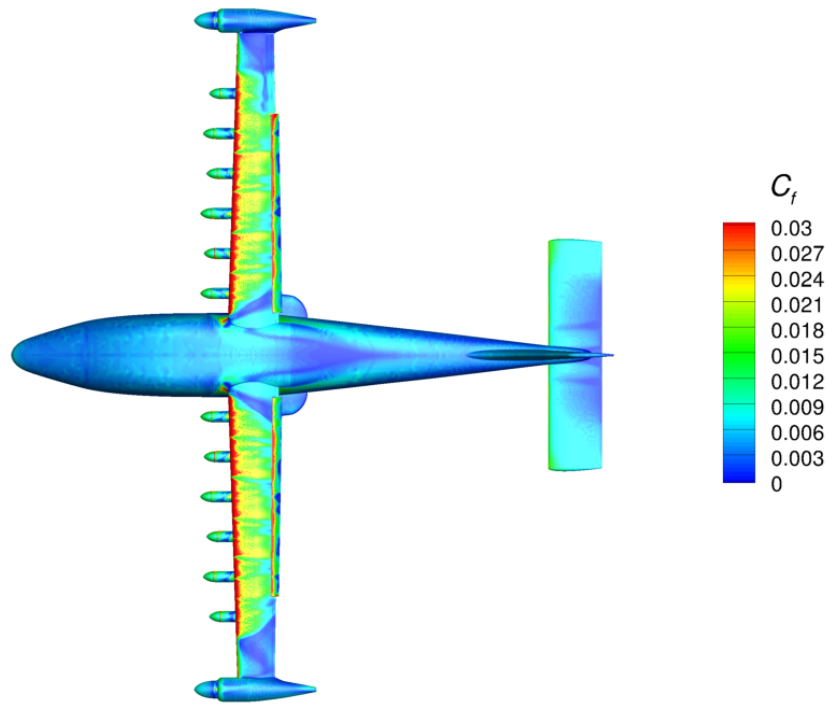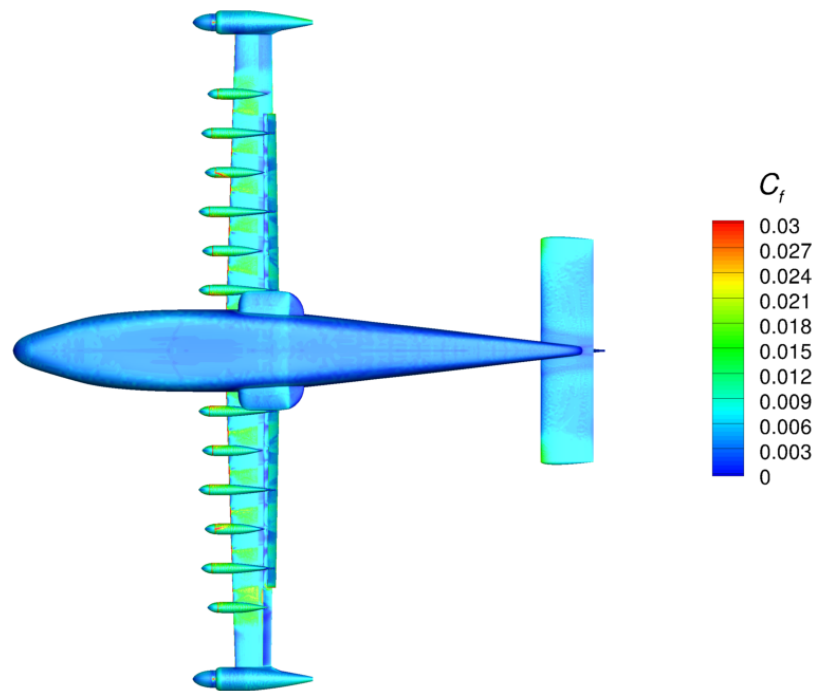
(a) Upper Surface

(b) Lower Surface

Figure 74. Skin Friction Coefficient for the Landing Configuration with $\delta_a = -10°$ at 58 KEAS and $\alpha = 2°$. High-Lift Blowing at 5035 RPM, $T = 50.65$ lbf, and $Q = 16.23$ lbf-ft. Cruise Propellers at 1540 RPM, $T = $ -8.02 lbf, and $Q = 0.65$ lbf-ft. USM3D SA QCR2000.
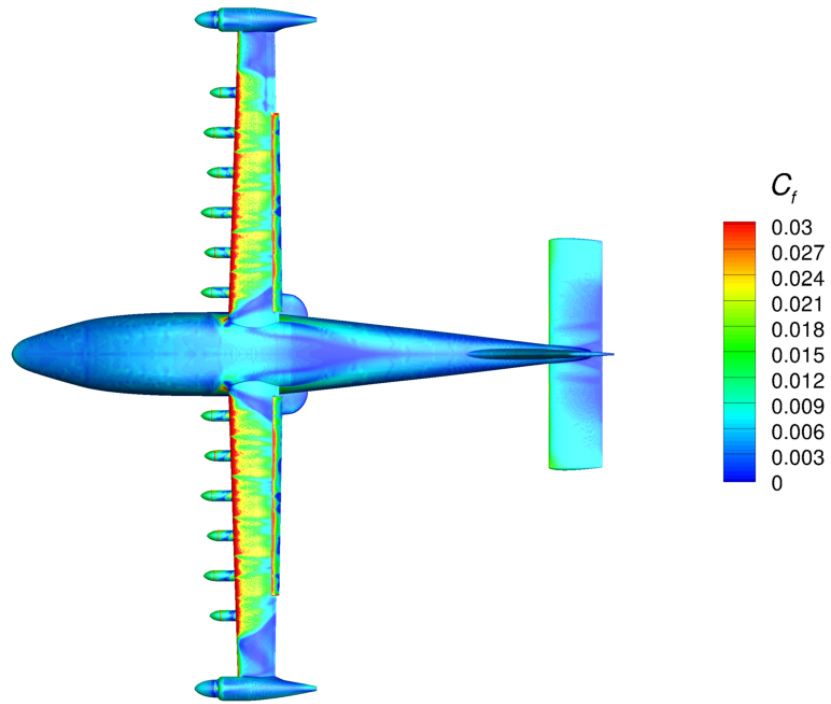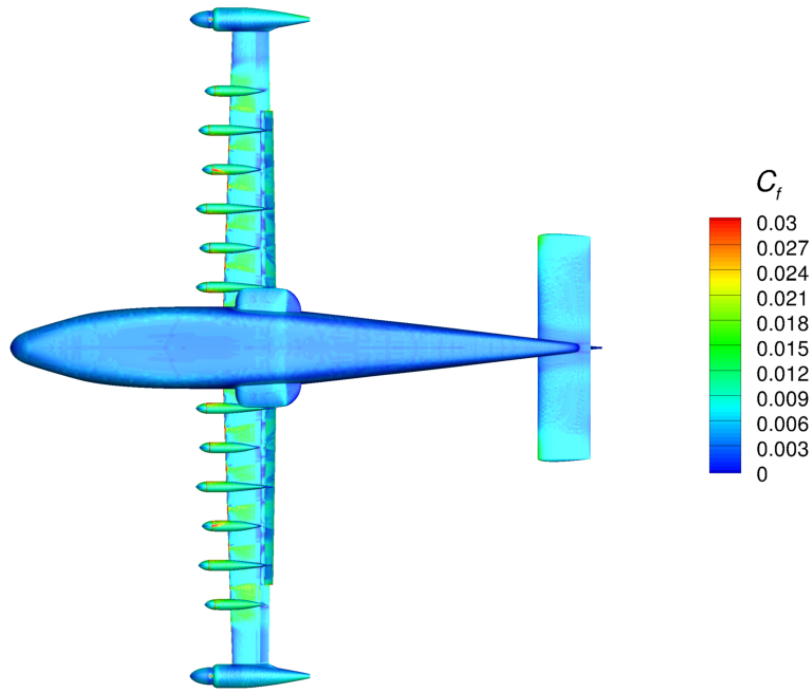
(a) Upper Surface

(b) Lower Surface

Figure 75. Skin Friction Coefficient for the Landing Configuration with $\delta_a = 10°$ at 58 KEAS and $\alpha = 2°$. High-Lift Blowing at 5035 RPM, $T = 50.65$ lbf, and $Q = 16.23$ lbf-ft. Cruise Propellers at 1540 RPM, $T = -8.02$ lbf, and $Q = 0.65$ lbf-ft. USM3D SA QCR2000.

(a) Upper Surface

(b) Lower Surface

Figure 76. Skin Friction Coefficient for the Landing Configuration with $\delta_a = 18°$ at 58 KEAS and $\alpha = 2°$. High-Lift Blowing at 5035 RPM, $T = 50.65$ lbf, and $Q = 16.23$ lbf-ft. Cruise Propellers at 1540 RPM, $T = -8.02$ lbf, and $Q = 0.65$ lbf-ft. USM3D SA QCR2000.
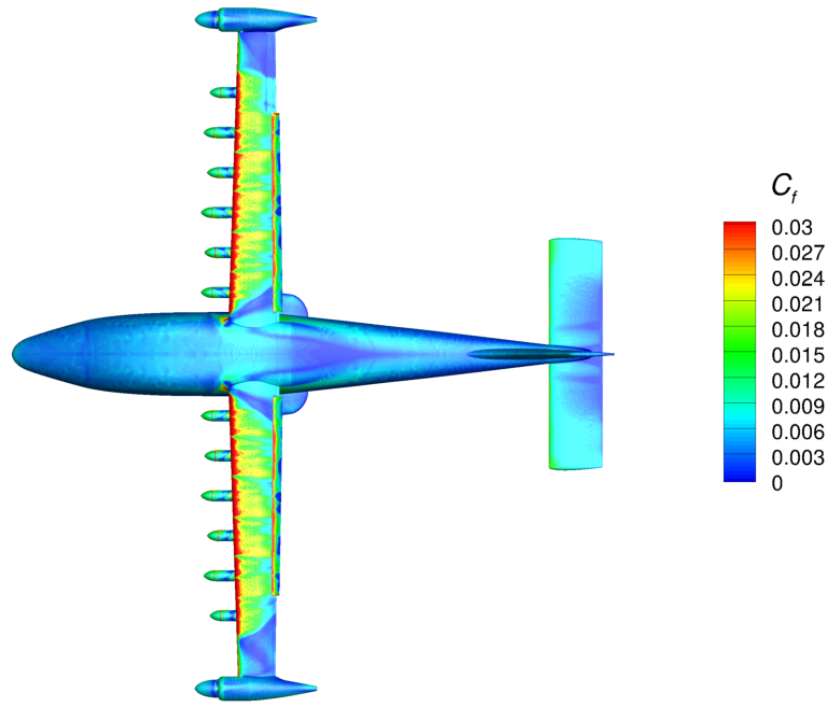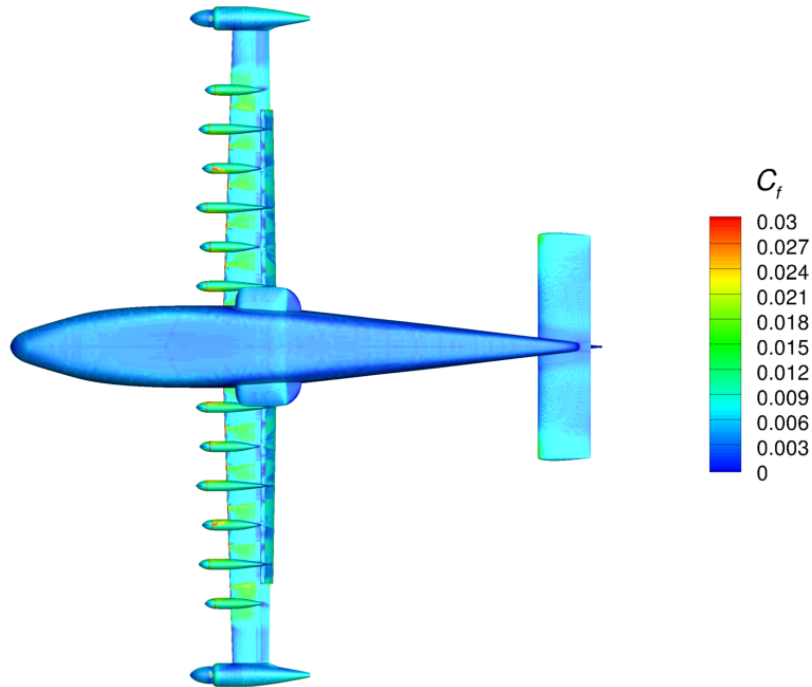
(a) Upper Surface

(b) Lower Surface

Figure 77. Skin Friction Coefficient for the Landing Configuration with $\delta_a = -25°$ at 58 KEAS and $\alpha = 14°$. High-Lift Blowing at 5035 RPM, $T = 50.65$ lbf, and $Q = 16.23$ lbf-ft. Cruise Propellers at 1540 RPM, $T = $ -8.02 lbf, and $Q = 0.65$ lbf-ft. USM3D SA QCR2000.
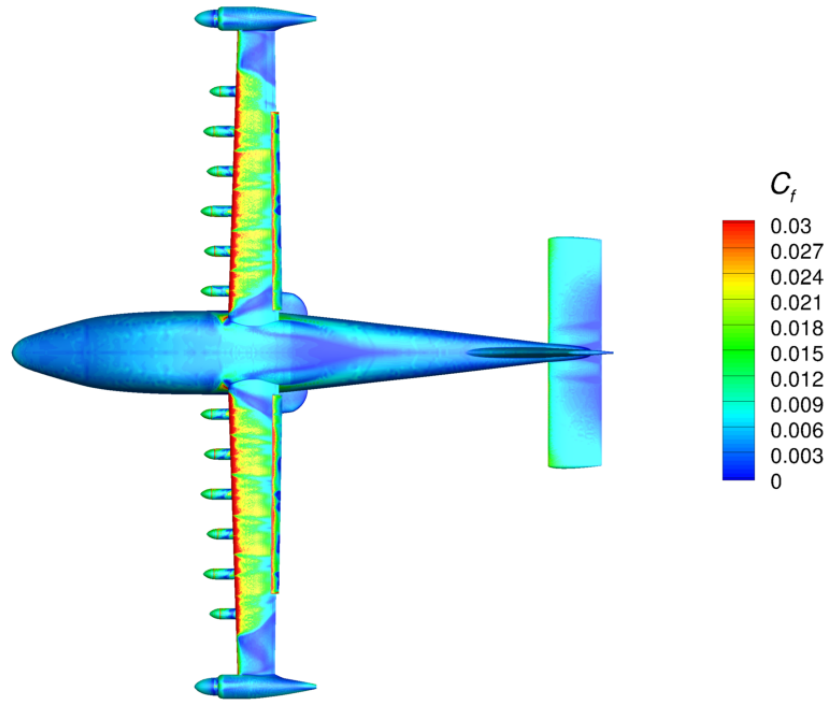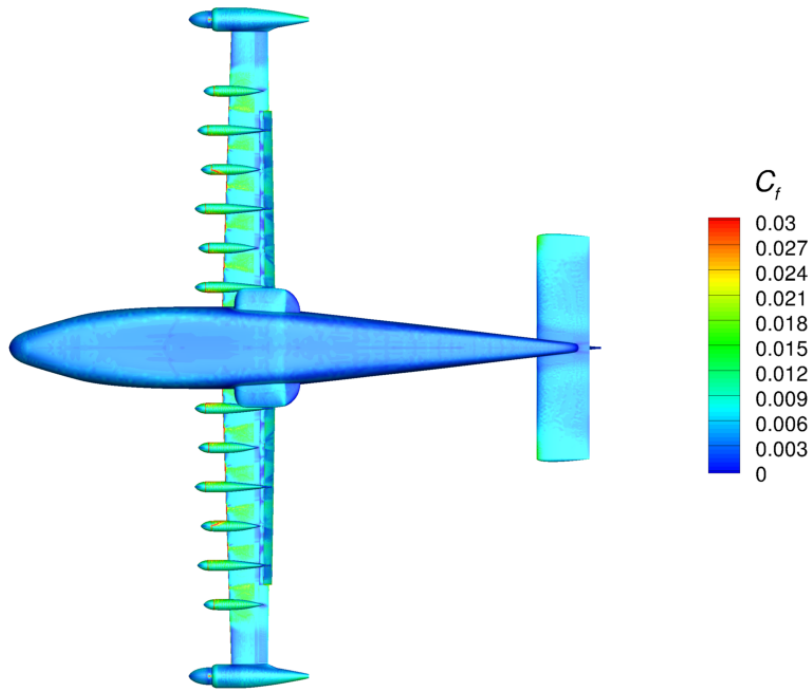
109

(a) Upper Surface

(b) Lower Surface

Figure 78. Skin Friction Coefficient for the Landing Configuration with $\delta_a = -15°$ at 58 KEAS and $\alpha = 14°$. High-Lift Blowing at 5035 RPM, $T = 50.65$ lbf, and $Q = 16.23$ lbf-ft. Cruise Propellers at 1540 RPM, $T =$ -8.02 lbf, and $Q = 0.65$ lbf-ft. USM3D SA QCR2000.

(a) Upper Surface

(b) Lower Surface

Figure 79. Skin Friction Coefficient for the Landing Configuration with $\delta_a = -10°$ at 58 KEAS and $\alpha = 14°$. High-Lift Blowing at 5035 RPM, $T = 50.65$ lbf, and $Q = 16.23$ lbf-ft. Cruise Propellers at 1540 RPM, $T = $ -8.02 lbf, and $Q = 0.65$ lbf-ft. USM3D SA QCR2000.
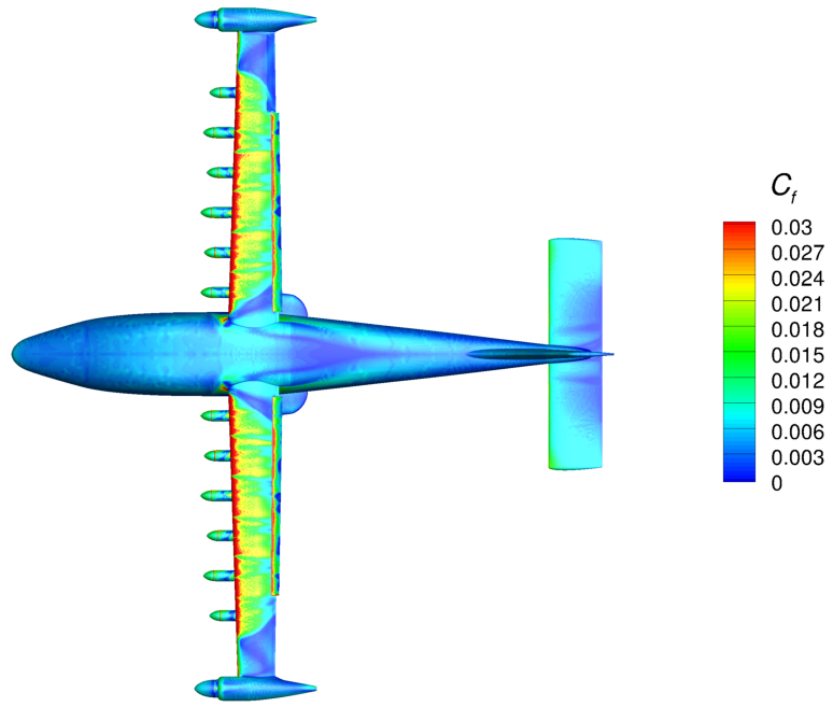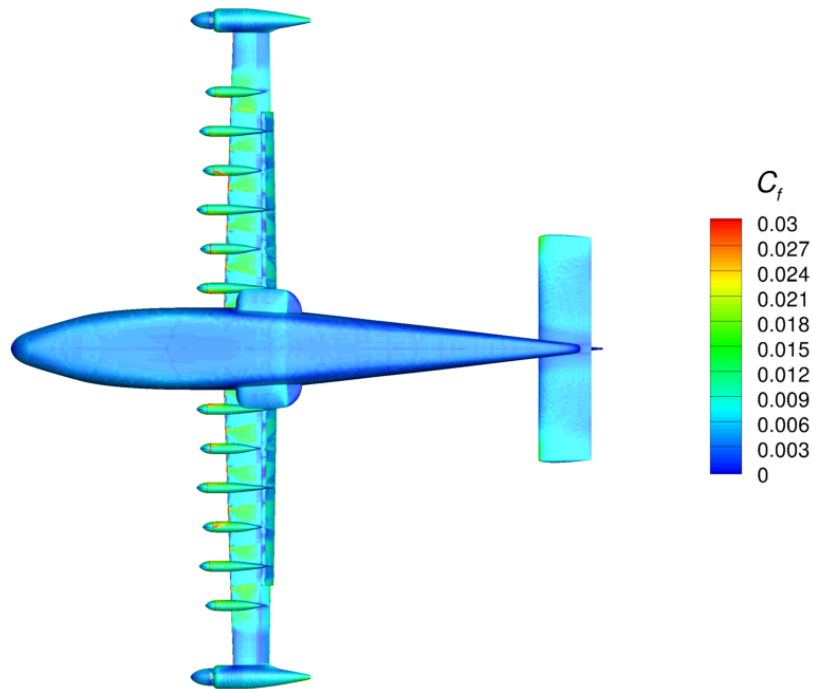
(a) Upper Surface

(b) Lower Surface

Figure 80. Skin Friction Coefficient for the Landing Configuration with $\delta_a = -5°$ at 58 KEAS and $\alpha = 14°$. High-Lift Blowing at 5035 RPM, $T = 50.65$ lbf, and $Q = 16.23$ lbf-ft. Cruise Propellers at 1540 RPM, $T = $ -8.02 lbf, and $Q = 0.65$ lbf-ft. USM3D SA QCR2000.
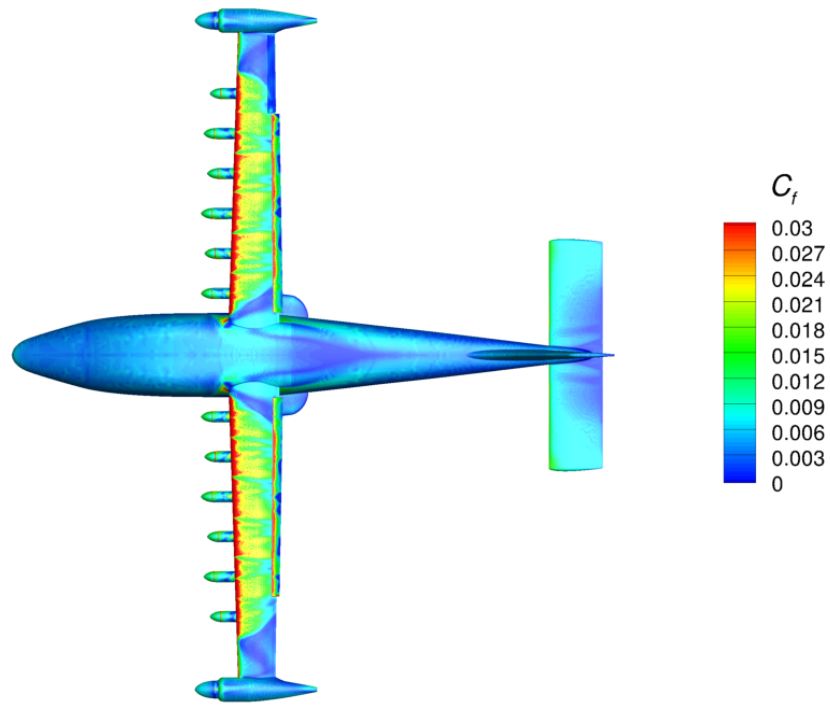
(a) Upper Surface

(b) Lower Surface

Figure 81. Skin Friction Coefficient for the Landing Configuration with $\delta_a = 10°$ at 58 KEAS and $\alpha = 14°$. High-Lift Blowing at 5035 RPM, $T = 50.65$ lbf, and $Q = 16.23$ lbf-ft. Cruise Propellers at 1540 RPM, $T = $ -8.02 lbf, and $Q = 0.65$ lbf-ft. USM3D SA QCR2000.
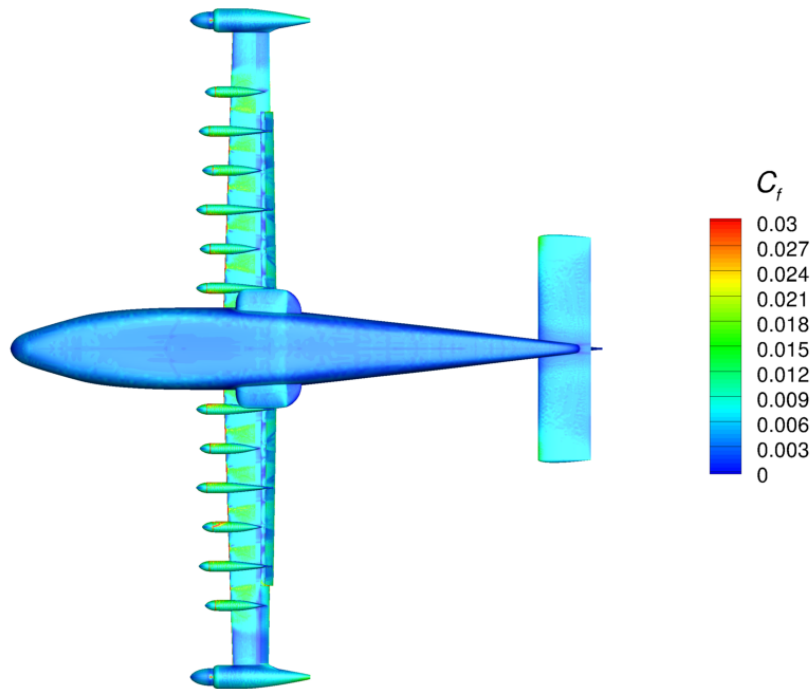
(a) Upper Surface

(b) Lower Surface

Figure 82. Skin Friction Coefficient for the Landing Configuration with $\delta_a = 18°$ at 58 KEAS and $\alpha = 14°$. High-Lift Blowing at 5035 RPM, $T = 50.65$ lbf, and $Q = 16.23$ lbf-ft. Cruise Propellers at 1540 RPM, $T = -8.02$ lbf, and $Q = 0.65$ lbf-ft. USM3D SA QCR2000.